FACULTY OF SCIENCES AND TECHNOLOGY OF THE UNIVERSITY OF COIMBRA

Biomedical Engineering 2010/2011

Master's thesis

PROPONENT: André Miguel Fernandes dos Santos

SUPERVISORS: Nicolás F. Lori (IBILI, FMUC)

"Visual-Callosal White Matter pathways in Neurofibromatosis type 1: A Diffusion Tensor Imaging – Fiber Tracking study"

-2011-

This work contributed to the publication of the following abstracts:

1. **Inês R. Violante, Maria Ribeiro, André Santos, Nicolás Lori, Eduardo Silva, Miguel Castelo-Branco**

"Structural and functional development of early cortical visual areas: an fMRI and DTI study"

Accepted for poster presentation at 17th Annual Meeting of the Organization for Human Brain Mapping (June, 2011 in Montreal, Canada)

2. **André Santos, Nicolás Lori, Inês R. Violante, Maria Ribeiro, Miguel Castelo Branco**

"Visual-Callosal White Matter pathways in Neurofibromatosis type 1: A Diffusion Tensor Imaging – Fiber Tracking study"

Accepted for poster presentation at 5th Workshop of the Organization for CInAPCe (August, 2011 in São Paulo, Brazil)

Acknowledgments

Ao Professor Doutor Nicolás Francisco Lori, pelos conhecimentos, ajuda e conselhos transmitidos no mundo da investigação em neurociências e técnicas de engenharia, que me ajudaram a crescer enquanto investigador e engenheiro.

À Inês Violante pela sua generosidade em tempo e atenção, ao longo de todo o ano lectivo, principalmente por toda a ajuda que me disponibilizou e pela esclarecedora troca de impressões que contribuiu para o desenvolvimento deste trabalho.

À Doutora Maria Ribeiro pelo disponibilizar dos dados que adquiriu, relacionados com o projecto sobre NF1, em que está a trabalhar, e pela atenção e detalhe com que analisou os resultados experimentais obtidos.

Ao Professor Doutor Miguel Castelo-Branco pela sua disponibilidade em integrar-me na fantástica comunidade científica que é o seu grupo de investigação no IBILI, e pela forma como a sua dedicação à neurociência me ajudou a focalizar a atenção na importância de usar a engenharia, enquanto veículo de melhoria no campo da neurociência.

Ao Professor Doutor Miguel Morgado pelo seu empenho e dedicação na coordenação e promoção do curso de Engenharia Biomédica.

A todas as crianças, adolescentes e adultos que participaram neste projecto, sem os quais este trabalho não seria possível, agradeço toda a disponibilidade e colaboração.

A todos os meus colegas do IBILI e do ICNAS que me receberam calorosamente, durante este ano lectivo, tendo sido promotores de apoio, convívio e bom ambiente.

Aos meus grandes amigos da Figueira da Foz e de Coimbra, por todos os adoráveis momentos que passei com eles, pela lealdade, carinho e afecto por eles demonstrados. O seu apoio e incentivo em muito contribuíram, para o projecto em que me envolvi, com especial destaque para este último ano.

A toda a minha família, por toda a preocupação e apoio demonstrados durante o meu curso de Engenharia Biomédica.

Um especial agradecimento aos meus pais, Carlos e Helena, por todos os meios que puseram ao meu dispor, pelo seu apoio nos bons e nos maus momentos, sem o qual dificilmente teria levado a bom termo este projecto. Também pelo exemplo e fonte de

inspiração que sempre foram para mim e ainda pelos grandes e benéficos conselhos que deles colhi.

À minha irmã, Diana que apesar de me "arreliar" com as suas brincadeiras sempre se preocupou comigo. Contribuiu em muito para a energia que necessitei, para que fosse um exemplo para ela seguir tanto no seu caminho escolar como nas escolhas que lhe que terá que fazer ao da sua vida.

A todos, o meu mais sincero obrigado.

Abstract

The present study aimed to investigate and provide neuroanatomic information on dorsal and ventral white matter (WM) pathways starting in low level cortical visual areas, in neurofibromatosis type 1. To achieve this goal we used DTI (Diffusion Tensor Imaging), FT (Fiber Tracking) and fMRI (Functional Magnetic Resonance Imaging) techniques.

Neurofibromatosis type 1 (NF1) is one of the most common autosomal inherited monogenic diseases, affecting the central nervous system (CNS) at a prevalence of approximately 1 in 3500 individuals. It is highly associated with cognitive deficits, mainly visual-perceptual abnormalities, which have been taken as a characteristic mark of the cognitive profile of these patients.

MRI studies suggest that visual-perceptual abnormalities might be related to an alteration in the WM microstructure. However there are no published studies employing a tractography analysis of white matter pathways in NF1. Our study combines several MRI methodologies to investigate the structural integrity of the WM pathways connecting early visual areas and the splenium of the corpus callosum.

33 NF1 patients and 43 healthy volunteers with an age range of 7 to 42 years participated in this study. Imaging analysis was performed with BrainVoyager QX 2.3 and Matlab 2011 software, allowing the definition of: V1, dorsal V2, ventral V2, dorsal V3 and ventral V3. These regions were used in the tractography analysis, with the purpose of estimating visual-callosal fiber tracts with seed points in each one of the considered regions.

For each tract estimated we extracted for each voxel the eigenvalues (λ1, λ2 and λ3), allowing the calculation of the mean diffusivity (MD), fractional anisotropy (FA) and axial FA values.

There was a successful identification of the visual-callosal fiber tracts for each visual area. NF1 patients presented a statistically significant decrease in FA and axial FA values and also an increase in MD and eigenvalues λ2 and λ3. The group effect was higher for the tracts estimated in children than in adults with NF1.

A higher group effect was found especially in the fiber tracts with seed points in the V1 and dorsal V2. No group effect was found in tracts with seed points in ventral V3, possibly related to the greater difficulty in the identification of tracts with seed points in ventral regions.

The significant FA and Axial FA decrease and MD increase are likely to be associated to diffuse and basic alterations in the WM microstructure, possibly related to myelin alteration. This possibility is also supported by the higher axial eigenvalues (λ2 and λ3) in the NF1 group, being this feature associated to myelin degradation.

In summary, our results indicate an alteration in the myelin microstructure of the visual-callosal fiber tracts in NF1, especially in children. Since these tracts are important to normal vision, the present results help to explain the visual-perceptual deficits observed in this disorder.

Resumo

O presente estudo visa investigar a providenciar informação neuro anatómica acerca do desenvolvimento das vias dorsais e ventrais de matéria branca que começam em áreas visuais corticais de baixo nível, associado à neurofibromatose tipo 1. De maneira a se atingir este objectivo, recorreu-se ao uso de técnicas de DTI (Diffusion Tensor Imaging [Imagens de Tensor de Difusão]), FT (Fiber Tracking [Tractografia]) e fMRI (Functional Magnetic Resonance Imaging [Imagens de Ressonância Magnética Funcional]).

Neurofibromatose tipo 1 (NF1) é uma das doenças monogénicas, hereditárias e autossómicas das mais comuns, afectando o sistema nervoso central (SNC) numa prevalência de aproximadamente 1 em 3500 indivíduos. Está altamente associada a défices cognitivos, principalmente a anormalidades no domínio visual e espacial, o que tem sido referido como uma marca característica no perfil cognitivo de pacientes com NF1.

Vários estudos de ressonância sugerem que as anormalidades no domínio visual e de percepção podem estar relacionados com uma alteração na microestrutura da matéria branca. Contudo, ainda não há nenhum estudo publicado onde se utilize uma análise de tractografia nas vias de matéria branca em NF1. Portanto, o nosso estudo visa combinar várias metodologias RM para investigar a integridade estrutural das vias de matéria branca que conectam as regiões do córtex visual umas com as outras a partir do esplênio do corpo caloso.

Para este estudo participaram 43 voluntários saudáveis e 33 pacientes com NF1, idades entre os 7 e os 42 anos de idade. Toda a análise de imagem foi feita com os softwares do BrainVoyager QX 2.3 and Matlab 2011, permitindo a definição de: V1, V2 dorsal, V2 ventral, V3 dorsal e V3 ventral. Estas áreas visuais foram depois usadas na análise tractografica, com o objectivo de estimar as fibras que ligassem o córtex visual ao corpo caloso, identificadas com os seus respectivos pontos de partida em cada uma destas regiões visuais.

Para cada uma das fibras estimadas extraiu-se para cada voxel os valores próprios (λ1, λ2 e λ3), permitindo o cálculo da difusividade média (MD) e da anisotropia fraccional (FA). Valores de FA axial também são calculados.

Houve uma identificação bem sucedida das fibras que conectam o lobo occipital ao corpo caloso de acordo com a respectiva região visual de partida. Encontrou-se um decréscimo estatisticamente significativo na anisotropia fraccional e na axial assim como um acréscimo significativo nos valores de difusividade e valores próprios λ2 e λ3 em indivíduos com NF1. Este efeito de grupo foi mais significativo para as fibras estimadas em crianças com NF1.

Um maior efeito de grupo é encontrado nas vias de matéria branca que começam em V1 e em V2 dorsal. Não foi observado nenhum efeito de grupo para as vias que começam na região visual V3 ventral, podendo este facto estar relacionado com a maior dificuldade que se encontra na identificação das vias de matéria branca com partida em regiões ventrais.

O decréscimo significativo de FA e FA axial e o acréscimo de MD que é verificado nas vias de matéria branca identificadas está associado a alterações básicas na sua microestrutura. Esta possibilidade é suportada pelo acréscimo significativo dos valores próprios λ2 e λ3 no grupo NF1, sendo que este facto está relacionado com uma degradação da mielina.

Resumindo, os nossos resultados indicam uma alteração na microestrutura da mielina nas fibras que conectam as diversas regiões do córtex visual em indivíduos diagnosticados com NF1, especialmente em crianças. Sendo estas fibras, extremamente importantes para a visão, os resultados presentes ajudam a explicar os défices visuais e de percepção que são normalmente observados nesta doença.

Motivation

Previous studies focused in NF1-associated impairments, through its microstructural and functional alterations in the human brain's WM and GM. These studies show evidences suggesting alterations in the microstructural organization of the brain's WM and GM related with several cognitive functions, especially for language and visuospatial function.

Several studies prove the strong association of the visuospatial performance with diagnosis, helping in the detection of NF1 in approximately 90% of children and adults with the disease [1, 9, 10]. Therefore, the presence of this cognitive impairment may be extremely important for the detection of the deficits verified in NF1. The study of WM interconnections between the striate and extrastriate cortex visual areas might give valuable information to the understanding of the visual impairments in NF1. Therefore, we combined DTI and tractography techniques in order to obtain neuroanatomical information about the connections between the different regions of the visual cortex. The combination of DTI and Fiber Tracking techniques allows the estimation of WM pathways within the brain, and thus enabling to study in more detail the microstructure of the estimated fibers. This methodology was used to answer the following questions:

1) How can we estimate WM pathways connecting dorsal and ventral regions in the visual cortex?

2) Is there any microstructural alteration in these pathways in children and adults diagnosed with NF1?

3) Can an alteration in these pathways be related to the visuospatial deficits in NF1?

Trying to answer these questions we will perform a combining Diffusion Tensor Imaging – Fiber Tracking quantitative analysis to comprehend the development of both dorsal and ventral WM pathways starting in low-level cortical visual areas. We will extract the eigensystem values of the diffusion tensor ($\lambda 1$, $\lambda 2$ and $\lambda 3$), and also mean values of diffusivity (MD), fractional anisotropy (FA) and Axial FA of visual-callosal WM pathways connecting visual areas of the cortex between right and left brain hemispheres, providing neuroanatomic information about these pathways, for a comparison between NF1 and healthy volunteers.

All the in-house software mentioned in this work was developed by the proponent (André Santos), and it was based on the BrainVoyager Toolbox functions.

Table of Contents

Abbreviations

DDT – Diagonalized Diffusion Tensor

DMR – Diffusion Project

DTI – Diffusion Tensor Imaging

fMRI – functional Magnetic Resonance Imaging

FT – Fiber Tracking

GM – Gray Matter

MRI – Magnetic Resonance Imaging

NF1 – Neurofibromatosis type 1

UBOs – Unidentified Bright Objects

V1 – Primary Visual Cortex

VDW – Volume Diffusion Weighted

VMR – Anatomical Project

WM – White Matter

List of Figures

essential to the proper communication between read processing regions of the brain, identified by Ben-Shachar (2007); In the image it can been identified in red the occipital-callosal fibers, similar to the ones identified by Dougherty (2005), as well as, temporal-callosal fibers.

Figure 9: Magnetization in two different situations: (a) Natural state, with no magnetic field applied to the spins; (b) Application to a magnetic field B_0 with a certain speed and strength.

Figure 10: (a) Spinning precession around B_0 at the Larmor frequency; (b) The magnetic vector M can be separated in two different components: longitudinal magnetization (M_z) along the z-axis and transversal magnetization (M_{xy}) on the xy-plane.

Figure 11: (a) a RF pulse turns the magnetization by exactly 90° into the xy-plane, causing the entire longitudinal magnetization (M_z) to transform into traverse magnetization, (M_{xy}) (b).

Figure 12: T1 relaxation process; Decay of transverse magnetization within the xy-plane and realignment of the longitudinal magnetization with the z-axis.

Figure 13: T2 relaxation; Spins lose phase coherence and transverse magnetization decays progressively.

Figure 14: Spin-echo [a-f]; Illustration of transverse magnetization dephasing, after the application of a 90° RF pulse [a-c]; with the application of the 180° RF pulse, the spins will be back in phasing, converging to coherence after a echo time (TE)

Figure 15: Multi-echo sequence; Illustration of spin-echo signal decrease with T2*

Figure 16: Relation between repetition time (TR) and T1 contrast; With a long TR, all tissues with long or short T1 will have time to recover full longitudinal magnetization, having as a result a small T1 contrast effect on the acquired image.

Figure 17: Relation between echo time (TE) and T2 contrast; a shorter T2 will result in a greater MR signal lost, with the appearance of darker tissues, making hard to distinguish them, while a longer T2 will result in a stronger signal thus, the tissues will appear bright.

Figure 18: (A) MRI device main components; (B) Representation of a 3T Siemens MRI scanner

Figure 19: Fick's first law, illustrating a molecular diffusion transport between regions with different concentrations and with a diffusion tendency from regions with higher to lower concentrations.

Figure 20: Illustration of the pulsed field gradient spin-echo MR sequence approach introduced by Stejskal and Tanner. The time between the two gradient pulses is denoted by Δ and δ as the pulse duration.

Figure 21: Difference between an off-diagonal element of the diffusion tensor and the respective apparent diffusion coefficient; (A) In this case the diffusivity along the x-axis is equal to the one along the y-axis, because of the anisotropy orientation at 45 degrees to both of them. In this case the displacements along the two are perfectly correlated; (B) In this case, x-axis and y-axis displacements are no longer correlated, being D_{xy} equal to zero, however the ADC along the x-y axis is not zero.

Figure 22: (A) Illustration of the diffusion tensor as a 3D ellipsoid and respective diffusion-weighted acquisitions acquired from the 6 possible directions. From each acquisition it is possible to extract the diffusion tensor synthesizing all the diffusion data; (B) Association of the diffusion tensor ellipsoid to an illustrative water molecule diffusion anisotropy in the brain's WM, where the molecules follow the direction of the fibers, being restricted perpendicularly to them. From each direction, we can see the different diffusion-weighted acquisition contrasts.

Figure 23: Water molecule diffusion associated to a diffusion ellipsoid, where two types of diffusion are established: diffusion parallel to the fiber length associated to the major eigenvalue ($\boldsymbol{\lambda_1}$) of the diffusion tensor, and perpendicular diffusion associated to the two smaller eigenvalues ($\boldsymbol{\lambda_2}$ and $\boldsymbol{\lambda_3}$).

Figure 24: Illustration of three diffusion ellipsoids, all with the same mean diffusivity value (MD=0.7x10^{-3} mm^2) and fractional anisotropy ranging from isotropic (lower FA=0.12) to anisotropic (higher FA=0.82)

Figure 25: MD (A) and FA (B) data collection of a brain's slice in a transversal section. The image intensity is proportional to the diffusion and anisotropy degree (A and B respectively). In image B, there's a proper distinction between the GM with the lowest intensities and the WM, with the highest intensities.

Figure 26: Example of the coronal and transversal section of a color-encoded fiber orientation maps, obtained with the BrainVoyager 2.3. QX software. A combination of colors creates tracts of different colors

Figure 27: Illustration of a HARDI acquisition in a specific voxel; in (A) it is properly represented in a specific voxel two crossing tracts, while in (B) using DTI we have only one tract

Figure 28: Illustration of the association of anisotropy with the CNS; First we have a separation of the brain's white and GM through imaging contrast, and we can verify the differences in both structures allowing, for the case of WM, a more anisotropic water diffusion in the presence of parallel axons.

Figure 29: Examples of streamline tractography following the orientation of diffusion MRI data along the principal eigenvector with the highest eigenvalues; (A) is the illustration of the specific streamline tractography developed by BrainVoyager QX 2.3.software (B) shows the specific streamline tractography developed by Mori et al (1999), where the diffusion tensor main orientations are identified by its primary colors

Figure 30: Illustration of the three existing types of water molecule diffusion considered in DTI (A, B and C), leading to different MR signal attenuations and correspondent contrasts in the diffusion-weighted image acquisition.

Figure 31: Schematic illustration of anistropic water diffusion measurement form axons to tracts, using DTI methodologies over resolution of several millimeters in voxels, extracting the WM tracts in the brain

Figure 32: Illustration of two types of fiber tracking approaches developed by the Human Connectome Research group; (A) illustrates the full fiber connectivity through the medial section of the corpus callosum, while in (B) we have the full fiber connectivity estimation of the human brain

Figure 33: (A) VMR final "Project Creation" dialog, with all the specific information required for its creation; (B) Schematic illustration of the VMR as a 3D anatomical data set, with proper visualization of the brain on sagital, coronal and transversal views.

Figure 34: (A) Schematic illustration of a sagital brain view. The anterior commisure is represented in red, while the posterior commisure is in blue; (B) Same sagital brain view as in A, with a different zooming where the AC-PC plane is identified by the horizontal green line

Figure 35: (A) DMR final "Project Creation" dialog, with all the specific information required for its creation; (B) Schematic illustration of the DMR as a diffusion weighted file, illustrating the brain in 35 slices.

Figure 36: Schematic illustration sagital, coronal and transversal views of the co-registration of the DWI data of the DMR project (in green) to the 3D anatomical data of the VMR project.

Figure 37: "VDW File Creation" window in BrainVoyager 2.3 QX;

Figure 38: Schematic illustration of the sagital view of the brain before (A) and after (B) the segmentation; (C) After the segmentation the resulted voxels are colored and the mask is created using those colored voxels

Figure 39: (A) Schematic illustration of the "VDW Analysis" window in BrainVoyager 2.3. QX, where the creation of the DDT file is performed; in the boxes blue and red correspond respectively to the inputs of the mask and VDW file required. The box in orange will estimate the diffusion tensor for each voxel of the input data; (B) Schematic illustration in a part of the VMR data of the diffusion tensors for each voxel, estimated with the creation of the DDT file.

Figure 40: Schematic Illustration of a VMP of the same brain slice, associated to an intensity histogram, where the color varies with the specific diffusion parameter value; In (A) we have the MD VMP, while in (B) we have the illustration of a FA computation. The VMP values ranges between 0 and 1, for both MD and FA; yellow color corresponds to the voxels with the highest scalar values for FA, while orange corresponds to the lowest ones

Figure 41: Schematic Illustration of a VMP of the same brain slice, illustrating an intensity histogram of eigenvalues λ_1, λ_2 and λ_3 in images (A), (B) and (C) respectively; yellow color corresponds to the voxels with the highest eigenvalue scalar values, while orange corresponds to the lowest ones

Figure 42: Schematic illustration of the "Volume Tools" windows used in BrainVoyager QX for a proper drawn of the occipital lobe´s WM volume of interest (VOI)

Figure 43: Sagital (A) and transversal (B) schematic illustrations of a volume of interest (VOI) defined in BrainVoyager for our fiber tracking procedure, in the occipital lobe's WM occupying both brain hemispheres

Figure 44: Schematic illustration of all fiber tracts that pass through the occipital lobe

Figure 45: (A) Schematic illustration of a VOI drawn surrounding the splenium of the corpus callosum; (B) "VOI Fiber Tracking" window in BrainVoyager QX, where the seed and intersection points are selected.

List of Tables

List of Graphics

Graphic 13: Average λ_3 of visual-callosal WM pathways with seed points in V1, V2d, V2v, V3d and V3v in adults, on a group effect comparison between control subjects and NF1 patients.

Graphic 14: Percentage of fiber identification, according to each seed visual region in control subjects and patients with NF1 separated between (A) children and (B) adults.

Graphic 15: Average FA in visual-callosal WM pathways with seed points in V1, V2d, V2v, V3d and V3v in children, on a group effect comparison between control subjects and NF1 patients.

Graphic 16: Average FA in visual-callosal WM pathways with seed points in V1, V2d, V2v, V3d and V3v in adults, on a group effect comparison between control subjects and NF1 patients.

Graphic 17: Average Axial FA in visual-callosal WM pathways with seed points in V1, V2d, V2v, V3d and V3v in children, on a group effect comparison between control subjects and NF1 patients.

Graphic 18: Average Axial FA in visual-callosal WM pathways with seed points in V1, V2d, V2v, V3d and V3v in adults, on a group effect comparison between control subjects and NF1 patients.

Graphic 19: Average MD in visual-callosal WM pathways with seed points in V1, V2d, V2v, V3d and V3v in children, on a group effect comparison between control subjects and NF1 patients.

Graphic 20: Average MD in visual-callosal WM pathways with seed points in V1, V2d, V2v, V3d and V3v in adults, on a group effect comparison between control subjects and NF1 patients.

Graphic 21: Average λ_1 of visual-callosal WM pathways with seed points in V1, V2d, V2v, V3d and V3v in children, on a group effect comparison between control subjects and NF1 patients.

Graphic 22: Average λ_1 of visual-callosal WM pathways with seed points in V1, V2d, V2v, V3d and V3v in adults, on a group effect comparison between control subjects and NF1 patients.

Graphic 23: Average λ_2 of visual-callosal WM pathways with seed points in V1, V2d, V2v, V3d and V3v in children, on a group effect comparison between control subjects and NF1 patients.

Graphic 24: Average λ_2 of visual-callosal WM pathways with seed points in V1, V2d, V2v, V3d and V3v in adults, on a group effect comparison between control subjects and NF1 patients.

Graphic 25: Average λ_3 of visual-callosal WM pathways with seed points in V1, V2d, V2v, V3d and V3v in children, on a group effect comparison between control subjects and NF1 patients.

Graphic 26: Average λ_3 of visual-callosal WM pathways with seed points in V1, V2d, V2v, V3d and V3v in adults, on a group effect comparison between control subjects and NF1 patients.

State of the art

Chapter 1: Neurofibromatosis type 1

1.1. NF1 disease characteristics

1.1.1. Phenotypic manifestations

Neurofibromatosis type 1 (NF1) is one of the most common autosomal inherited monogenic diseases, affecting both skin and central nervous system (CNS) at a prevalence of approximately 1 in 3500 individuals, regardless of age, gender and any ethnic background [1,2,3]. It was described for the first time in medical literature in 1882, by Dr. Friedrich von Recklinghausen, being called during the following years as von Recklinghausen's neurofibromatosis [1].

NF1 is considered as a neurocutaneous disorder with a large variety of phenotypic manifestations [1,4,3], such as:

- skin freckling and formation of cutaneous neurofibromas and café-au-lait spot marks (figure 1A);
- bone malformation and presence of scoliosis;
- tumors located in the optic nerve (known as optic gliomas) affecting consequently the eyes (figure 1B);
- both endocrine and CNS alterations (T2-weighted hyperintensities, known as unidentified bright objects (UBOs) and macrocephaly) (figure 1C);

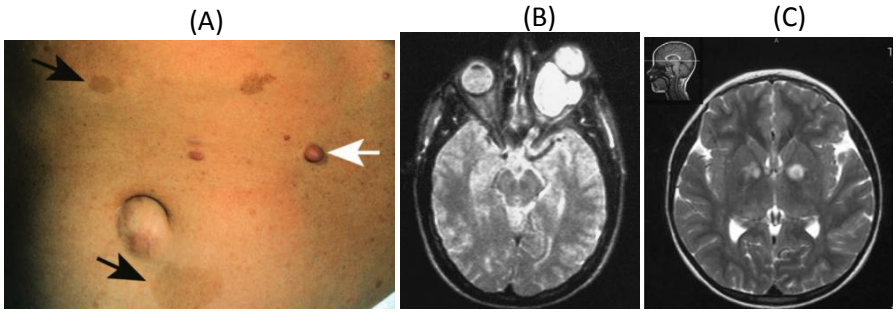

Figure 7: Illustration of some phenotypic manifestations occurring in NF1: (A) café-au-lait spots [5]; (B) optic gliomas; (C) T2-weighted hyperintensities, known as UBOs [6].

NF1 diagnosis is based on the clinical manifestations of at least two of seven criteria [1,2]. Table 1 shows the seven diagnostic criteria for NF1 as defined by the National Institute of Health (NIDs):

Table 11: National Institutes of Health diagnostic criteria for NF1; Na individual is considered to have NF1 when two or more of the following features are met [2].

- Six or more café-au-lait macules over 5mm in greatest diameter in prepurbertal individual and over 15 mm in greatest diameter in postpubertal individuals;
- Two or more neurofibromas of any type or one plexiform neurofibroma;
- Freckling in the axillary or inguinal regions;
- Optic glioma (tumour located in the optic nerve);
- Two or more Lisch nodules (iris hamartomas)
- A distinctive osseous lesion such as sphenoid dysplasia or thinning of long bone cortex with or without pseudoarthrosis;
- A first-degree relative (parent, sibling or offspring) with NF1 by the above criteria;

1.1.2. Cognitive impairments

Several studies report that NF1 is clearly associated to cognitive impairments, leading to the behavioral manifestations and learning disabilities verified in 30-60% of the NF1 individuals [1,3,7,8] .

NF1 affects crucial cognitive functions like attention, memory, language, visual perception and reading/vocabulary [1,3,4,8]. According to some studies, about 50% of children with NF1 reach poor academic achievements due to deficit in attention, planning procedures, as well as a lower shift in the distribution of IQ scores [1,8,9]. Learning disabilities is the major cognitive deficit present in NF1, being diagnosed in up to 65% of NF1 patients, where there are verified components of non-verbal and verbal-type learning disabilities [4]. Attention Deficit Disorder is another cognitive deficit verified in NF1 individuals, especially in children, with serious problems of inattention not only at school, but also at home [1]. Another important cognitive deficit, extremely associated to NF1, is visual-perceptual abnormalitities, which have been taken as a characteristic mark in the cognitive status in NF1 patients. Several studies prove the strong association of the visuospatial performance with diagnosis, helping in the detection of NF1 in approximately 90% of children and adults with the disease [1,9,10]. Therefore, the presence of this cognitive impairment may be important for the development of cognitive deficits verified in NF1.

1.2. Human genetics in NF1: NF1 gene and protein

In 1987, studies investigating the NF1 genotype found that NF1 patients presented translocation breakpoints on chromosome 17, which was the beginning of the disease-causing gene discovery [11, 12]. The NF1 gene is composed by 60 exons [13] and it is classified as a tumour suppressor (figure 1). The mutation in the NF1 gene is one with highest ratio of occurrence in the human genome [14]. The NF1 gene is highly conserved between species. In a study in 1993, Dr. Bernards revealed that the NF1 gene protein product neurofibromin, in humans had a considerable homology with the neurofibromin in mouse and drosophila (approximately 98% and 60% respectively) [13].

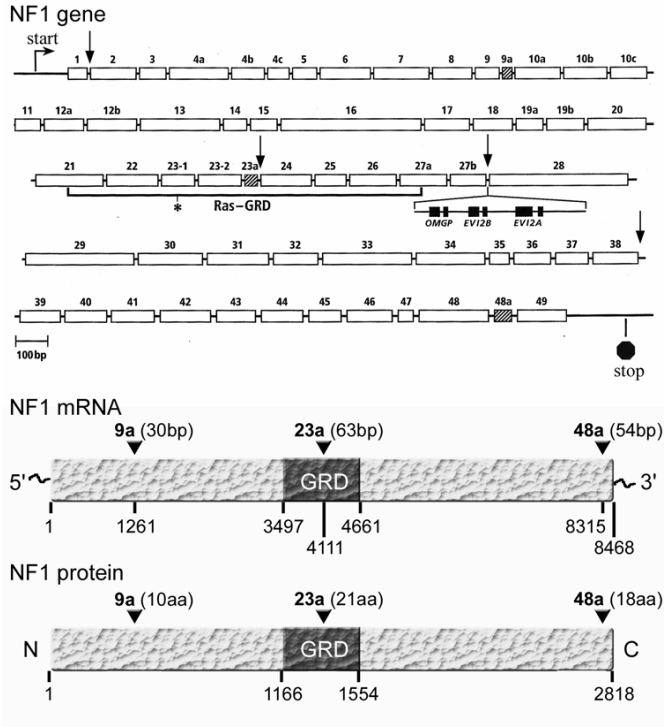

Figure 8: Schematic representation of the NF1 gene, mRNA and NF1 protein; Presentation of all the exons of the NF1 gene as well as an illustration of the spliced exons if NF1 mRNA and protein (9a, 23a and 48a) and the GAP-related domain of the NF1 protein; [15].

A major function of neurofibromin is the inhibition/regulation of the Ras pathway. The activation occurs from one of the neurofibromin domains, specifically the domain for the activation of guanosine triphosphate (GTPase)[2,7]. This control is performed by Ras-GTPase-activating proteins (Ras-GAPs), inactivating Ras-attached-GTP with the transformation of GTP to GDP. Ras is responsible for intracellular signal transmission, with a wide range of expression sites between the surface and the cell nucleus. This transmission will regulate the transcription

of genes involved in cell differentiation and proliferation [2]. A mutation in the NF1 gene will cause a neurofibromin disfunction, stopping with the ability to inhibit Ras. The lack of Ras inhibition leads to its exaggerated activation, and the basis of tumour development in NF1 [2,4, 13].

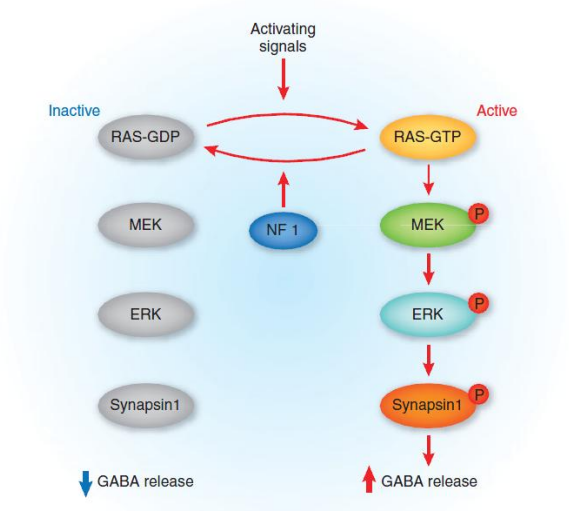

Figure 9: Illustration of Ras signal regulation by the neurofibromin functioning; neurofibromin is responsible for Ras inhibition by the GTP hydrolysis to GDP; In the case of a neurofibromin mutation/deficiency, Ras activation will be exaggerated, leading to a overwhelming activation of MEK and ERK kinases. This will cause a decreased GABA release from inhibitory neurons [16].

From previous studies performed in mice model, it was possible to conclude that the exaggerate activation of Ras by NF1 gene mutation is also associated with the increased release of the neurotransmitter gamma-aminobutyric acid (known as GABA) [2,4]. As consequence of the mutation in the NF1 gene, there will be abnormal ratios of cell proliferation and differentiation, causing the development of multiple benign tumors in various organs, mainly composed by Schwann cells and called neurofibromas. Those are the most prevalent tumors in patients with NF1 [2].

1.3. Brain morphologic alterations in NF1

The NF1 gene is highly expressed in the nervous system in both central and peripheral nervous systems (CNS and PNS respectively). Within the central nervous system, the NF1 expression is presented in cortex, hippocampus, cerebellum and brainstem [4]. This wide range of NF1 expression is likely to support the range of cognitive symptoms associated to CNS

dysfunction [4]. Indeed, in the past two decades important discoveries in the neuroimaging literature, linked the cognitive deficits identified in the NF1 disorder, to structural and functional brain phenotype abnormalities. These discoveries provided a greater focusing on the brain-behavior associations with NF1.

1.3.1. Macrocephaly

Macrocephaly is defined as an abnormal/exaggerated increase of the head circumference and it occur in approximately 50% of NF1 children [3]. Several factors can contribute to this enlargement: the greatest one is megalencephaly, an overwhelming increase of the brain volume [3, 17, 18]. It is known that white matter (WM) and gray matter (GM) have an important role in here [3]. Several MRI studies have already analyzed quantitatively the contribution of WM and GM in megalencephaly observed in NF1 patients, analyzing the volumetry from quantitative MR Images.

Steen et al (2001), examined 18 patients with NF1 (ages 6 to 16) and found that children showed enlarged brains structures, being associated with characteristic WM lesions (WML), causing an increase in the brain volume, during its development. Sevick et al (1992), compared the WM evolution in patients with NF1, and found WML especially in children, where they appeared in greater size and number. In 2005, Greenwood et al measured GM and WM volumes in lobar regions of the brain in children with NF1 and found a significant GM increase in occipital and parietal regions and a significant WM increase in regions proximate to the frontal lobe of the brain. A specific study was performed by Wignall in 2010, studying the differentiation of the corpus callosum microstructure in adults with NF1, using DTI volumetric imaging methodologies [19]. Indeed, the corpus callosum is referred as one of the brain anatomical structures with a major enlarging within the overall brain volume, in children with NF1 [1,18]. In his study, Wignall showed that this enlargement of the corpus callosum size found in children to be statistically significant was also present in adults with NF1, however the difference was not statistically significant in adults.

Although these studies are very interesting, it is not possible to make a general comparison between them, because they all followed different aspects and decisions taken during the acquisition procedure. For example, they all include a wide range of ages in control subjects and NF1 patients, as well as the nature of the control group varies between them, since non-genetically relate to genetically related [17, 20, 21]; and some studies have choose to analyze in detail the development of tumors, based by gender [18].

1.3.2. Myelin disorder

Besides brain volume increase, there is another major phenotypic alteration in the CNS of NF1 patients. This alteration is identified easily through MRI techniques as hyperintensities on T2-weighted images and known as unidentified bright objects (UBOs). Several MRI studies successfully found a correlation between UBOs and a myelinic alteration, more specifically a myelin disorder/disintegration and axonal disruption [22, 23, 24]. With the use of diffusion weighted imaging, it is possible to quantitatively differentiate between healthy volunteers and patients with NF1, with the analysis of isotropic scalar parameters, like apparent diffusion coefficient (ADC) as well as anisotropic ones, such as fractional anisotropy (FA) [6, 23]. Several studies, analyzing those two coefficients, as well as the eigenvalues extracted from the diffusion tensor of DTI data, reported an inverse alteration in FA and ADC values in UBOs identified in children and adults with NF1 [23, 24], with a FA decrease and a ADC increase. This seems to be a possible explanation for an axonal damage in the myelin of WM, identified by MR spectroscopy performed within the UBOs and apparently normal WM [23, 24, 25].

Chapter 2: Functional and anatomical organization of visual-callosal WM pathways

Since we will be analyzing the diffusion properties of water molecules in WM pathways connecting visual cortical areas in the occipital lobe, through the corpus callosum, it is necessary to understand the anatomical organization and function of these regions, in the transmission of visual information through the human brain.

2.1. Biological Background

The brain is the main organ and center of the nervous system, being an extremely complex and extensive structure. It is distributed by billions of cells composed of essentially two main tissues, which are the basis of its functional performance:

- WM composed by myelinated fibers (axons) and glial cells (oligodendrocytes are the most abundant) (figure 3A), connecting the neurons via fiber pathways The name of "WM" comes from the lipid-rich myelinated sheath that surrounds the majority of the CNS axons, rendering the tracts white (figure 3B) [26].
- GM, including the cerebral cortex, constituted by neurons forming regions involved in multiple performances, such as: sensory perception, memory, seeing and hearing, as well as muscle control. The GM is composed of dendrites, neuronal cell bodies, myelinated axons, unmyelinated axons, and glial cells (mostly astrocytes and oligodendrocytes).

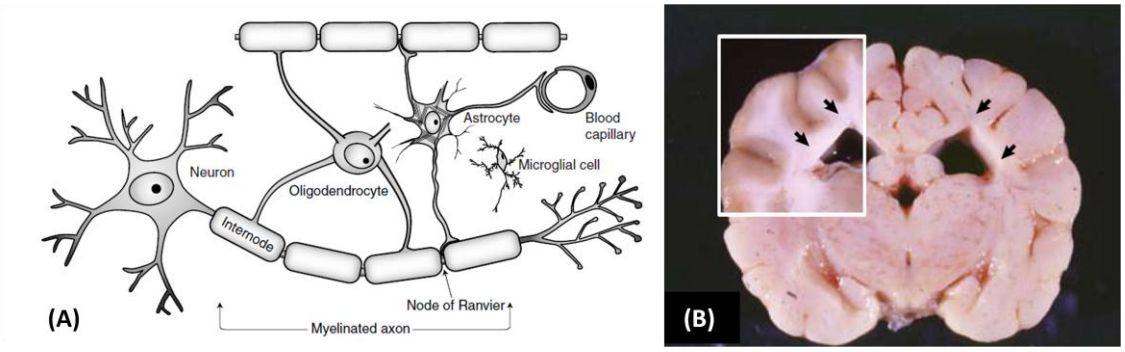

Figure 10: (A) Illustration of the main WM cellular elements. The neuronal cell body in the GM is connected with other via WM fiber pathways, along an axonal process. The axon is surrounded by a lipin-rich myelin sheath, produced by oligodendrocytes [26]. (B) The lipid-rich myelin sheath surrounding the axons, gives the WM its characteristic color [26].

2.2. Anatomy of the corpus callosum

The corpus callosum is a thick anatomical structure that separates the two brain hemispheres. It contains axons connecting both left and right sides of the brain, allowing the transmission of visual, sensory and cognitive information between them [27, 28]. It is located at the center of the brain (figure 5) and is considered the main WM fiber bundle within it [27].

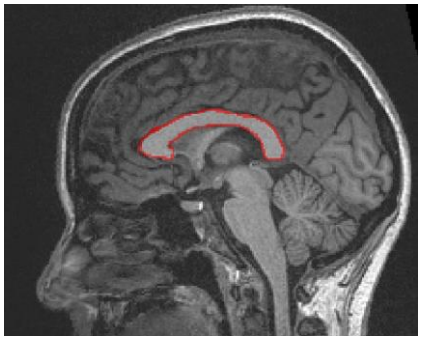

Figure 11: Sagital illustration of the corpus callosum in one of the control individuals

There are several studies reporting the importance of the corpus callosum role in the correct transfer of information between hemispheres and what is the relationship between its anatomical structure and its role in the transmission of information, especially cognitive information[27, 29]. In order to do so, two studies stood out, having established a topographical distribution on the corpus callosum of the fiber tracts connecting the cortex, from its anterior to its posterior portion [29, 30]. In these two studies, the corpus callosum was segregated in 5 distinct parts. The two definitions differ mainly at the anterior tip and midbody of the corpus callosum, where [30] divided one region on the anterior third and the other in the anterior midbody of the corpus callosum, while [29] divided the most anterior segment in one region covering the first sixth of the corpus callosum and the rest of the anterior half as the second region. Nowadays, the division of the corpus callosum performed by Hofer (2006) may be more viable, since it was performed in eight human subjects, while Witelson (1989) partitions were based in primate data.

So with Hofer's topography (2006), we can distinguish: axons in the genu of the corpus callosum (most anterior portion) connecting the prefrontal cortex of each brain hemisphere (Region I in figure 6); the anterior midbody of the corpus callosum, connecting the premotor and supplementary motor cortical areas (Region II in figure 6). The posterior half of the corpus

callosum is divided into three portions where fibers connect the primary motor (Region III in figure 6), sensory (Region IV in figure 6) and visual cortical areas (Region V in figure 6).

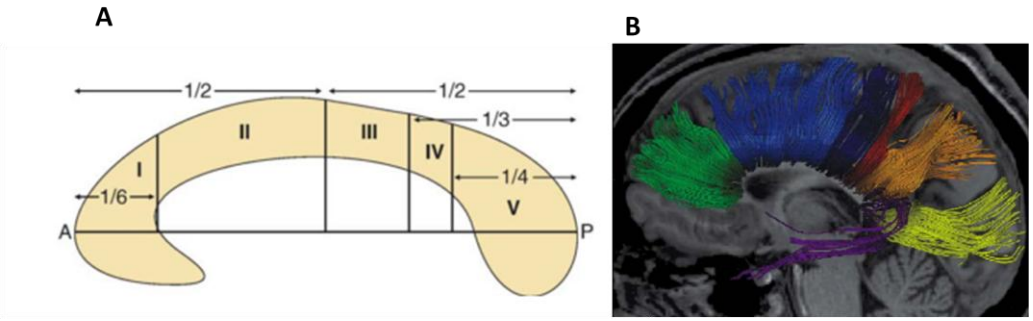

Figure 12: Topography of midsagittal corpus callosum proposed by S. Hofer, dividing it into 5 distinct parts; (B) 3D Sagital reconstruction performed by S. Hofer, of all callosal fibers, comprising fibers projecting into the prefrontal lobe (green), premotor and supplementary motor areas (blue), primary motor cortex (dark blue), primary sensory cortex (red), parietal lobe (orange), temporal lobe (violet) and occipital lobe (yellow) [29].

2.3. Visual cortex in humans

The human visual cortex comprises the grey matter in occipital lobe, organized in multiple functional areas involved in visual processing, and extends into the parietal and temporal lobes. The primary visual cortex, known as V1 or striate cortex is primarily responsible for transmitting visual information, from the retina to the other cortical regions of the visual cortex, known as extrastriate visual areas. Both the striate cortex and the extrastriate cortex visual areas contain an enormous interconnection between them and other cortical visual areas. Each cortical area can be strongly connected to between 5-10 other cortical areas [31, 32].

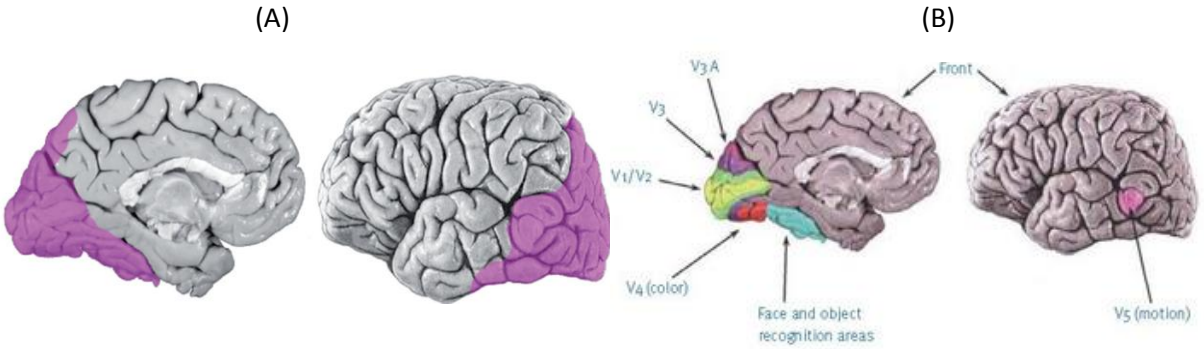

Figure 13: (A) Connections between cortical visual areas; The primary visual cortex V1 as being the visual areas with greater connections with other cortical areas, having direct connections with posterior extrastriate areas V2 and V3, as well as V3A, V4 and MT (Adapted from [31]); (B) Labelling of the areas of the visual cortex (V1, V2 and V3) according to their functionality: "V1 having to do with sorting the signals for various visual tasks, V2 and V3 relating to the perception of form" [31, 56]

2.4. Visual-Callosal WM pathways

The constituent fiber tracts of the brain's WM are essential for proper communication between distant cortical areas, commonly belonging to different brain hemispheres, with each area doing specific parts of a certain behavioral or cognitive tasks [33, 34]. These fiber tracts play a critical role in transferring information between different brain regions. Any damage to them, will affect this transfer, having specific consequences in different aspects of cognitive performance [33, 34, 35].

Regarding the characteristics of fiber tracts connecting areas of the visual cortex in both brain hemispheres, and which are of interest to our work, there are two MRI studies that analyzed those fibers. Dougherty et al (2005) identified them in 50 children; they are fiber bundles passing through the splenium of the corpus callosum and connecting the occipital lobes of each hemisphere [33, 34]. In 2007, Michael Ben-Shachar reviewed findings in the literature and identified three of the larger WM pathways associated to information communication through all the reading processing cortical areas in the brain. Between them he identified those passing also through the callosum and connecting both occipital lobes [35].

Focusing all efforts on the identification of visual-callosal fiber tracts, Dougherty et al (2005) identified a large fiber tract, passing through the central portions of the splenium of the corpus callosum and projecting to dorsal areas of the visual cortex [33, 34] (figure 8A). Ben-Shachar et al (2007) identified the same fibers, projecting to occipital and temporal cortexes (figure 8B), highlighting their importance on the DTI study performed by Dougherty et al (2005) [35].

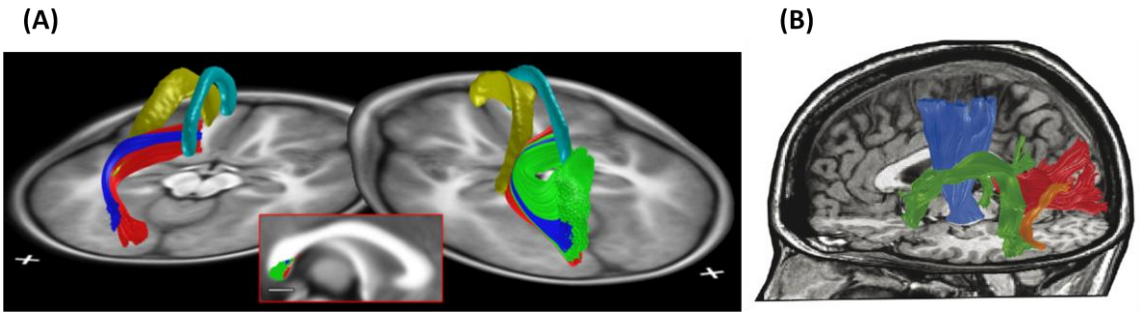

Figure 14: (A) Occipital-callosal fiber tracts identified by Dougherty, connecting both occipital lobes of each brain hemisphere through the corpus callosum. On the image on the left are identified the fibers projecting to lateral (blue) and ventral (red) occipital lobes; in yellow, are identified the fibers passing on the two sides of the ventricle. The image on the right correspond to a different view of the same fiber tracts, where Dougherty identified the fiber tracts projecting to dorsal regions of the occipital lobe (green color) [33]; (B) WM pathways essential to the proper communication between read processing regions of the brain, identified by Ben-Shachar (2007); In the image it can been identified in red the occipital-callosal fibers, similar to the ones identified by Dougherty (2005), as well as, temporal-callosal fibers [35].

Chapter 3: Magnetic Resonance Imaging – an Overview

By combining a strong magnetic field with radio waves, magnetic resonance imaging (MRI) produces detailed and high-resolution brain images without using potentially harmful radiation.

3.1. Spin's characteristics in the magnetic field

The MR phenomenon is based on the fact that nuclei of atoms have magnetic properties. Nucleuses with an overall nuclear spin (I) different of zero (^{1}H, ^{13}C, ^{31}P) are susceptible to the MR technique.

The spin is a vector physical property of the matter and it is proportional to h, Planck's constant, and to *I* which is an integer for Bosons and a semi-integer for Fermions. Fermions obey Pauli's exclusion principle, while Bosons do not, which implies that Fermions have a strong tendency to not occupy the same energy level, and hence to not occupy the same physical space. The particles that constitute the stable atoms (protons, neutrons, and electrons) are all of them Fermions with *I=±½* (equation 1). But pairs of Fermions, because of Pauli's exclusion principle, have a tendency cancel each other's spin. Thus, atomic nuclei with an even number of nucleons of the same type have a spin equal to zero. As an example, oxygen has 16 nucleons, 8 protons and 8 neutrons. Since both types of nucleons have an even number of elements, the spin of the oxygen nucleus is equal to zero. The z-axis component of the spin is:

$$S_z = \frac{h}{2\pi}.I \quad (1)$$

The spin's magnetic moment (μ) is proportional to the spin, and the proportionality constant is the gyromagnetic coefficient (γ):

$$\vec{\mu} = \gamma.\vec{S} \quad (2)$$

The gyromagnetic coefficient (γ) value depends on the element that is being considered.

The molecule normally used in clinical MRI acquisitions is water; the use is due to its abundance in the human body, giving a large magnetic moment. Since oxygen has a spin of zero, the water molecule can be approximated as two independent hydrogen nucleus. The Hydrogen nucleus contains a single proton, and it is quite simple to model. If there is no

magnetic field interacting with the spins (figure 1a), the earth magnetic field is not strong enough to orient the spins of water in a non-random fashion [36], and so the magnetization (M), the sum of all spin magnetic moments, at room temperature in biological tissue will typically be zero:

$$\vec{M} = \sum \vec{\mu} = 0 \quad (3)$$

3.2. Precession

With the presence of a strong magnetic field applied in a certain orientation, the water's proton spin will tend to point either parallel or anti-parallel to the direction of the applied magnetic field (B_0) (figure 1b). For the proton, the parallel orientation has the lowest energy difference (ΔE) to the state of there being no applied field; and so using Boltzman's distribution, $Probability = e^{-\frac{\Delta E}{KT}}$, it is the more likely orientation where *K* is Boltzman's constant and *T* is the temperature. It is appropriate to use the Boltzman distribution as an approximation to the Fermi-Dirac distribution, because the temperature T considered is sufficiently higher than the absolute zero.

The difference of probability between the parallel and the anti-parallel case allow for the existence of an average magnetization parallel to the applied magnetic field. Due to several factors like spin collisions, inertia and random spin motion, the spins rotate around the main magnetic field axis, instead of aligning parallel or anti-parallel with it. This process is called precession (figure 10a), and the rate at which the spins rotate (Larmor frequency, w_0) its related with the speed and strength of the main magnetic field (B_0), as shown in equation 4 [36, 37]:

$$w_0 = \gamma . B_0 \quad (4)$$

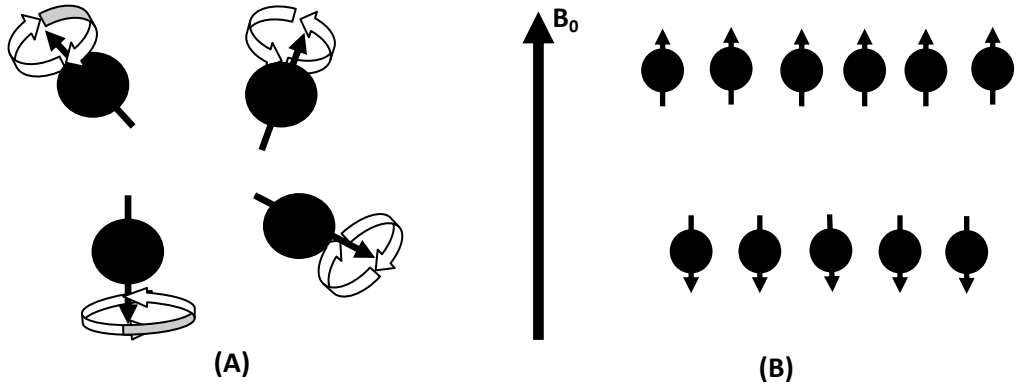

Figure 9: Magnetization in two different situations: (A) Natural state, with no magnetic field applied to the spins; (B) Application to a magnetic field B_0 with a certain speed and strength. (Adapted from [36])

The magnetization (M) can be separated into two magnetizations, each one of them corresponding to a component of the magnetic vector of spinning protons: longitudinal magnetization (M_z) pointing in the z-direction which by definition is parallel to applied magnetic field (B_0), and a transversal magnetization (M_{xy}), lying in the xy-plane (figure 2b)

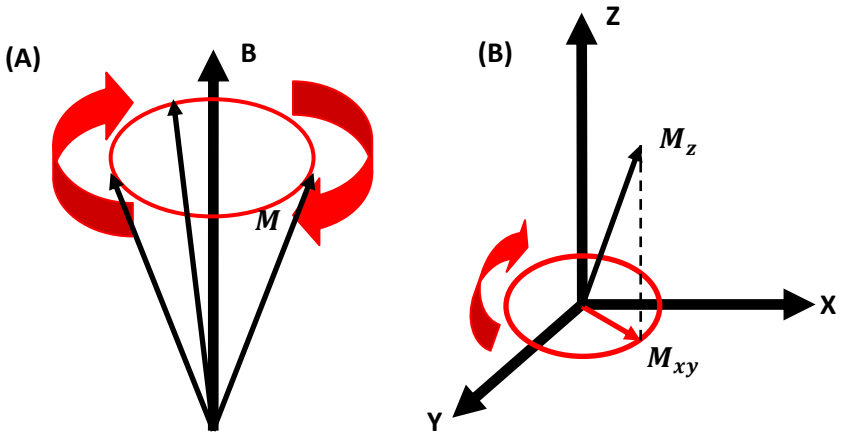

Figure 10: (A) Spinning precession around B_0 at the Larmor frequency; (B) The magnetic vector M can be separated in two different components: longitudinal magnetization (M_z) along the z-axis and transversal magnetization (M_{xy}) on the xy-plane. (Adapted from [36])

According to equation 4, to each strength of the applied magnetic field there corresponds an oscilation frequency. Also, to the energy difference between parallel and anti-parallel proton spins there also corresponds a frequency. The first frequency is called the Larmor frequency, and the second is called the resonance frequency. In MRI, and NMR, where the transition is between consecutive energy levels, such as in water, the Larmor frequency is

equal to the resonance frequency. And so they are often named indistinctively. Application of a pulse-sequence where a magnetic field is rotating with the Larmor frequency will be constituted by photons with the appropriate resonance frequency. The application of RF pulses by a transmitter RF-coil with the appropriate frequency to protons will cause them to absorb energy, and the magnetic field associated to the RF pulse will make the magnetization rotate orthogonally to the z-axis and onto the xy-plane. If the timing of the magnetization rotation is such that the magnetization is rotated 90º, the all longitudinal magnetization will be converted into traverse magnetization (figure 11) [36, 38]. The continuing existence of the applied magnetic field B_0 will make the magnetization rotate at the Larmor frequency which will have a similar effect to an electrical generator, and will thus induce a time-changing magnetic field with a Larmor frequency. According to Maxwell-Faraday's equation the time-changing magnetic field will induce a time-changing electromotive force. The time-changing electromotive force will induce a time-changing electric-potential difference in the receiving RF-coil. That time-changing electric potential difference along each loop of the coil is what constitutes the MR signal [37].

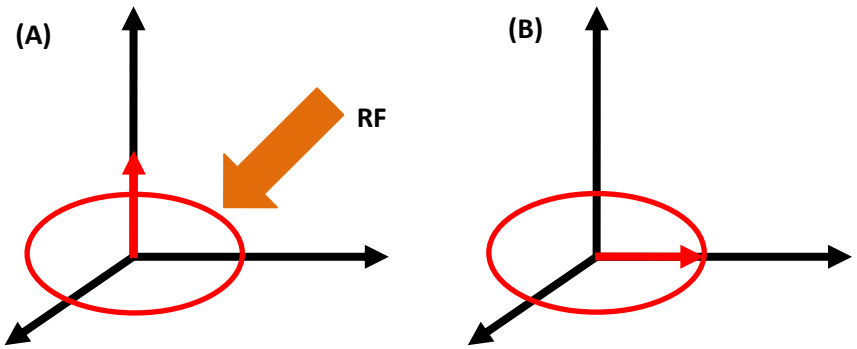

Figure 11: (A) a RF pulse turns the magnetization by exactly 90° into the xy-plane, causing the entire longitudinal magnetization (M_z) to transform into traverse magnetization, (M_{xy}) (B). (Adapted from [36])

3.3. Relaxation

The process described above is known as the spin's excitation, in the presence of a strong applied magnetic field. The continued application of the strong magnetic field after the RF pulse stopped will make the spins to return to their statistical equilibrium situation where the magnetization was pointing in the z-axis, and where there was no net magnetization in the xy-plane. The time of reappearance of the longitudinal (z-axis) magnetization is called T1, and the time of disappearance of transverse (xy-plane) magnetization is called T2. The magnetization is said to "re-appear" if it recovered e^{-1} of its maximal strength, and it is said to

"disappear" if it lost e^{-1} of its maximum strength. Consequently, after excitation the MR signal gradually fades with the restoration of longitudinal magnetization and reduction of the transverse magnetization, notice that the amplitude of the magnetizations is not preserved since T1 is different from T2. The fading of the MR signal is called relaxation and it will cause the system to reach the stable state it had before the excitation process [36, 37].

3.3.1. T1: Longitudinal relaxation

With T1 relaxation, transverse magnetization fades and the magnetic moment will progressively realign with the z-axis of the main magnetic field (B_0) (figure 12). The projection of the magnetic moment onto the z-axis is restored, the MR signal will fade proportionally, as the transverse magnetization decreases in the xy-plane [36]. The longitudinal magnetization recovery rate is characterized by a constant known as the time constant T1. After a T1 time, longitudinal magnetization will have recovered 63% of its value before excitation. Considering the beginning of T1 relaxation, when longitudinal magnetization has a null value (90º RF pulse), its regrowth is given by the following equation:

$$M_z(t) = M_0\left(1 - e^{\frac{-t}{T_1}}\right) \quad (5)$$

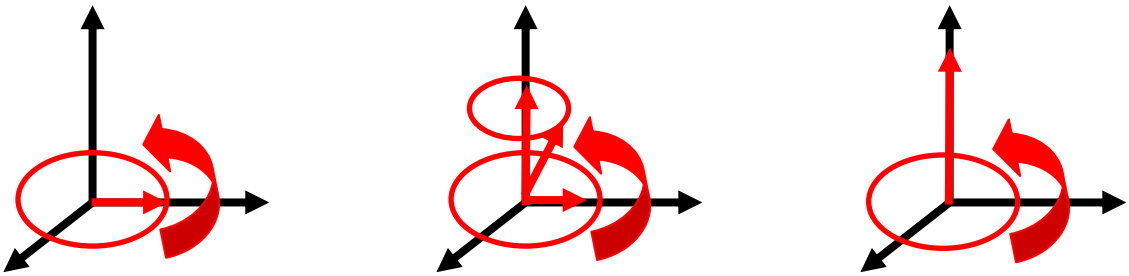

Figure 12: T1 relaxation process; Decay of transverse magnetization within the xy-plane and realignment of the longitudinal magnetization with the z-axis. (Adapted from [36])

3.3.2. T2/T2*: Transverse relaxation

With T2 relaxation, the spins pointing orthogonally to the main magnetic field will lose phase coherence, because of the interaction of the magnetic fields of each spin, progressively modifying their precession rate. Losing phase coherence will cause transverse magnetization to decay (figure 5), being this decay of magnetizations on the xy-plane described by the following equation (6). The transverse magnetization decay is characterized by a time constant T2 (always shorter than T1). After a T2 time, the transverse magnetization has already lost 63% of its initial value before relaxation.

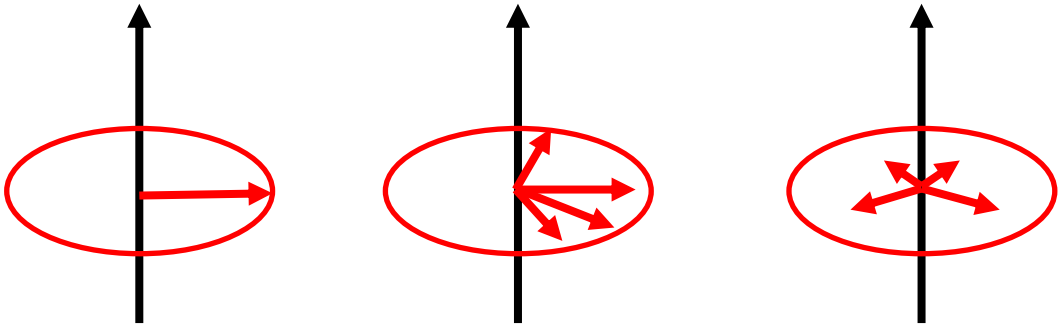

Figure 13: T2 relaxation; Spins lose phase coherence and transverse magnetization decays progressively. (Adapted from [36])

$$M_{xy}(t) = M_{xy}(0)e^{\frac{-t}{T2}} \quad (6)$$

Transverse magnetization dephasing can occur on two different ways:

1. Spin-spin interaction, with energy transfer/exchange between spins;
2. Influence of inhomogeneities caused by the main magnetic field B_0 or by the person being imaged. Those Inhomogeneities contribute to transverse magnetization dephasing at a time constant even shorter than T2, called T2*. This characteristic time constant T2* is what is observed when the MRI technique used is for example a Free Induction Decay (FID) or a gradient echo (GE) pulse sequence.

3.4. 180° pulse and obtaining of the spin-echo signal (T2*)

In the transverse relaxation, magnetic field inhomogeneities can be divided into a time-dependent and a time-independent component. The inhomegenities in the appled magnetic field are time-independent, while inhomogeneities in the biologically-induced (e.g. the magnetic field generated by deoxygenized hemoglobin) is partly time independent and partly time-dependent. In a spin-echo pulse sequence the phase induced by magnetic field inhomogeneities' is inverted by a 180° phase reversal pulse sequence at a time $T_E/2$ after the 90° RF pulse. For the component of the magnetic filed inhomogeneity that is time-independent, the phase generated by the inhomogenity until the time $T_E/2$ is equal to the phase induced between time $T_E/2$ and time T_E. But since the phase was completely inverted at time $T_E/2$, at the time T_E the time-independent inhomogeneity-induced phase is completely

cancelled [36, 37] (figure 14). The 180° RF pulse is identical to the 90° excitation pulse except that it runs for twice the time.

The time between the application of a 90° RF pulse and the 180° RF pulse is called a run time (τ). With the application of the 180° RF pulse, the spin echo increases its signal and reaches its maximum after a double run time (TE=2 τ) [37, 39]. As mentioned before the fast/slow time-independent spin distribution will reverse with the 180° RF pulse, placing the spins with greater precession rate "behind" the slow ones [36]. After this pulse, the spins will be back in phase, with the fast/slow spins "catching up" after an echo time (TE: time between a 90° RF pulse and the MR signal sampling). The Repetition time (TR) will correspond to the time between two consecutive 90° RF (excitation) pulses [36, 37].

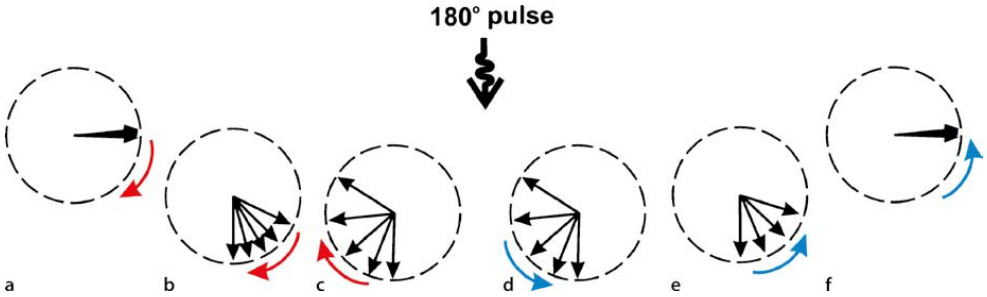

Figure 14: Spin-echo [a-f]; Illustration of transverse magnetization dephasing, after the application of a 90° RF pulse [a-c]; with the application of the 180° RF pulse, the spins will be back in phasing, converging to coherence after a echo time (TE) [36]

When we have a sequence of 180° RF pulses, we obtain the several spin-echoes of a multi-echo sequence. The amplitude and strength of each spin-echo signal will be strongly related to the echo time (TE): the larger the TE, the smaller the echo will be, and this process will repeat itself until T2 relaxation is fully completed, and transverse magnetization is lost (figure 15) [36, 37].

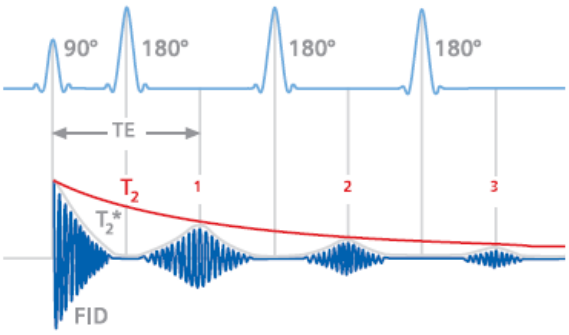

Figure 15: Multi-echo sequence; Illustration of spin-echo signal decrease with T2* [39]

3.5. Gradient echo sequence

The gradient echo (GE) sequence is usually applied when shorter TR and TE and consequently shorter scan and acquisition times are required. It differs mainly from the spin-echo sequence on the use of a flip angle below 90° for spin excitation, and the presence of a magnetic field gradient reversal instead of the 180° rephasing pulse. With the use of a partial flip angle, the longitudinal magnetization will require a shorter time for full recovery of its value, allowing a shorter TR and TE. Due to the use of a gradient reversal, instead of the 180° rephasing pulse, only the applied magnetic filed inhomogeneities will be cancelled. Meaning that the biologically induced magnetic field inhomogeneities will not be cancelled making the transverse magnetization disappear faster, T2*, than for the spin-echo pulse sequence (T2* is always smaller than T2).

3.6. Echo planar Imaging sequence

Echo planar Imaging (EPI) sequence is the fastest acquisition method applied in MRI, reaching an acquisition time of 100ms per slice, but with a considerable spatial resolution limitation. It is based on the following aspects:

1. The excitation pulse;
2. A continuous MR signal acquisition to acquire the total or a partial portion of k-space, depending on the type of acquisition (single shot versus segmented acquisition);
3. Phase-encoding in the y-axis, in order to fill the y-component of the k-space;
4. Read-out in the x-axis, in order to fill-out the x-component of the k-space.

3.7. Image contrast

T1 and T2, as well as the proton density of the tissue being considered, are essential features for the image contrast. Different tissues have differing values of at leats one of these parameters, and so their combined measurement allows the determination of the volume in some cases the physiological condition of different types of tissue [36, 37].

3.7.1. Repetition Time (TR) and T1-weighting relation

Repetition time (TR) and T1 relaxation are two MRI features closely related to each other, since TR defines the relaxation period between two excitation pulses (90° pulses). When a long TR is selected, there will be more spins rotating to the z-axis and therefore contributing to the regrowth of the longitudinal magnetization [37. With a short TR, the image contrast will be affected in greater scale by T1.

Tissues with a short T1 will relax quicker, giving a larger signal with the next RF pulse [37]. With a long T1, the spins relax more slowly and the longitudinal magnetization will be smaller when the next excitation pulse is applied, emitting less signal than the tissues with short T1 (figure 16).

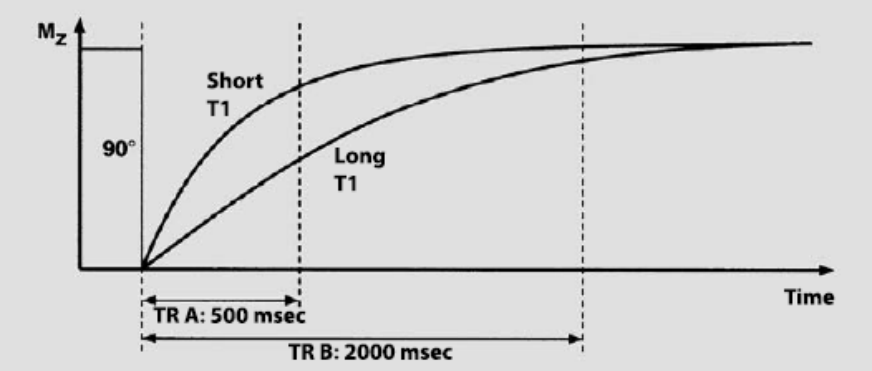

Figure 16: Relation between repetition time (TR) and T1 contrast; With a long TR, all tissues with long or short T1 will have time to recover full longitudinal magnetization, having as a result a small T1 contrast effect on the acquired image [37].

With a short T1, we acquire a T1-weight image, containing mostly T1 information. With a long T1, all tissues will have available time to return to equilibrium after the 90° RF pulse application giving all of them a similar MR signal [37].

3.7.2. Echo time (TE) and T2-weighting relation

The T2 contrast effect on the MR image is closely related with TE. With a short TE, the tissues will have a smaller signal difference between them, due to the little signal decay, at the time of echo collection [36, 37]. The resulting MR image will have a low T2-weighting. Otherwise if a longer TE is selected, the difference between tissue signals will be bigger, acquiring a better contrast between the tissues in the resulting MR image, thus obtaining a better T2 weighting (figure 17). However, the T2 of the tissue will also have a considerable

effect in the acquired MR image: with a short T2, the tissues will lose most of its MR signal appearing dark on the MR image; a longer T2 will produce a stronger signal in the tissues and thus appearing bright [37].

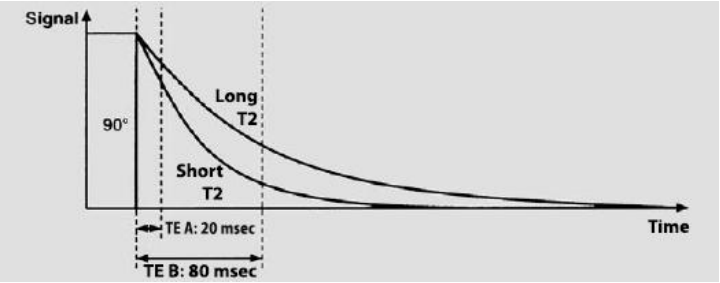

Figure 17: Relation between echo time (TE) and T2 contrast; a shorter T2 will result in a greater MR signal lost, with the appearance of darker tissues, making hard to distinguish them, while a longer T2 will result in a stronger signal thus, the tissues will appear bright [37].

3.8. MR systems and main components

The MRI device relies on four main hardware components: main magnet, gradients, radio frequency coils, and the computer systems. The junction of these four systems forms the MR device, and is represented in figure 18A:

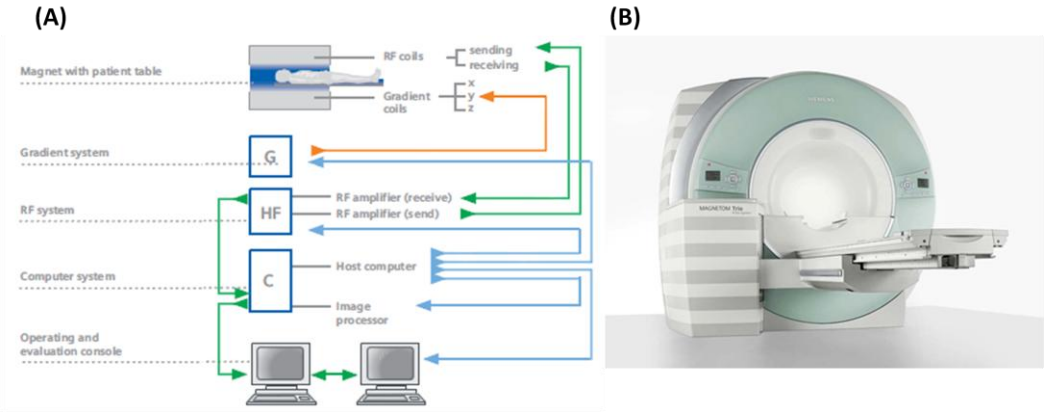

Figure 18: (A) MRI device main components [39]; (B) Representation of a 3T Siemens MRI scanner [53].

3.8.1. The main magnet

This component is the most critical and expensive of the MR device. It purpose relies on the creation of a strong magnetic field (in medical imaging it usually ranges from 1.5 to 3

T), highly stable and with no field strength fluctuations. There are three types of magnets available:

- Resistive magnets, which depend on a great and constant amount of power supply; the magnetic field reaches a maximum strength of 0.3T.
- Permanent magnets consisted of ferromagnetic substances, creating a magnetic field, which does not need an external power supply and reaches a maximum strength of 0.5T.
- Superconducting magnets consisted of coils made of niobium titanium (Nb-Ti) alloy; the magnetic field is also maintained without any external power supply, reaching strengths of 18T. They are the typically used in medical and neuroscience applications.

3.8.2. The Gradient system

This system consists of three gradient coils, each one corresponding to each spatial direction (x, y and z). The generated magnetic field is not permanent and so, these coils are instead switched on/off for several times during the MR acquisition.

The generated gradients are essential for the signal spatial encoding, where each gradient produces a linear variation along each of the considered directions.

3.8.3. The Radio Frequency system

This system, as its name says, contains a powerful radio frequency generator and a receiver with high sensitivity. Any instability between those two components, the transmitter and the receiver coils, will cause distortions in the magnetic field, resulting in the acquisition of a blurred image.

3.8.4. The Computer system

This system controls the gradient activation, as well as the radio frequency coils coordination for data management and image processing.

Chapter 4: Diffusion Weighted (DW) Magnetic Resonance Imaging (MRI)

4.1. What is diffusion?

Diffusion is the name given to a transport process present in nature, which involves molecules or particle mixing without the requirement of bulk motion [26]. It is explained by Langevin's Brownian motion equation that can be approximated by Fick's first physical law, relating the flux of molecular diffusion to any concentration alteration in the particle's environment:

$$J = -D\nabla C \quad (7)$$

This physical relation implies that when the specimen is composed by regions with different molecular concentrations, the particles will tend to be transferred from regions with higher to lower molecular concentrations, as represented in figure 11. This diffusion transport leads to a net flux (J) proportional to the diffusion coefficient (D) and gradient concentration (C).

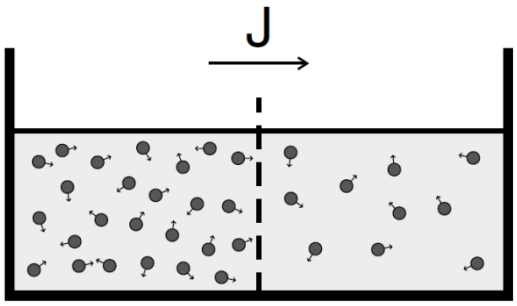

Figure 19: Fick's first law, illustrating a molecular diffusion transport between regions with different concentrations and with a diffusion tendency from regions with higher to lower concentrations [26].

4.2. Magnetic Resonance (MR) and Diffusion relationship

Diffusion processes of molecular transport are highly dependent on the anatomical structure of the environment being analyzed, and so magnetic resonance (MR) is a useful technique in acquiring this structural environment information with non-invasive procedures.

Gradient pulse application

During the spin's dephasing, spins acquire different phase shifts between them, depending on the magnetic field applied at their respective location. In order to control those different spin phase changes across the specimen, diffusion-sensitizing magnetic field gradients are applied. Those diffusion-sensitizing gradients are much stronger than the gradients applied for space localization, and they typically consist of two gradients each lasting a time δ and their start separated by a time Δ; one gradient occurs before and the other after the 180° RF pulse. If the molecules do not move the phase induced by the first gradient is cancelled by the second gradient; if the molecules move in a certain direction then the signal will gain a phase when the diffusion sensitizing gradient is applied on the direction; but if the molecules do not have a bet flow and simply diffuse then each molecule will gain a different phase depending on their movement but the average of the dephasings will be zero. The magnetization will be reduced by the molecular diffusion because the dispersion in all directions of the spin's phases will reduce their overall sum, but the net magnetization at the echo will point in the same direction as before the application of the diffusion-sensitizing gradients. Because the reduction of the MR signal at the echo is in this situation strongly influenced by the molecular diffusion, the reduction of the MR signal intensity indirectly measures the diffusion coefficient of the liquid system being examined [26, 40]. This indirect measurement utilizes several elaborate mathematical techniques, some of which will be described in later sections. This approach was first introduced by Stejskal and Tanner (1965), allowing a proper distinction between the encoding and the diffusion time for the diffusion coefficient measurement, as illustrated in figure 20 [26].

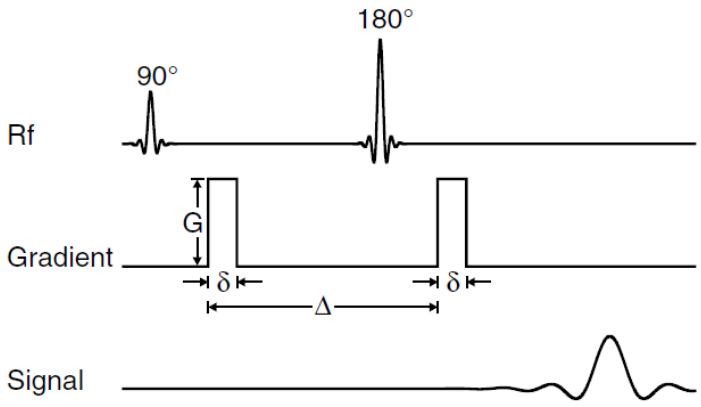

Figure 20: Illustration of the pulsed field gradient spin-echo MR sequence approach introduced by Stejskal and Tanner. The time between the two gradient pulses is denoted by Δ and δ as the pulse duration [26].

Considering an MR acquisition sequence with the application of two gradient pulses, as illustrated in figure 2, the change of the spin particle's net phase during the application of each gradient pulse is, if x_1 is the location of the molecule during the first gradient and x_2 the location during the second gradient, are given respectively by the two following equations [26]:

$$\varphi_1 = -qx_1 \quad (8)$$

$$\varphi_2 = -qx_2 \quad (9)$$

The vector $\vec{q} = \gamma\delta\vec{G}$ where γ is the gyromagnetic constant, and $\vec{G}$ is the gradient vector. Because of the application of the 180° RF pulse, the net phase change induced by the first gradient pulse will be reversed and so the phase shift will be [26]:

$$\varphi_2 - \varphi_1 = -q(x_2 - x_1) \quad (10)$$

4.2.1. MR signal attenuation

In the case the particle remains stationary (x_2=x_1), the diffusion-sensitizing gradients will have no effect on the MR signal. If we have random particle diffusion, the phase decrement after the application of the second gradient is not necessarily canceled by the phase increment with the first gradient pulse, and so this discrepancy will result in phase dispersion among the spin's population moving randomly [26]. As a result, there will be a MR signal attenuation (E(q)) on the overall MR signal (S), given by the following equation [26]:

$$E(q) = \frac{S(q)}{S_0} \quad (11)$$

where S(q) is the diffusion-attenuated signal and S_0 the diffusion-attenuated signal without the appliance of any gradient. The MR signal attenuation will eliminate any effect of MR relaxation and so, the q-dependence of E(q) will be only attributed to diffusion [26], as shown in equation 12:

$$E(q) = \int \rho(x_1) \int P(x_1, x_2, \Delta) e^{-iq(x_2 - x_1)}\, dx_2\, dx_1 \quad (12)$$

Where $\rho(x_1)$ represents the spin density when the first gradient is applied.; $P(x_1, x_2, \Delta)$ is the diffusion propagator (a Green's function), denoting the probability that the particle, initially at position x_1, becomes located at position x_2 at the end of the second gradient pulse.

In the case of free diffusion, the diffusion propagator is a Gaussian distribution and taking in consideration the pulse's duration, the MR signal attenuation is given by [26]:

$$E(q) = e^{-q^2 D\left(\Delta - \frac{\delta}{3}\right)} = e^{-bD} \quad (13)$$

$$b = q^2\left(\Delta - \frac{\delta}{3}\right) = (\gamma \delta G)^2\left(\Delta - \frac{\delta}{3}\right) \quad (14)$$

The b-value describes the strength of the diffusion weighting [26, 40]. The diffusion process is described by a second order symmetric tensor, and the diffusion propagator, the P-function, is described by the following equation [40]:

$$P(x,t) = \frac{1}{(4\pi t|D|)^{\frac{3}{2}}} e^{-\frac{x^T D x}{4t}} \quad (15)$$

Where *x* is the particle current position, *t* represents the time moment and *D* denotes the second order diffusion tensor. The methods used for the quantitative extraction of its components will be explained next.

4.2.2. Apparent diffusion coefficient (ADC)

For each voxel of an acquired diffusion-weighted (DW) the intensity at that voxel can be described by equation 16, where the signal without any gradient (S_0) will only depend on the chosen MR sequence type and duration. The gradient strength (*G*), duration (*δ*), interval period between two gradient pulses (*Δ*), as well as the unit-vector direction ($\vec{u}$) will constitute the diffusion parameters connected to the MR diffusion attenuation. The apparent diffusion coefficient (*ADC*) will represent the diffusion coefficient defined by the applied gradient along a particular direction:

$$S(\vec{u}) = S_0 e^{-(\gamma \delta G)^2 \Delta\left(ADC_{\vec{u}}\right)} = S_0 e^{-b\, ADC_{\vec{u}}} \quad (16)$$

$$ADC_{\vec{u}} = \vec{u}^T \cdot D \cdot \vec{u} \quad (17)$$

According to equation 9, an increase in the b-value will come with an increase in any of the following parameters: gradient strength (G), duration (δ), gyromagnetic constant (γ), aand/or the period between the start of the two gradient pulses (Δ).

As shown in equation 16, dividing the measured *S* signal by the signal measured without any diffusion-sensitizing gradient, we will obtain the diffusion attenuation information (*E(q)*). This attenuation can be further described by the gradient projection on the diffusion

tensor, and consequently by its association with equation 17, the ADC value can be denoted as the projection of the diffusion tensor on the gradient's direction [26, 40]:

$$ADC_{\vec{q},\Delta} = \frac{ln\left(\frac{S_{\vec{q},\Delta}}{S_0}\right)}{|\vec{q}|^2 \Delta} \quad (18)$$

4.2.3. Diffusion Tensor Imaging

In this subsection the aim is to describe how the diffusion's directional information is extracted from a multi-directional 3D acquisition. The data acquisition is performed with low angular resolution diffusion imaging (LARDI).

When there is tissue organization, for example the brain's WM and GM, the water molecules' motion can no longer be adequately described with an ADC [40]. A more complex mathematical model is required for a proper characterization of the diffusion when the water molecule displacements' capacity is not equal in all directions. This different mathematical model is called the "diffusion tensor" and it will correspond to a different P-function as described in the previous sub-section. The diffusion tensor will be a 3x3 symmetric and second order matrix, describing the diffusion displacements of water molecules in 3D [26, 40]:

$$D = \begin{bmatrix} D_{xx} & D_{xy} & D_{xz} \\ D_{xy} & D_{yy} & D_{yz} \\ D_{xz} & D_{yz} & D_{zz} \end{bmatrix} \quad (19)$$

The diagonal elements describe the water diffusivity along the orthogonal axes of the reference frame, while the off-diagonal axes will correspond to the correlation between the molecular diffusion displacements located in the diagonal orthogonal directions in a given time. The eigenvalues of the diffusion tensor are (λ_1, λ_2 and λ_3), and they correspond to the eigenvectors with unit vectors (ε_1, ε_2 and ε_3), and the magnitude of the water diffusion along those vectors is described by their correspondent eigenvalue. We follow the usual choice of notation, which considers that in all cases $\lambda_1 \geq \lambda_2 \geq \lambda_3$.

It is extremely important to understand the fact that an off-diagonal element (e.g. D_{xy}) is not the measured ADC when $\vec{q}$ points in the $\hat{x} + \hat{y}$ direction, the ADC_{xy}; but rather, it is equal to: $\hat{x}^T \cdot D \cdot \hat{y}$. Figure 21 describes a particular case where this fact can be verified [26];

in figure 21b one has $D_{xy} = 0$ and $ADC_{xy} = \frac{\lambda_1+\lambda_2}{2}$; while in figure 21a one has $D_{xy} = \frac{\lambda_2-\lambda_1}{2}$ and $ADC_{xy} = \lambda_2$.

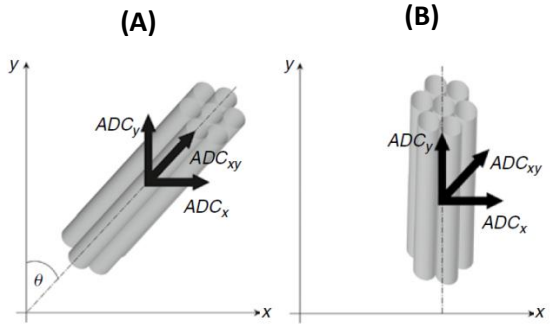

Figure 21: Difference between an off-diagonal element of the diffusion tensor and the respective apparent diffusion coefficient; (A) In this case the diffusivity along the x-axis is equal to the one along the y-axis, because of the anisotropy orientation at 45 degrees to both of them. In this case the displacements along the two are perfectly correlated; (B) In this case, x-axis and y-axis displacements are no longer correlated, being D_{xy} equal to zero, however the ADC along the x-y axis is not zero [26].

The eigenvalues can be properly written in the following general (20) and consequently, the diffusion tensor is given by the general mathematical system (21) [40]:

$$\forall_{x\neq 0}\exists_{\lambda,\varepsilon\neq 0}, Dx = \lambda\varepsilon x \Rightarrow (D-\lambda\varepsilon)x = 0, \text{since } x \neq 0 \quad (20)$$

$$D = \lambda\varepsilon \Leftrightarrow \begin{bmatrix} D_{xx} & D_{xy} & D_{xz} \\ D_{xy} & D_{yy} & D_{yz} \\ D_{xz} & D_{yz} & D_{zz} \end{bmatrix} = \begin{bmatrix} \lambda_1 & 0 & 0 \\ 0 & \lambda_2 & 0 \\ 0 & 0 & \lambda_3 \end{bmatrix} . \begin{bmatrix} \varepsilon_{1x} & \varepsilon_{1y} & \varepsilon_{1z} \\ \varepsilon_{2y} & \varepsilon_{2y} & \varepsilon_{2z} \\ \varepsilon_{3z} & \varepsilon_{3z} & \varepsilon_{3z} \end{bmatrix} \quad (21)$$

The eigenvalues λ_1, λ_2 and λ_3 are the diffusion coefficients in the respective directions ε_1, ε_2 and ε_3, being visualized as an 3D ellipsoid, given by equation 22 and properly illustrated in figure 22:

$$\frac{x^2}{\lambda_1^2} + \frac{y^2}{\lambda_2^2} + \frac{z^2}{\lambda_3^3} = 1 \quad (22)$$

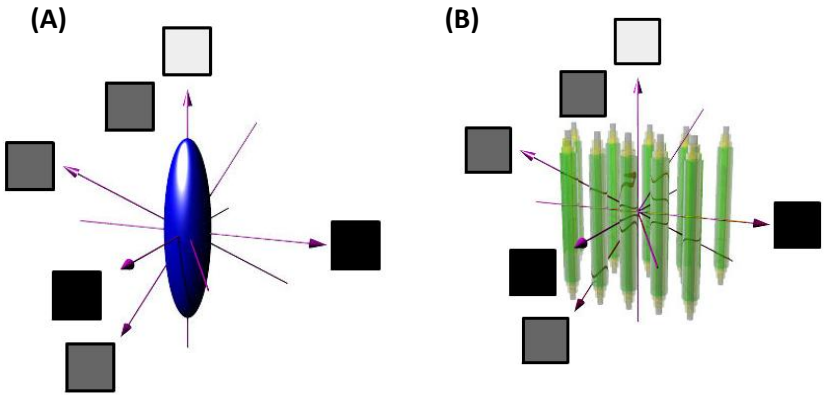

Figure 22: (A) Illustration of the diffusion tensor as a 3D ellipsoid and respective diffusion-weighted acquisitions acquired from the 6 possible directions. From each acquisition it is possible to extract the diffusion tensor synthesizing all the diffusion data; (B) Association of the diffusion tensor ellipsoid to an illustrative water molecule diffusion anisotropy in the brain's WM, where the molecules follow the direction of the fibers, being restricted perpendicularly to them. From each direction, we can see the different diffusion-weighted acquisition contrasts [54].

The main axis lengths of the 3D ellipsoid are equal to twice the eigenvalues for those axis, allowing for a proper presentation of the diffusion coefficient proportions and the diffusion direction's [26]. λ_1 is the largest eigenvalues of the diffusion tensor, and it is associated to the apparent diffusion coefficient parallel to the fiber length, while the two smaller ones (λ_2 and λ_3), are associated to the apparent diffusion coefficient perpendicular to the fiber (figure 23)

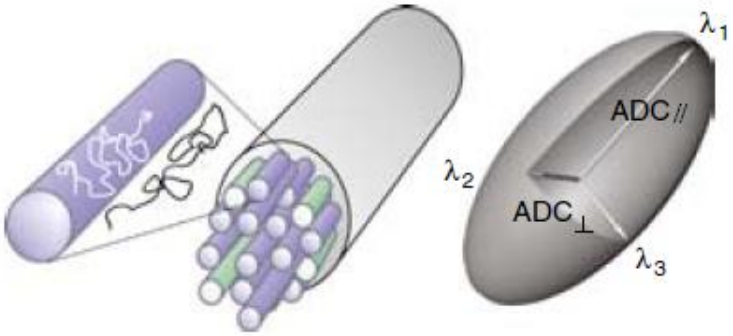

Figure 23: Water molecule diffusion associated to a diffusion ellipsoid, where two types of diffusion are established: diffusion parallel to the fiber length associated to the major eigenvalue ($\boldsymbol{\lambda_1}$) of the diffusion tensor, and perpendicular diffusion associated to the two smaller eigenvalues ($\boldsymbol{\lambda_2}$ and $\boldsymbol{\lambda_3}$) [26].

With the decomposition of the diffusion tensor in those eigenvalues and eigenvectors, it is possible to characterize the water molecules diffusion in the directions where it is not

restricted. The eigenvector corresponding to the highest eigenvalues will point in the orientation of the most efficient water molecule movement [40].

The estimation of the diffusion tensor is possible through the DW-MRI signal acquired and a series of mathematical routines. If one starts with a B matrix (equation 24) where *n* is the number of measurements performed during the MR acquisition in its rows, and each column element being: $b_{ij} = (\gamma\delta G_i)(\gamma\delta G_j)\left(\Delta - \frac{\delta}{3}\right)$. Then using the D' vector (equation 18) composed by the elements of the diffusion tensor, one can obtain the X vector containing the log-transformed signal intensities [26, 40]:

$$B = \begin{bmatrix} b_{xx}^1 & 2b_{xy}^1 & 2b_{xz}^1 & b_{yy}^1 & 2b_{yz}^1 & b_{zz}^1 \\ b_{xx}^2 & 2b_{xy}^2 & 2b_{xz}^2 & b_{yy}^2 & 2b_{yz}^2 & b_{zz}^2 \\ \vdots & \vdots & \vdots & \vdots & \vdots & \vdots \\ b_{xx}^n & 2b_{xy}^n & 2b_{xz}^n & b_{yy}^n & 2b_{yz}^n & b_{zz}^n \end{bmatrix} \quad (23)$$

$$D = \begin{bmatrix} D_{xx} & D_{xy} & D_{xz} & D_{yy} & D_{yz} & D_{zz} \end{bmatrix}^T \quad (24)$$

$$X = BD' \quad (25)$$

If the relation between the measurements in the acquisition and the diffusion tensor is known, it is possible to extract the tensor components [26, 40]. There only has to exist a $\hat{d}$ as an inversion of the equation above and obtained with an error of e':

$$D' = \hat{d}.X + e' \quad (26)$$

$$\hat{d} = (B^T B)^{-1} B^T \quad (27)$$

The tensor obtains the final form as shown in equation 19 and characterizes the diffusio within a considered voxel. Despite the importance of the information within the diffusion tensor, it is rather difficult to illustrate the tensor characteristics of all voxels within a certain region or volume of interest (ROI and VOI respectively) as "an easy-to-read image" or information, because the tensor has nine different elements [40]. In order to achieve an easy-to-read diffusion parameter, rotationally invariant parameters were proposed, and among them we describe an isotropic and two anisotropic parameters.

The isotropic parameter is known as the Mean Diffusivity (MD) and it is calculated through the most useful measure of isotropy, obtained through DTI: the trace (Tr) of the

diffusion tensor (D), being the sum of the three diagonal elements. The MD will be the division of this sum by 3:

$$Tr(D) = D_{xx} + D_{yy} + D_{zz} = \lambda_1 + \lambda_2 + \lambda_3 \quad (28)$$

$$MD = \frac{Tr(D)}{3} \quad (29)$$

It is a diffusion parameter extensively used in clinical studies, being fairly uniform through parenchyma [41] and does not confound the anisotropy effects on the detection of diffusion abnormalities (figure 16A).

The most useful scalar measure of anisotropy is known as the fractional anisotropy (FA) [41], being a ratio between the mean square root and the standard deviations of the eigenvalues (figure 16B)

$$FA = \sqrt{\frac{1}{2}}\frac{\sqrt{(\lambda_1-\lambda_2)^2+(\lambda_2-\lambda_3)^2+(\lambda_3-\lambda_1)^2}}{\sqrt{\lambda_1^2+\lambda_2^2+\lambda_3^2}} \quad (30)$$

It is normalized to the interval [0:1]. A value of zero means that water molecules are transported in all directions being this, the case of a strong isotropic diffusion. Otherwise in the case of a strong anisotropic diffusion, the FA is approximately equal to 1, and the water molecules will be transported through one main direction, corresponding to the major eigenvector with the highest of the eigenvalues. Unlike MD, FA is a scalar parameter that presents a vast difference between GM and WM, due to the cell content of each of these structures (figure 24). In GM it presents values approximately to 0.2 and varying between 0.4 and 1 in WM [26]

Figure 24: Illustration of three diffusion ellipsoids, all with the same mean diffusivity value (MD=0.7x10^{-3} mm^2) and fractional anisotropy ranging from isotropic (lower FA=0.12) to anisotropic (higher FA=0.82)

Looking at the FA expression in equation 23, it should be possible to recognize the two main tensor shapes that result from high anisotropy: “cigar-shaped” ($\lambda_1 > \lambda_2 = \lambda_3$) and

"pancake-shaped" ($\lambda_1 = \lambda_2 > \lambda_3$) tensors. To this end, it is possible to calculate new diffusion anisotropic parameters through the eigenvalues, like: the axial FA, a more robust and sensitive anisotropic parameter than FA; and three parameters describing the ellipsoid's "linearity" (C_l), "planarity" (C_p) and "sphericity" (C_s), note that $C_l+C_p+C_s=1$ [26].

$$Axial\ FA = \frac{\lambda_1 - \left(\frac{1}{2}(\lambda_2+\lambda_3)\right)}{\lambda_1+\lambda_2+\lambda_1} \quad (31)$$

$$C_l = \frac{\lambda_1-\lambda_2}{\lambda_1+\lambda_2+\lambda_3} \quad (32)$$

$$C_p = \frac{2(\lambda_2-\lambda_3)}{\lambda_1+\lambda_2+\lambda_3} \quad (33)$$

$$C_s = \frac{3\lambda_3}{\lambda_1+\lambda_2+\lambda_3} \quad (34)$$

With these parameters, we can calculate a final parameter that provides the deviation of the ellipsoid's shape, describing the water molecule anisotropy, from a full spherical case, specific for a full isotropic water motion. This parameter is the ellipsoid's "anisotropy" [26]:

$$C_a = \frac{\lambda_1+\lambda_2-2\lambda_3}{\lambda_1+\lambda_2+\lambda_3} \quad (35)$$

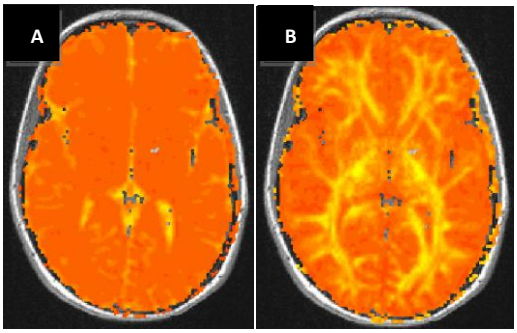

Figure 25: MD (A) and FA (B) data collection of a brain's slice in a transversal section. The image intensity is proportional to the diffusion and anisotropy degree (A and B respectively). In image B, there's a proper distinction between the GM with the lowest intensities and the WM, with the highest intensities.

4.2.4. Tensor Orientation

For brain structures widely oriented along the three principal reference axies (x, y and z), it is possible to infer fiber orientation along those orthogonal axes [41, 42, 43]. Using the eigenvectors and correspondent eigenvalues of the diffusion tensor information, it is possible to illustrate the orientation of fiber tracts using three primary colors. The most used schemes [41, 42] associates the x, y and z elements of the main eigenvectors with the primary colors red, green and blue respectively, as illustrated in figure. By following the path of transmission in color, it is possible to visualize the trajectory, along fiber orientation, of the WM fiber tracts [43, 44, 45].

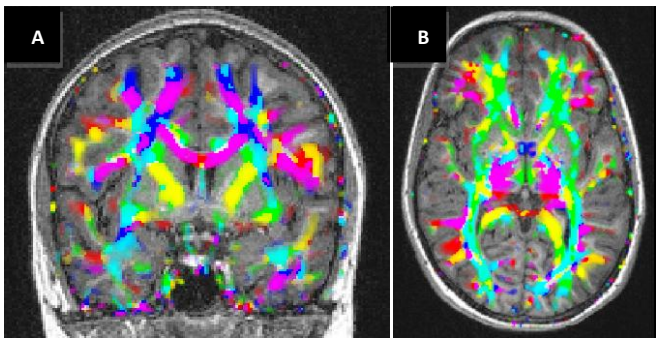

Figure 26: Example of the coronal and transversal section of a color-encoded fiber orientation maps, obtained with the BrainVoyager 2.3. QX software. A combination of colors creates tracts of different colors (A-B).

4.2.5. High angular resolution diffusion imaging (HARDI) methodologies

The principal limitation of the DTI methodology is the determination of water molecules motion orientation in cases where the fibers meet and cross, a process often called "fiber crossing" [26, 40]. This led to the development of new methodologies acquired using a lot more gradient directions than those used in LARDI. The two main "fiber crossing" diffusion MRI data acquisition methodologies are the High Angular Resolution Diffusion Imaging (HARDI) and the Diffusion Spectrum Imaging techniques, and in both these approaches the computation for each voxel has similarities to the DTI approach but the data processing is more mathematically elaborate, thus requiring a greater number of diffusion-sensitizing gradient directions for the case of HARDI, and a greater number of both directions and amplitudes in the cased of DSI (figure 27) [52]. In HARDI, the q-vector amplitude is maintained by keeping both δ and the gradient amplitude constant, and the MR signal reduction is obtained for multiple gradient directions. Nowadays the most common HARDI data-processing methodologies are the Multi-tensor DTI where we have several tensor estimations within a voxel, and Q-ball Imaging (QBI) where one obtains an orientation distribution function (ODF) of

water diffusion for each voxel. The DSI approach is the ultimate technique of diffusion MRI acquisition, the acquired diffusion MRI data is such that the q-vector arranged in a cubic grid, and the corresponding data processing obtains a displacement probability distribution function (PDF) of water diffusion for each voxel [51].

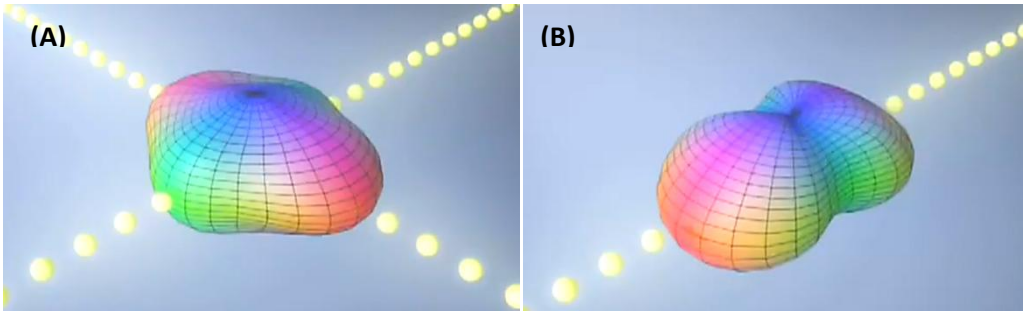

Figure 27: Illustration of a HARDI acquisition in a specific voxel; in (A) it is properly represented in a specific voxel two crossing tracts, while in (B) using DTI we have only one tract [55].

4.2.6. Fiber Tracking

4.2.6.1. Concepts

Nowadays, fiber tracking (FT) is a method widely used to identificate and measure WM pathways. It is a non-invasive and can be done both in-vivo and ex-vivo. It relies on one essential assumption: that the water molecule motion is restricted when it passes through the axonal membranes and that the axons are typically arranged in parallel bundle arrangements. So, when there's an injury in the WM, the water diffusion is most likely to be hindered across this axis than along it [26, 40].

In DTI or multi-DTI approaches, the FT bases on the eigenvectors and eigenvalues information and reconstructs the fiber tracts existing in the WM, connecting the different regions of the GM cortex.

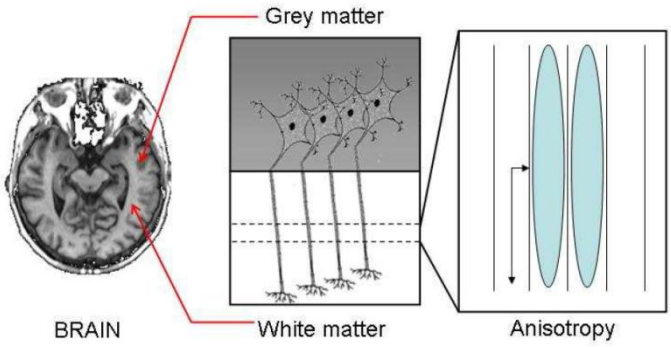

Figure 28: Illustration of the association of anisotropy with the CNS; First we have a separation of the brain's white and GM through imaging contrast, and we can verify the differences in both structures allowing, for the case of WM, a more anisotropic water diffusion in the presence of parallel axons [40].

4.2.6.2. Strategies (Deterministic and Probabilistic FT)

FT can be separated in two main approaches, depending on the stepping process chosen: deterministic or probabilistic fiber tracking. Each of them will be briefly described, and subsequently a more detailed explanation about the approach used with BrainVoyager 2.3. QX will be given.

Deterministic FT is based in the streamline approach. In this approach one defines a starting point and then, a constant step-size advancement is made following a direction parallel to the orientation of the diffusion tensor's eigenvector with the biggest eigenvalue, ε_1 in our nomenclature. A stopping criteria (typically the arrival to a low FA region) is reached and the reconstruction of the WM pathways is ended. The output of this approach is a WM pathway connecting two points in the brain [26, 40].

The probabilistic FT approach uses the diffusion MRI information as a background for the development of a Monte-Carlo algorithm. This Monte-Carlo algorithm associates to each point in space a ODF (and/or a displacement PDF) which is then used to calculate the probability of joining two points. Any two points have a finite probability of being connected, but some probabilities are much higher than others. At the end, the positions of the brain with a larger number of highly probable trajectories joining them will be considered to be very likely to be anatomically connected [26, 40].

The deterministic approach is the method used in the fiber tracking performed by BrainVoyager QX 2.3. and so it will be explained in more detail, and properly illustrated (figure

29). As it was mentioned before, the deterministic approach is a streamline approach which can be divided in the following way:

1. First, a starting point must be chosen. Usually the choice of this point comes from where one is expected to find a known fiber tracts starting in a known region of the cortex. Another and very useful approach is the selection of the starting point acquired with other MRI measurement, such as a functional MRI (fMRI) experiment;

2. After the choice of a starting point, comes the streamline reconstruction of the WM pathway. This reconstruction is performed in small steps, and considering X_n as being the current position of the fiber reconstruction step, X_{n+1} as the position of the next point, ε_n as the diffusion direction provided by diffusion MRI information and Δ_x as the step length, the reconstruction of the fiber tract can be described with the following general equation [40]:

$$X_{n+1} = X_n + \varepsilon_n . \Delta_x \quad (36)$$

3. Finally, a stopping criterion must be considered for reconstruction termination. The fiber tract reconstruction has no conditions to continue if the reconstruction enters brain positions inside GM, and because no fibers are expected to be reconstructed there (another example could be inside the cerebral spinal fluid (CSF)). These structures can be detected by its diffusion anisotropy properties and therefore, FA becomes a useful tool in its detection. Summarizing, once the FA value becomes lower than a certain threshold there is no need to continue the WM pathway reconstruction. Another stopping criterion is the angle threshold, used to stop the reconstruction when the angle of diffusion direction between two successive positions is too discrepant.

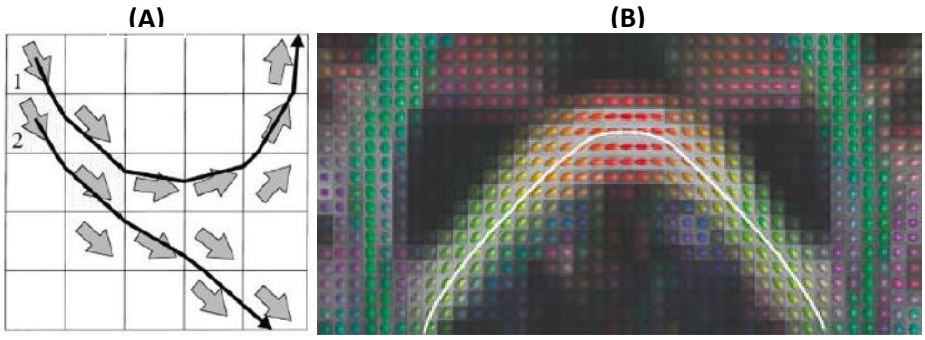

Figure 29: Examples of streamline tractography following the orientation of diffusion MRI data along the principal eigenvector with the highest eigenvalues; (A) is the illustration of the specific streamline tractography developed by BrainVoyager QX 2.3.software (B) shows the specific streamline tractography developed by Mori et al (1999), where the diffusion tensor main orientations are identified by its primary colors [26].

4.2.7. Principles of diffusion imaging in neural tissue

As described in the previous sub-sections, the basis of DTI and fiber tracking lies on the anisotropic diffusion of water molecules in neural fibers of WM. Water molecule diffusion provides essential information about structure and function of the brain, being sensitive to the considered tissue microstructure (cell's cytoskeleton, axonal membranes, and other macromolecules structures and fibers), and it varies according to the tissue in consideration and pathological modifications that may occur within it [26]. The importance and strength of the MRI lies in this fact, providing methods where its image contrast and acquisition sequence are sensitive to different water molecular properties [26].

In the diffusion MRI technique, we average water molecular motions within a voxel, since the molecular mean square displacement during T_E is on the order of microns, and the voxel size is on the scale of the millimeters. Nowadays, diffusion-weighted images are extensively applied in neuroimaging. This approach aims to highlight the differences occurring in water molecule movements, due to the random motion of water molecules in the studied neural tissues.

The displacement of water molecules in DTI can be described in three different situations [26] and for which one of them, diffusion MRI gives different image contrasts and thus makes a proper distinction between different tissues:

1. First, we have a free diffusion of water molecules (figure 28A), with no restrictions in water molecule displacement in all directions as for example, the case of the cerebrospinal fluid;

2. Second, we have a water molecule restricted isotropic diffusion in all directions (figure 28B), due to various obstacles (p.e. proteins, macromolecules) ;
3. Thirdly, water molecules can also be orientated through a restricted anisotropic diffusion in tissues, in one or several distinguished directions (figure 28C). In this case, water molecule diffusion in only restricted in a certain direction, as in the case of fibers;

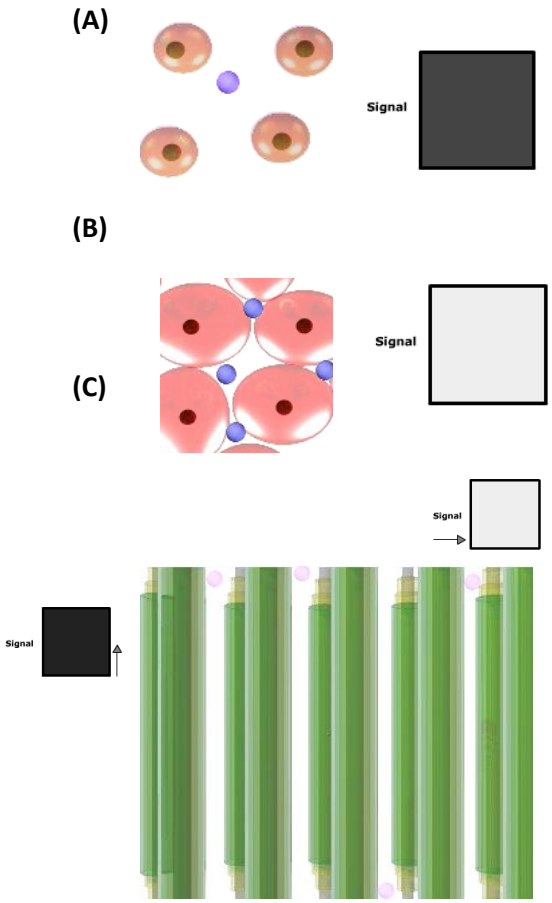

Figure 30: Illustration of the three existing types of water molecule diffusion considered in DTI (A, B and C), leading to different MR signal attenuations and correspondent contrasts in the diffusion-weighted image acquisition [54].

Anisotropic diffusion is more correlated to figure 30C, where the water molecule displacements are not the same for different directions. Indeed in anisotropic diffusion, water molecules "prefer" to move parallel and to the axon's length, rather than moving between axons across their membrane. Being the axon, one of the main components of a WM fiber tract, DTI and fiber tracking methodologies make it possible to perform the "virtual identification" of those fibers in the human brain [26]

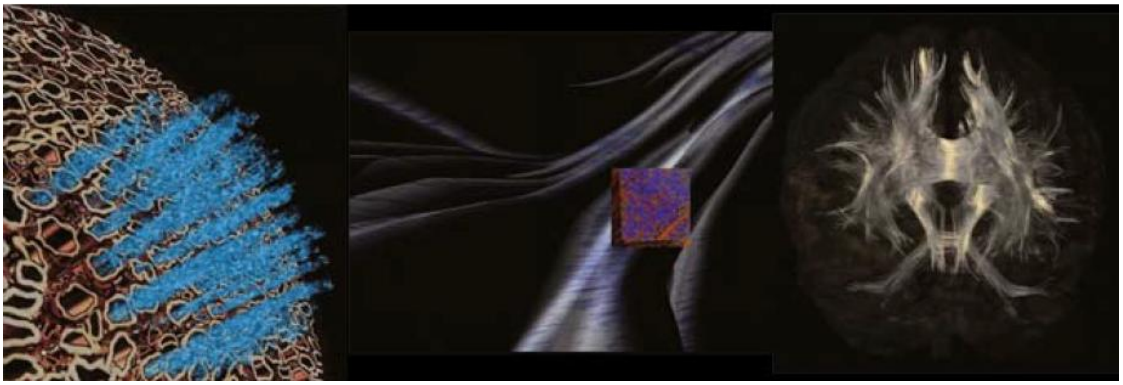

Figure 31: Schematic illustration of anistropic water diffusion measurement form axons to tracts, using DTI methodologies over resolution of several millimeters in voxels, extracting the WM tracts in the brain [26].

4.2.8. The Human Connectome

FT is also an important tool in some very interesting studies, like those studying the full connectivity structure of the human brain, usually called "the human connectome"[46, 47]. With the creation of a full detailed network delimitation of the structural connection of the human brain, we are one step closer to the full understanding of the functionality of the human brain as a complex system [26].

Just like functional and structural methodologies of MRI, diffusion imaging and FT are extremely important for this goal in enabling, the in vivo estimation of structural connectivities at a specific scale [26].

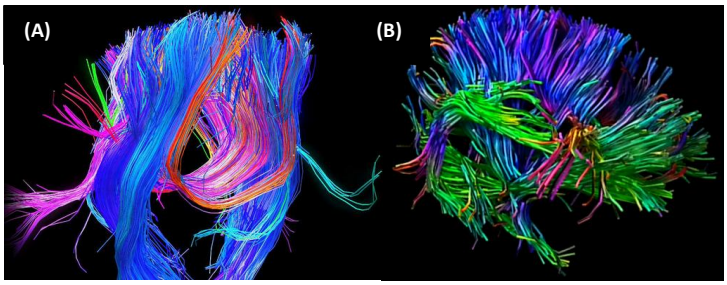

Figure 32: Illustration of two types of fiber tracking approaches developed by the Human Connectome Research group; (A) illustrates the full fiber connectivity through the medial section of the corpus callosum, while in (B) we have the full fiber connectivity estimation of the human brain.

Methods

Chapter 5: MR acquisition protocol

5.1. Participants

In this study, we analyzed deficits in visual-callosal WM pathways in a total of seventy-six recruited individuals. The analysis was performed in two groups: NF1 patients and healthy volunteers (Table 2).

Table 12: Demographic table: participants characterization by gender and age (age = mean age ± SD)

		CHILDREN			ADULTS		
		Boys (♂) (age range)	**Girls (♀) (age range)**	**Total**	**Boys (♂) (age range)**	**Girls (♀) (age range)**	**Total**
Controls	**N**	9 (7-17)	14 (7-17)	23	2 (32-34)	18 (19-39)	20
	Age ± SD	12,0 ± 2,73	12,0 ± 3,0	12,0 ± 2,85	33,0 ± 1,41	33,0 ± 5,6	32,0 ± 6,0
NF1	**N**	6 (7-16)	14 (9-16)	20	-	13 (23-42)	13
	Age ± SD	11,8 ± 3,3	11,07 ± 2,2	11,0 ± 2,52	-	33,0 ± 4,94	33,0 ± 4,94
Total	**N**	15	28	43	2	31	33
	Age ± SD	12,0 ± 2,86	11,0 ± 2,3	12,0 ± 2,48	33,0 ± 1,41	11,0 ± 2,2	33,0 ± 5,59

NF1 participants were recruited and diagnosed in collaboration with the Genetics Department of the Pediatrics Hospital of Coimbra according to the NIH criteria (1988) [57]. For the children/adolescent control group, participants were recruited among unaffected siblings and from a local school. The adult control group was recruited among the unaffected mothers or from an adult educational school. These adult schools provide learning programs for adults with low educational levels and many NF1 adult participants are also attendants.

The study was conducted in accordance with the Declaration of Helsinki and all procedures were reviewed and approved by the Ethics Commissions of the Faculty of Medicine of the University of Coimbra and of the Hospitals of Coimbra. Informed consent was obtained from the children's parents and the adult volunteers.

In order to ensure that participants included in the study had no central nervous system pathology, a FLAIR MRI sequence was performed in addition to the standard structural scans. Neuroradiological assessments were carried out by an experienced neuroradiologist.

Participants were excluded from this study if they had a clinically significant intracranial abnormality on MRI such as intracranial tumor, optic glioma or other imaging

abnormalities. The presence of UBOs (Unidentified Bright Objects - T2 hyperintensities, commonly found in NF1 patients) was not considered to be an exclusion criteria.

None of the participants had a psychiatric illness, epilepsy or were taking medication for treating depression. Participants were also excluded if they had full-scale IQ below 70, for the children/adolescent groups, or Raven Matrices score below 3 (n= 1 NF1), in the adult groups. Parents of children on stimulant medication for attention deficit hyperactivity disorder (ADHD) were requested not to give their children the medication on the days of testing. All the participants had normal or corrected-to-normal visual acuity.

Ophthalmological assessment was performed by an experienced ophthalmologist to rule out eye disorders in the NF1 group. This included best-corrected visual acuity, stereopsis evaluation using Randot, slit lamp examination of anterior chamber structures and fundus examination. No anomalies that could affect vision were found.

5.2. Data acquisition

Scanning was performed on a 3T Siemens TimTrio scanner at the Portuguese Brain Imaging Network (BIN), using a 12-channel birdcage head coil. For each participant we acquired: i) two T1-weighted (T1w) MPRAGE sequences, 1x1x1 mm^3 voxel size, repetition time (TR) 2.3 s, echo time (TE) 2.98 ms, flip angle (FA) 9°, field of view (FOV) 256x256, 160 slices; ii) a T2-weighted (T2w) FLAIR sequence, 1x1x1 mm^3 voxel size, TR 5 s, TE 2.98 ms, Inversion Time (TI) 1.8 s, FOV 250x250, 160 slices; iii) one run of fMRI scanning for the M/P-biased stimuli and two runs of the polar angle stimuli using single shot echo planar imaging (EPI) acquired in the axial plane orthogonal to the anterior commissure covering the occipital, temporal and frontal cortices, with 2x2x2 mm^3 voxel size, TR 2 s, TE 39 ms with a 128x128 matrix, FA 90º, FOV 256x256, 26 slices; iv) a DTI scan using a spin-echo planar imaging sequence with 20 non-identical gradient directions (b-value=1000), with 1.8x1.8x3 mm^3, TR 5.1s, TE 104 ms, 35 slices and 3 repetitions, totaling 63 volumes.

FLAIR images were used to identify T2 hyperintensities, a common neuroradiological finding in NF1 patients. A neuroradiologist blinded to the participants' clinical history observed the MR structural scans and reported on the distribution and number of UBOs. Fourteen of the twenty (70 %) children and 9 of the thirteen (69.2%%) adults with NF1 had one or more UBOs. The frequency of UBOs is in accordance with published data (Payne *et al.* , 2010). None of the control participants had UBOs.

5.3. Data Analysis

5.3.1. Demographic analysis

Statistical analyses concerning demographic data were performed with IBM SPSS Statistics 19 (SPSS Inc., Chicago, USA).

First, we verified the normality assumption for the different parameters using the Shapiro Wilk's test. For normally distributed data, we used independent samples t-tests, ANOVA and Pearson's correlation analyses. When the data did not meet assumptions of sphericity, we used the epsilon value to choose the type of correction applied: the Huynh-Feldt (for $\varepsilon > 0.75$) or the Greenhouse–Geiser (for $\varepsilon < 0.75$). For the non-normal data, we used the Mann-Whitney test for comparison between two independent samples. *P* values <0.05 were considered statistically significant.

5.3.2. Magnetic Resonance Image processing and analysis

Image processing and analysis were carried out using BrainVoyager QX 2.1 (Brain Innovation, Maastricht, The Netherlands) and PAWS Statistics 18 (SPSS Inc., Chicago, USA).

5.3.3. Image processing and analysis in retinotopically-defined areas

The image analysis described in this sub-section comes from a related project where the retinotopic maps were defined in the same individuals.

5.3.3.1. <u>Anatomical Image processing</u> - High-resolution T1w anatomical images were intensity normalized and re-oriented into a space where the anterior and the posterior commissure lie in the same plane (AC-PC). Afterwards, cortex was segmented using automatic segmentation routines (Kriegeskorte and Goebel, 2001), mesh representations of each hemisphere were created and inflated for polar angle maps projection.

5.3.3.2. <u>Functional Image Processing</u> - Functional data pre-processing prior to statistical analysis consisted of slice scan time correction, linear trend removal, temporal high-pass filtering (2 cycles per run), followed by a correction for small interscan head movements. Participants were excluded from further analysis if any within-run movement exceeding 2 mm was detected (n= 2 NF1, 4 controls).

In addition, we applied modest spatial smoothing using a Gaussian filter (FWHM 2 mm).

5.3.3.3. Retinotopic mapping - Polar angle maps were obtained from the average of two runs, created based on linear regression analysis and projected onto the AC-PC anatomical surfaces of each subject. The cross-correlation was calculated for each run, as a function of the time lag (in TR units, 2 seconds per lag). Lag values at each voxel were encoded in pseudocolors, voxels were included into the statistical map if r >0.25, p <0.05. Retinotopic areas V1, V2 dorsal (d), V2 ventral (v), V3d and V3v were manually defined for each subject in each hemisphere in the inflated meshes. Obtained regions-of-interest (ROIs) were used as "masks" to the analysis of the blood-oxygen-level-dependent (BOLD) signal elicited by M- and P-biased stimuli.

5.3.4. DW-MRI Analysis

All the analysis referent to this sub-section is properly illustrated and explained in more detail in chapter 6.

DTI data was primarily averaged into 21 volumes, with the creation of a diffusion weighted magnetic resonance (DMR) project. The DMR project was subsequently co-registered with the T1w MRI structural data. The resulting transformation calculations were employed to the creation of a 3D Diffusion Weighted data set (VDW). We extracted for each voxel the eigenvalues (λ1, λ2 and λ3) in a volume map (VMP) file format. With the eigenvalues we were able to calculate the mean diffusivity (MD), fractional anisotropy (FA) giving respectively, the average of diffusion and the anisotropy of diffusion within a voxel. Axial FA values were also calculated.

5.3.5. Fiber Tracking Analysis

All the analysis referent to this sub-section is properly illustrated and explained in more detail in chapter 7.

Our procedure was adapted from a previous study [33]. We started by drawing two volumes of interest: one surrounding the splenium of the corpus callosum, taking into account anatomical landmarks [29], and the second in a slice of the occipital lobe's WM occupying both brain hemispheres. We performed a first fiber tracking approach with seed points in the occipital lobe VOI and intersection on the splenium. The subset of fibers identified is then transferred to Matlab. In-house software was designed to identify the voxels of those fibers belonging to a particular visual area. In summary, voxels within a range of 3mm to each visual

region were identified as belonging to this region and will be used as seed points for a new fiber tracking approach. An intersection point is again considered in the VOI surrounding the splenium and as a result the occipital-callosal fiber tracts are identified according to each seed VOI.

With the VMP files extracted with the DW-MRI analysis in BrainVoyager, we can extract the diffusion parameters and eigensystem values specifically for the voxels belonging to the visual-callosal WM pathways identified with our FT approach and calculate the values for each fiber tract amount identified according to its seed VOI in the visual cortex.

With the statistical analysis, we aimed to determine if there was any significant difference on the diffusion parameters and eigensystem values for the visual-callosal WM pathways, between healthy volunteers and NF1. Consequently, we performed the ANOVA General Linear Model (GLM) repeated measures analysis. First we analyzed the within-subject effects, i.e. to determine if there was any significant difference on the measures extracted of the identified fiber tracts for the two groups. If the significance level of the Mauchly's test was lower than 0.05 (i.e. $p<0.05$), the data did not meet the assumptions of sphericity. So we used the Greenhouse–Geiser correction (for $\varepsilon < 0.75$). After this, the between-subject effect was analyzed in order to detect if there was any differences between the two groups.

Regarding the specific differences for each group in each visual-callosal WM pathways identified for each individual, we performed the Independent-Samples T-Test. For the equality of variances within groups, if the significance level of the Levene's test was lower than 0.05 (i.e. $p<0.05$) this meant that their variances were not similar, and so the "equal variances not assumed" test was used. Otherwise, we used the "equal variances assumed" test. After this the "t-test for equality of means" was used to detect if there was any differences between the two groups for each visual-callosal WM pathway.

The within group age dependence of the diffusion parameters and eigensystem values was tested separately for each fiber identification using a parametric bivariate correlation analysis (Pearson).

Chapter 6: Single subject Diffusion Weighted (DW) – MRI analysis

All image processing and statistical analysis were carried out using BrainVoyager QX 2.3 (Brain Innovation, Maastricht, The Netherlands) and IBM SPSS Statistics 19 (SPSS Inc., Chicago, USA). This chapter aims to be a step-by-step guide for a DW-MRI data set analysis in BrainVoyager 2.3 QX.

6.1. Initial data

For the DW-MRI analysis procedure we require some initial information, like: DW-MR images, information about the gradient used during the acquisition, an anatomical data set acquired in the same session as the diffusion data set, as well as anatomical information about the low-level visual areas defined with fMRI. Table 1 summarizes this data, specifying each information type:

Table 13: Initial data required for a DW-MRI analysis in BrainVoyager 2.3 QX

Data	File type
DW-MR Images	DICOM
Gradient information	GRB
Anatomical project	VMR
Low-level visual areas	VOI

6.1.1. Gradient information

The gradient file is a table composed by 63 rows and 4 columns, containing the gradient direction (x,y and z) and respective b-value for each volume.

6.1.2. Anatomical project (VMR)

The anatomical project is a 3D high resolution data set of the subject's brain, also created in BrainVoyager QX, with 163 slices corresponding to each volume acquired during the section and with the dimension 768x768 (figure 33).

The anatomical project is re-oriented to a space where the anterior and posterior commisures (figure 34A) lie in the same plane (figure 34B), called the AC-PC space. This space allows an accurate localization of functional signals, providing an easier inter-subject comparison. The transformation is performed with a "sinc" interpolation. A transformation file (.trf) will be saved, specifying the spatial transformation performed in this procedure and a final VMR will be obtained as the result of the application of the saved spatial transformation.

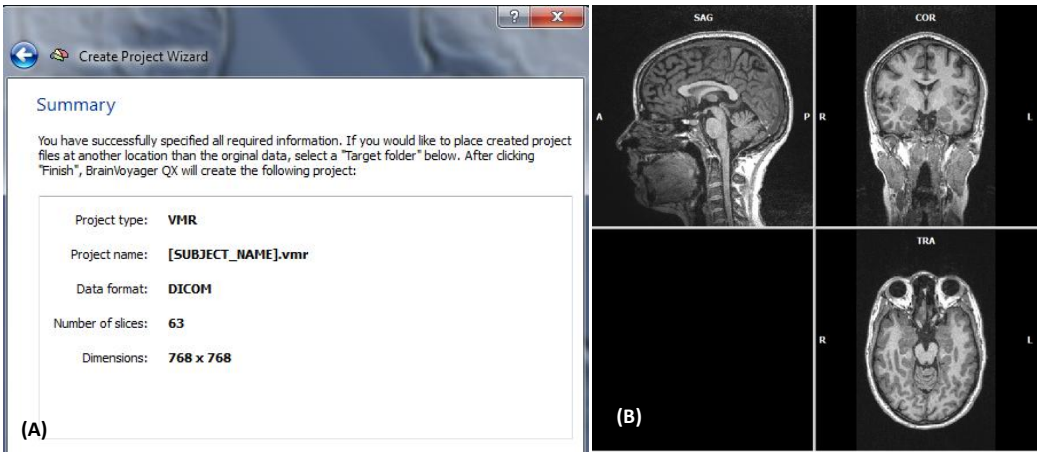

Figure 33: (A) VMR final "Project Creation" dialog, with all the specific information required for its creation; (B) Schematic illustration of the VMR as a 3D anatomical data set, with proper visualization of the brain on sagital, coronal and transversal views.

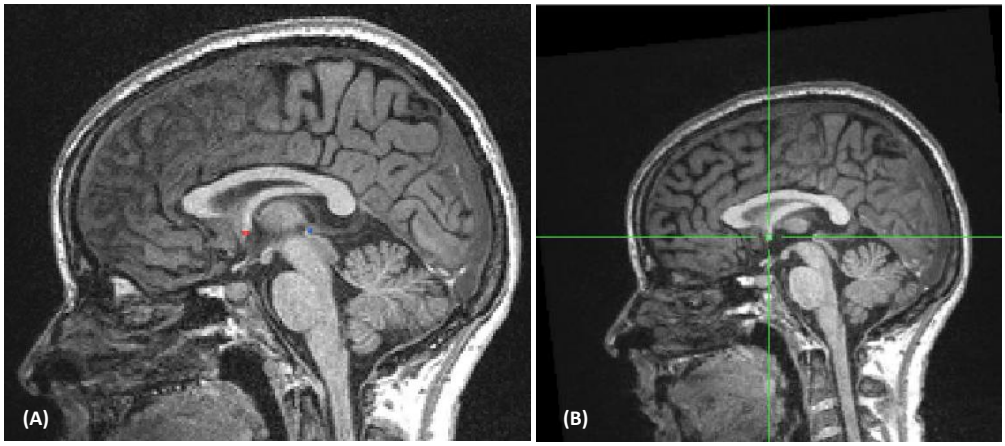

Figure 34: (A) Schematic illustration of a sagital brain view. The anterior commisure is represented in red, while the posterior commisure is in blue; (B) Same sagital brain view as in A, with a different zooming where the AC-PC plane is identified by the horizontal green line

6.1.3. Low-level visual cortical areas

This file has a volume of interest (VOI) format, composed by 10 different volumes. Each volume contains the voxels of the VMR project in the ACPC space corresponding to each visual area (V1, dorsal V2, ventral V2, dorsal V3 and ventral V3) for both brain hemispheres.

6.2. Creation of a Diffusion weighted Magnetic Resonance (DMR) project

The DMR project will be the basis of all DTI analysis inBrainVoyager QX. It will contain all the DW-MR images required during the MR acquisition (figure 35), with 35 slices totaling 63 volumes and a dimension 128x128. The gradient has 20 non identical directions (b-value=1000).

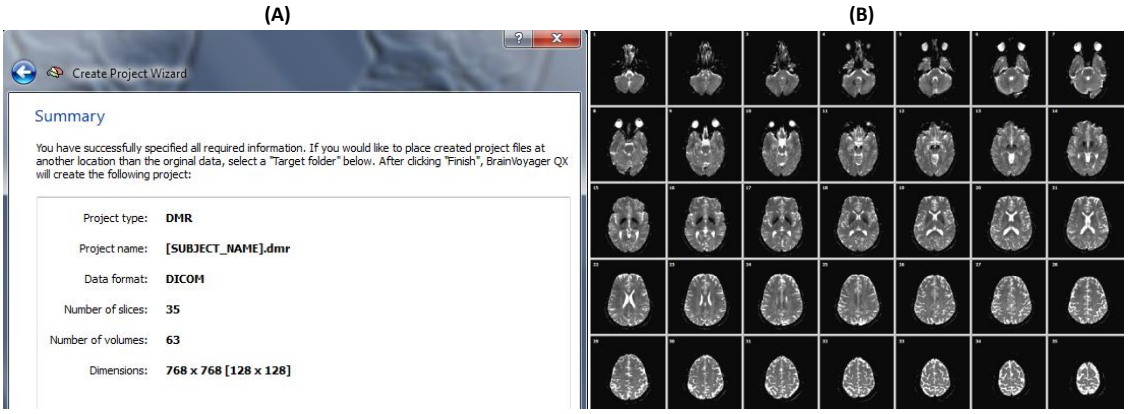

Figure 35: (A) DMR final "Project Creation" dialog, with all the specific information required for its creation; (B) Schematic illustration of the DMR as a diffusion weighted file, illustrating the brain in 35 slices.

6.3. Co-registration of the diffusion and anatomical data

Both DMR and VMR acquired in the same session need to be coregistrated, aligning the diffusion slice-based data on the DMR with the 3D anatomical data set (figure 36). This process will allow an association between the water molecule diffusion to anatomical locations in the brain, preparing the data for posterior analysis. This process will save two files with the transformations performed during the initial alignment (IA.trf file) and Fine-tunning alignment (FA.trf file), required for the next step of diffusion weighted imaging (DWI) analysis.

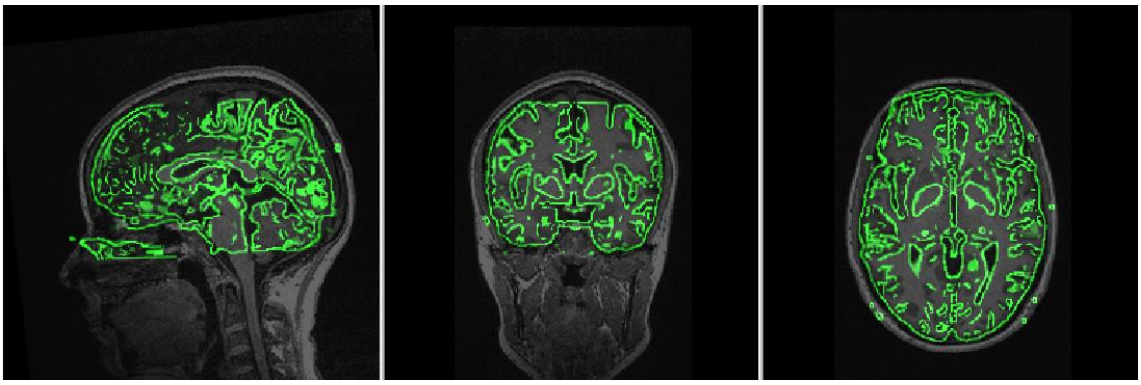

Figure 36: Schematic illustration sagital, coronal and transversal views of the co-registration of the DWI data of the DMR project (in green) to the 3D anatomical data of the VMR project.

6.4. Creation of a Volume Diffusion Weighted (VDW) data set

In this step, we transform our diffusion data into the AC-PC space, resulting in a VDW file creation, containing the 3D DW data set of the DMR project. For this process we require

both the DMR and the transformation file (.trf) created and saved during the co-registration of the DMR and VMR projects. The trf file saved during the transformation of the VMR into the ACPC space is required, because it has the spatial transformation information required for a similar transformation of the diffusion data.

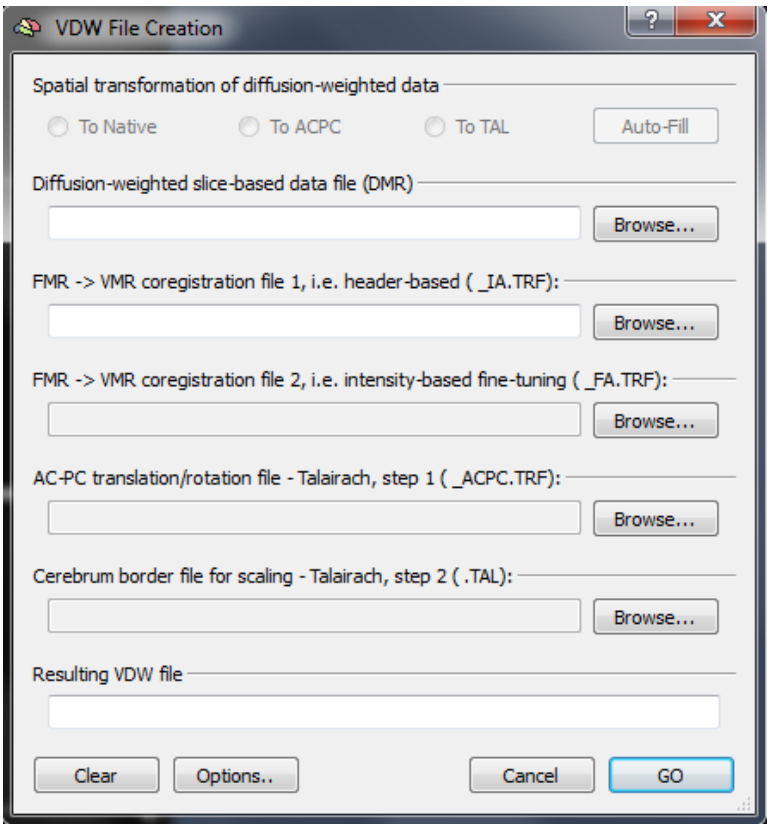

Figure 37: "VDW File Creation" window in BrainVoyager 2.3 QX;

6.5. Masking the DW data

Since the field of view is larger than the brain size, there is some noise present outside the brain in the VMR project. So, we will reduce that noise with the appliance of a mask involving only brain voxels. This approach, not only reduces significantly the number of voxels in the data, but also decreases the processing time in posterior steps.

The VMR project is composed of voxels with different intensities, ranging from 0 to 255, where only the voxels belonging to the brain will have intensities superior to zero (figure 36B). So, linking the VDW file created previously, which will define the bounding box of the mask, a proper segmentation of the brain is performed, the resulted voxels are colored (figure 36C) and the mask involving the individual's brain is created.

Figure 38: Schematic illustration of the sagital view of the brain before (A) and after (B) the segmentation; (C) After the segmentation the resulted voxels are colored and the mask is created using those colored voxels

6.6. Creation of a Diagonalized Diffusion Tensor (DDT) file

With the two previous steps we get the required data for the creation of a DDT file containing the diffusion tensor (with the eigenvector entries and the 3 eigenvalues) for each voxel of the VMR data: the VDW file, containing all the 3D DW data and a mask containing only the voxels within the brain, working mostly like a filter for a proper restriction of the diffusion tensor calculations to the human brain.

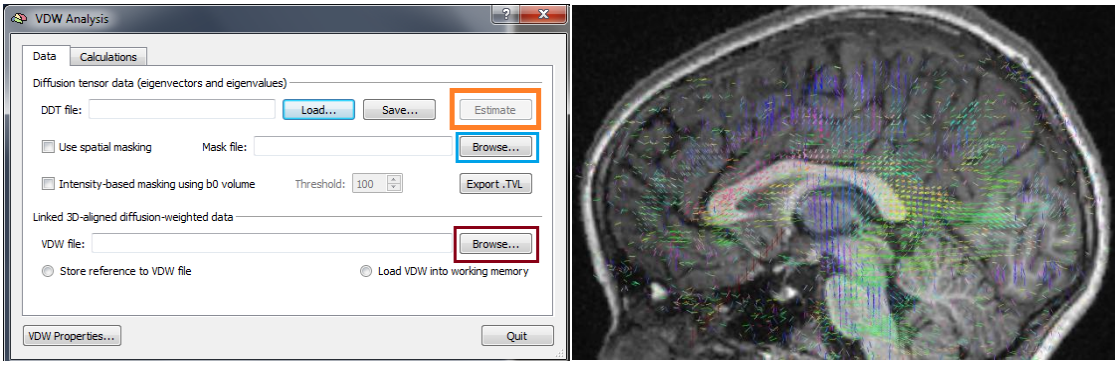

Figure 39: (A) Schematic illustration of the "VDW Analysis" window in BrainVoyager 2.3. QX, where the creation of the DDT file is performed; in the boxes blue and red correspond respectively to the inputs of the mask and VDW file required. The box in orange will estimate the diffusion tensor for each voxel of the input data; (B) Schematic illustration in a part of the VMR data of the diffusion tensors for each voxel, estimated with the creation of the DDT file.

6.7. Eigenvalues, Mean Diffusivity (MD), Fractional Anisotropy (FA) and Axial Fractional Anisotropy (Axial FA) computation

The computation of diffusion scalar parameters with the VMR-VDW attached project is stored in a volume map (VMP) format. The VMP will contain the values of the diffusion parameter being considered in each voxel of the anatomical data. Scalar parameters are calculated with the information estimated upon the creation of the DDT file, so we will have diffusion parameter calculations only in voxels within the applied brain mask.

The computation and extraction of mean diffusivity and fractional anisotropy in BrainVoyager is performed directly from the "VDW Analysis" window (figure 38).

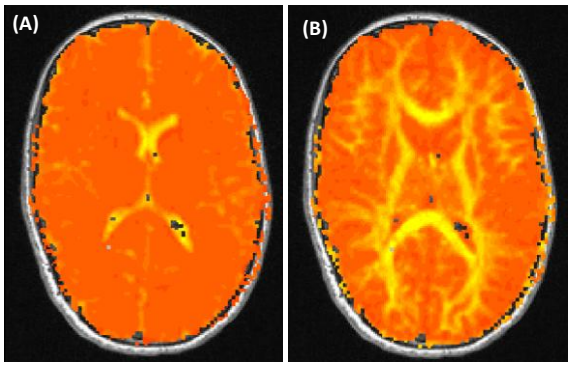

Figure 40: Schematic Illustration of a VMP of the same brain slice associated to an intensity histogram, where the color varies with the specific diffusion parameter value; In (A) we have the MD VMP, while in (B) we have the illustration of a FA computation. The VMP values ranges between 0 and 1, for both MD and FA; yellow color corresponds to the voxels with the highest scalar values for FA, while orange corresponds to the lowest ones

However, the extraction of the eigenvalues of the diffusion tensor is more complex. The DDT file must be transferred to Matlab, and with in-house software and the BVQXtools, we create new VMP files, containing the information of each eigenvalues in each voxel. This new VMP file is transferred again to BrainVoyager and the extraction of the VMPs of each eigenvalues is performed equally to what is done for the MD and FA extraction (figure 39).

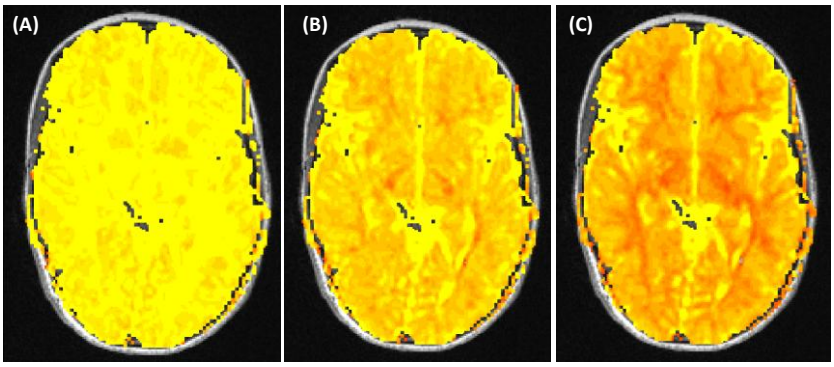

Figure 41: Schematic Illustration of a VMP of the same brain slice, illustrating an intensity histogram of eigenvalues λ_1, λ_2 and λ_3 in images (A), (B) and (C) respectively; yellow color corresponds to the voxels with the highest eigenvalue scalar values, while orange corresponds to the lowest ones

With the extraction of the eigenvalues, it is possible to compute the axial fractional anisotropy, given by the following equation [24]:

$$Axial\ FA = \frac{\left(\lambda_1 - \frac{1}{2}.(\lambda_2+\lambda_3)\right)}{(\lambda_1+\lambda_2+\lambda_3)} \quad (37)$$

Chapter 7: Single subject 3D Fiber Tracking

With the DTI analysis described in the previous chapter we have the diffusion tensor estimation for each voxel of the 3D anatomical data and so, using the fiber tracking methodologies explained in chapter 4, it is possible to estimate the path of the fiber tracts of the WM, with some additional information.

Fiber tracts were estimated using BrainVoyager 2.3. QX in the ACPC space, which uses a deterministic streamline tracking algorithm and a half-voxel step size. Each tensor is estimated using a trilinear interpolation of the tensor components. Starting in the initial seed, there's fiber tract estimation in one or both directions of the fiber main axis, depending on the tracking performance. The fiber path tracking proceeded until the FA value decreased below 0.20 or until the angle between the current path step and the estimation of the path step succeeding it exceeds 50°.

7.1. Occipital fiber tract estimation

Our fiber tracking procedure was adapted from a previous study [33]. We started by drawing one volume of interest (VOI) in the occipital lobe's WM occupying both brain hemispheres (figure 42).

In the VMR project, the voxels belonging to WM are those with FA having the higher intensities. Analyzing these intensities, a minimal value is chosen (figure 41A; blue box), from which all voxels with higher intensities will be colored (figure 41A; red color). This coloration will be restricted to the most posterior portion of the brain, with the right limitation of its main axis (figure 41A; orange box). The volume of interest containing the occipital lobe's WM will be created from the colored voxels (figure 41; green box and figure 41B; green box).

Each colored voxel belonging to the VOI will serve as seed point for a streamline fiber tracking approach, which will result in the estimation of all fiber tracts passing through the brain's occipital lobe WM (figure 43). Between them we estimate fiber tracts passing through the splenium of the corpus callosum and connecting the occipital lobe in both brain hemispheres. Other fibers are estimated, like those projecting to frontal and temporal lobes of the brain.

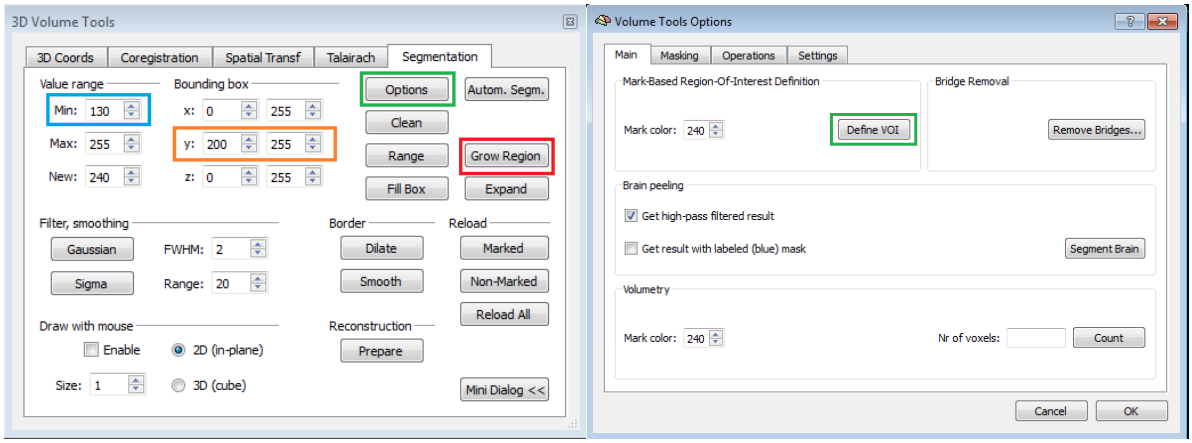

Figure 42: Schematic illustration of the "Volume Tools" windows used in BrainVoyager QX for a proper drawn of the occipital lobe´s WM volume of interest (VOI)

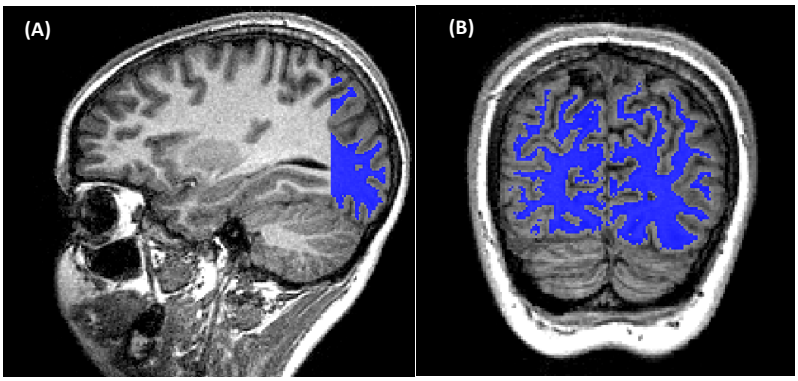

Figure 43: Sagital (A) and transversal (B) schematic illustrations of a volume of interest (VOI) defined in BrainVoyager for our fiber tracking procedure, in the occipital lobe's WM occupying both brain hemispheres

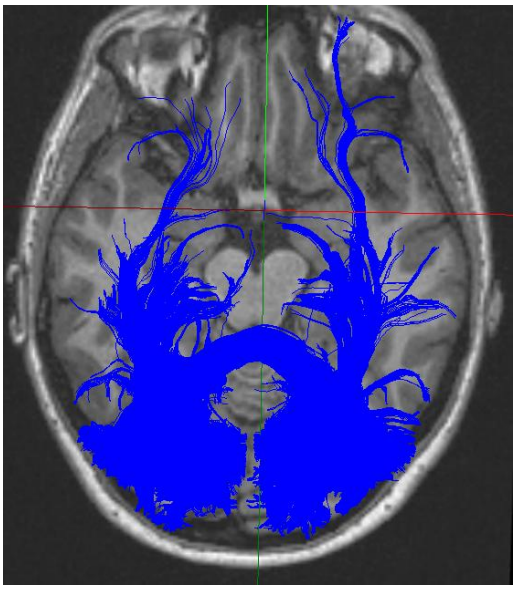

Figure 44: Schematic illustration of all fiber tracts that pass through the occipital lobe

7.2. Occipital-Callosal fiber tract sub-set estimation

A second VOI is drawn manually using a virtual drawing pen in 3D with dimensions 2x2x2 voxels, surrounding the splenium of the corpus callosum, taking in account anatomical landmarks [29]. We decided to extend the drawn of this VOI expanding it into other portions of the corpus callosum and even to voxels outside its anatomical structure (figure 44A). This was done, because we wanted to be sure to "catch" all the structure of the splenium of the corpus callosum, and taking in consideration that the corpus callosum is a structure surrounded by GM, no fibers will be tracked passing outside it. Also, we do not expect any connection between the retinotopic regions and other areas of the corpus callosum which do not include the splenium.

With the definition of a second VOI surrounding the splenium of the corpus callosum we can perform a fiber tracking approach, selecting from the estimated fiber tracts with seed points in the occipital lobe, those which intersect the VOI surrounding the splenium, in a "from

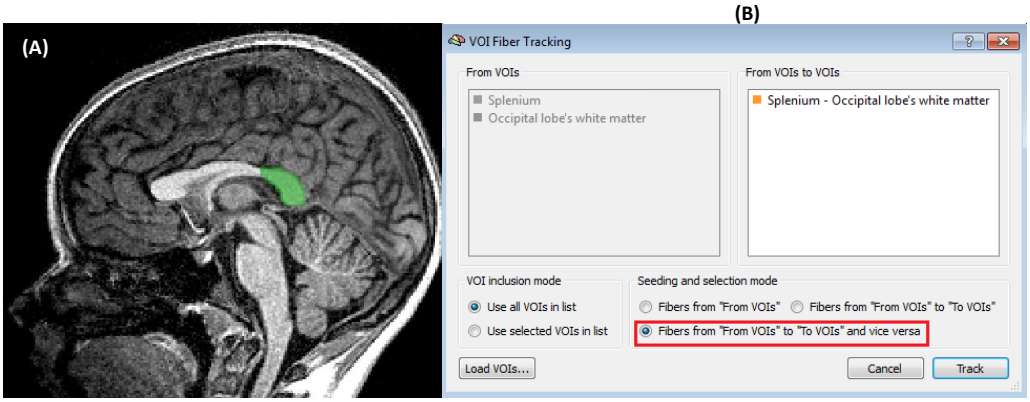

Figure 45: (A) Schematic illustration of a VOI drawn surrounding the splenium of the corpus callosum; (B) "VOI Fiber Tracking" window in BrainVoyager QX, where the seed and intersection points are selected.

VOIs to VOIs and vice versa" approach, allowing the tracking in the 2 directions. This will result in a sub-set of occipital-callosal fiber tracts (figure 45).

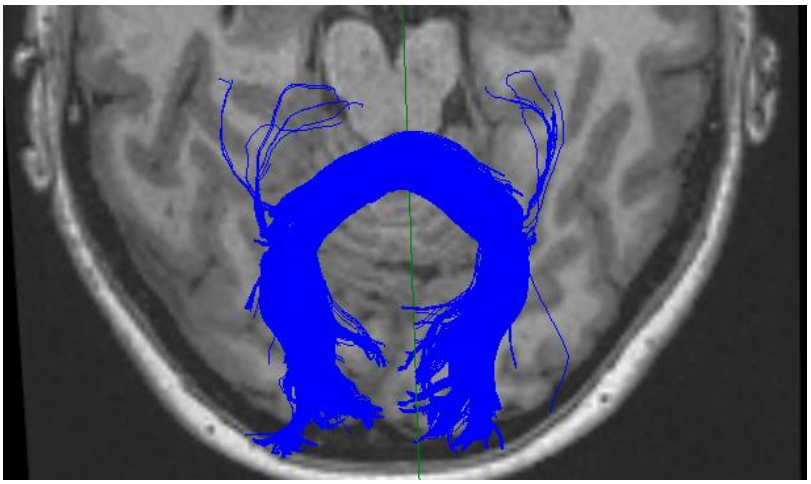

Figure 46: Sub-set of fiber tracts starting in the occipital lobe's WM and passing through the splenium of the corpus callosum

7.3. Fiber tract endpoints identification in Matlab

The voxels of the subset of fibers identified (figure 45) and the ones of each visual area defined with fMRI are transferred to Matlab. In-house software was designed to identify the voxels of those fibers belonging to a particularly visual area. In summary, voxels within a range of 3mm to each visual region were identified as belonging to this region and are used as seed points for a new fiber tracking approach.

7.4. Visual-Callosal fiber tract estimation

With the previous procedure, a new VOI file was created containing the voxels of the sub-set of occipital-callosal fiber tracts within 3mm of the cortical regions. This VOI file is again transferred into BrainVoyager QX. On this new fiber tracking approach we select those voxels as seed points and an intersection point is again considered in the VOI surrounding the splenium. As a result we get the visual-callosal fiber tracts properly identified according to each seed region in the visual cortex (figure 46).

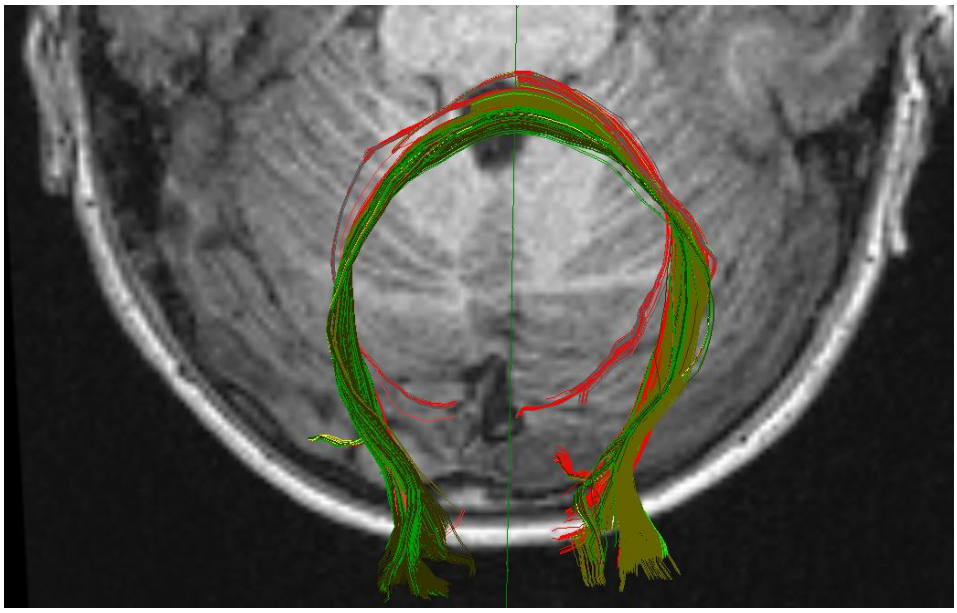

Figure 47: Schematic illustration of the new fiber tracking approach, resulting in visual-callosal fiber tracts identification according to each seed region in the visual cortex. With full identification, we get 10 types of fibers, since we have 10 regions of the visual cortex (V1, Dorsal V2, Ventral V2, Dorsal V3 and Ventral V3 for both right and left brain hemispheres)

With this fiber identification approach, having fiber tract estimations with seed points in the same visual region, from one brain hemisphere to the other and vice-versa, we have the possibility that some fiber tracts are being estimated twice, i.e. we are abserving the same pathway that goes from one hemisphere to the other.

Considering this fact, it was decided to identify the visual-callosal fiber tracts merely with their seed visual region, i.e. in the case of having the estimation of fibers starting in a specific visual area in one brain hemisphere, as well as another fiber amount starting in the same visual region in the other hemisphere, it was decided to join those two volumes of interest, containing those two fiber amounts in one volume of interest.

If it occurs that there is only fiber tract estimation with seed points in a particularly visual region in one hemisphere, but none in the other, then the estimated fiber tracts are kept and no distinction is made about the hemisphere from which fibers start (figure 47).

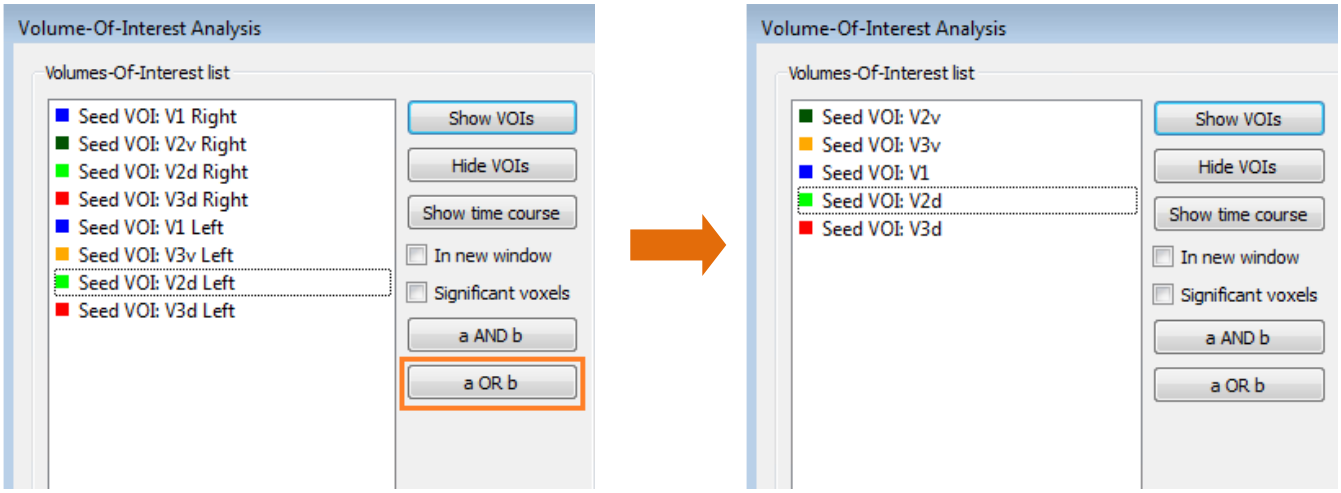

Figure 48: Schematic illustration of the reunion of two volumes of interest, representing two visual-callosal WM pathways with seed points in similar visual regions in the two brain hemispheres; If there is an estimation of a fiber tract amount with seed points in only in a particularly visual region in one hemisphere, the estimated fiber tracts are kept (figure example: fiber tracts with seed points in ventral V2 in the right hemisphere and ventral V3 in the left hemisphere

This procedure will result in the identification of five types of fibers, according to their respective seed points in visual regions: V1, dorsal V2, ventral V2, dorsal V3 and ventral V3 (figure 48).

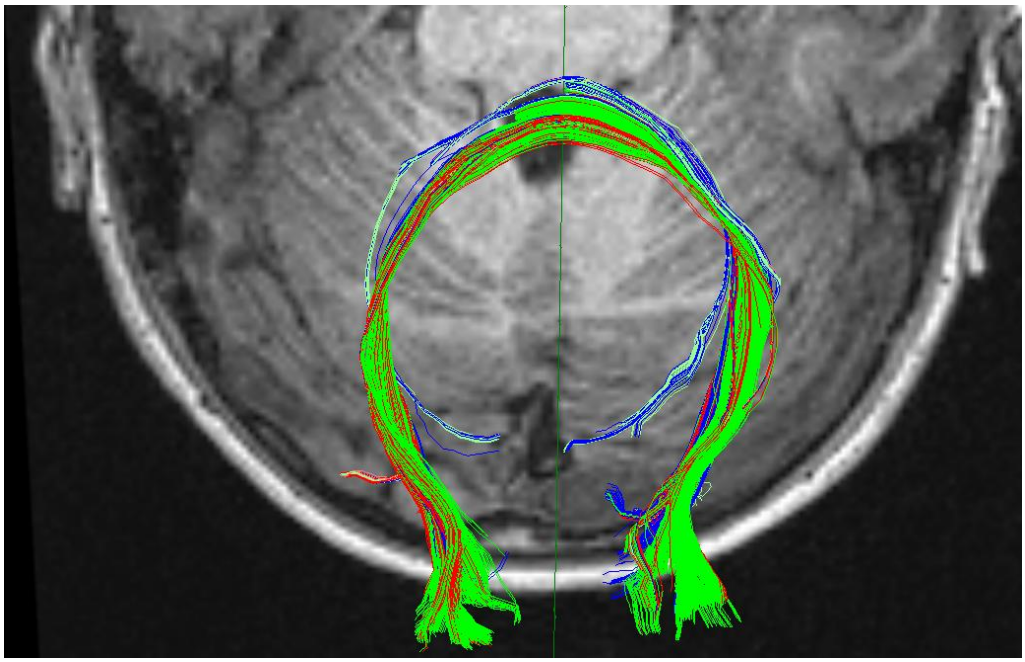

Figure 49: Schematic illustration of the visual-callosal fiber tracts identification according to each seed region in the visual cortex. We get 5 types of fibers: V1 (blue); dorsal V2 (light green); ventral V2 (dark green); dorsal V3 (red) and ventral V3 (dark red)

We conducted a parallel fiber identification approach where we only kept the information for visual-callosal WM pathways with seed points in the same visual region identified in both brain hemispheres.

The rational to perform this second methodology were:

1) this a more robust approach
2) If there is a estimation of a fiber amount with seed points in a particularly visual region in one hemisphere but not in the other, the estimated fiber tracts are not kept for the statistical analysis, leaving us only with those identified with seed points in the two brain hemispheres (figure 49).

To this approach we call in the results sub-section as the “robust approach”.

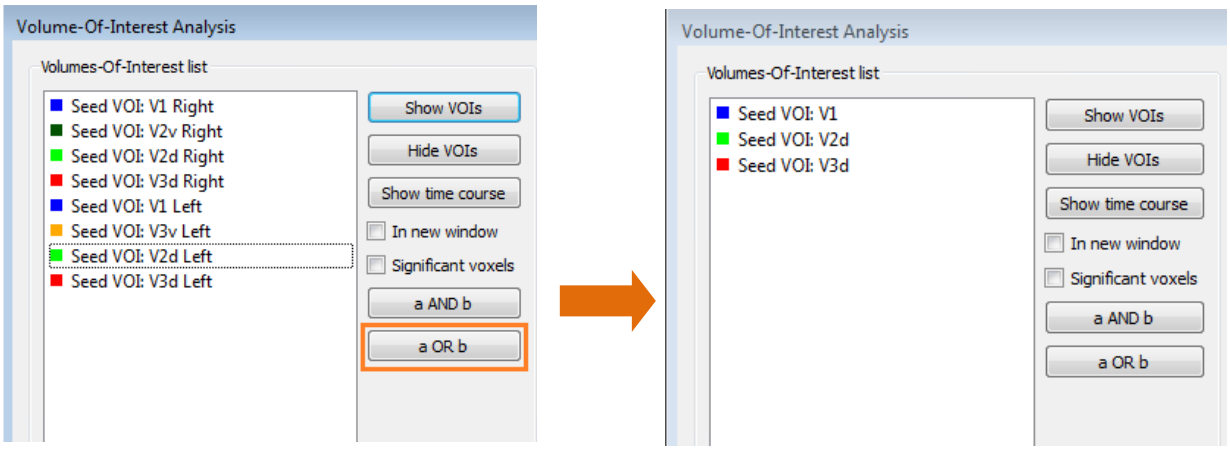

Figure 50: In this example there was identification in fiber tracts with seed points in visual region ventral V2 in the right hemisphere, and in ventral V3 in the left hemisphere, however no fibers were identified with seed points in the other hemisphere for both cases. In this approach the information of those fibers is not kept for the statistical analysis

RESULTS

This section is separated in two parts, referent to the results observed with both fiber identification approaches.

8.1. First identification approach

8.1.1. Percentage of fiber identification, according to each seed visual region in control subjects and in patients with NF1

Our fiber identification approach allowed us to identify fiber tracts starting in visual regions V1 and dorsal V2 for all control subjects and NF1 patients. Fiber tracts starting in dorsal V3 are identified for all controls subjects, in contrast to NF1 patients, where there is fiber identification in approximately 92% of adults. Fiber tracts starting in ventral regions are those with the lowest percentage of identification, but still with a considerable degree of identification, ranging between 78 and 90% of individuals, with the lowest case occurring for the identification of fiber tracts starting in ventral V2 regions of the visual cortex, for children.

With ANOVA repeated measures and multivariate analysis we identify with this fiber identification approach a total of: 17 healthy volunteer and 16 children with NF1 and 18 healthy volunteer and 10 adults with NF1, comprising the chort with 100% success in fiber identification for all regions.

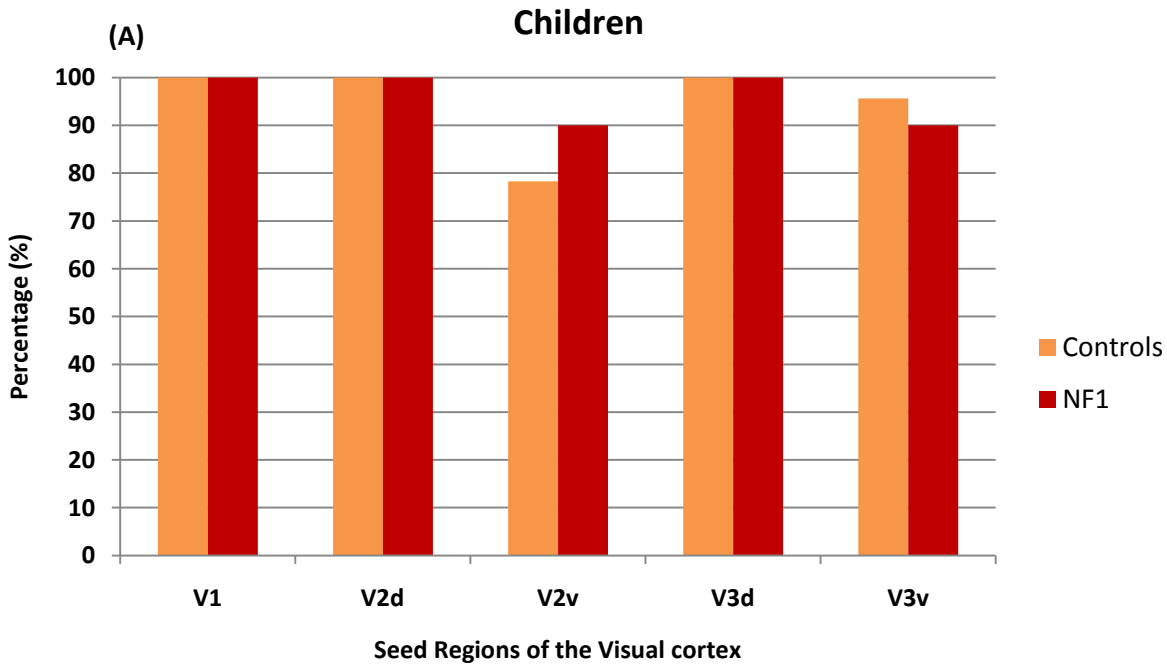

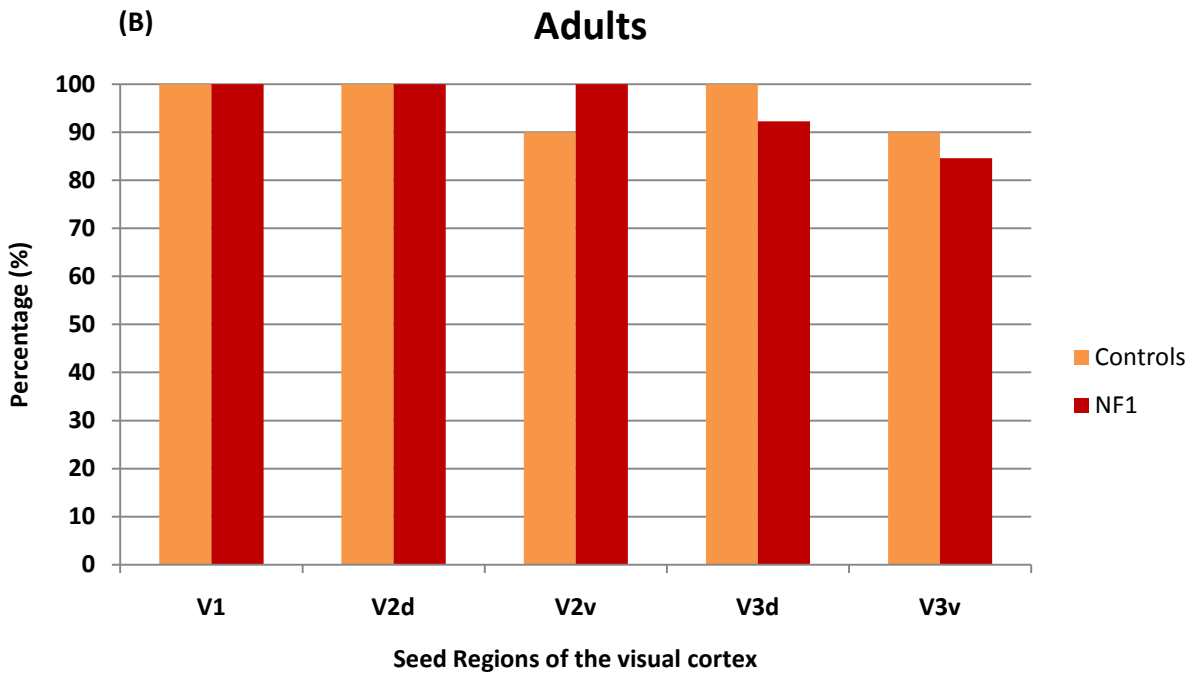

Graphic1: Percentage of fiber identification, according to each seed visual region in control subjects and patients with NF1 separated between (A) children and (B) adults.

8.1.2. Statistical analysis in Visual-Callosal pathways

Statistical analysis on diffusion parameters, eigenvalues and ellipsoid's specificities revealed a significant group effect for all measures in children, except for the mean variance of the main eigenvalue (λ_1) of the diffusion tensor (Tables 4 and 5). In adults it was also verified a significant group effect, however with less significance and in fewer variables. A significant group effect was verified in the two lower eigenvalues λ_2 and λ_3 (Table 5) and a specific anisotropic measure describing the deviation shape of the diffusion ellipsoid from a full spherical shape.

Table 14: Statistical analysis of the group effect in isotropic and anisotropic diffusion parameters

		FA	Axial FA	MD
Children	**Controls (mean ± SD)**	0.584 ± 0.045	0.396 ± 0.047	0.259 ± 0.019
	NF1 (mean ± SD)	0.548 ± 0.039	0.355 ± 0.037	0.273 ± 0.014
	ANOVA repeated measures	$F_{(1,\ 0.142)} = 8.790$	$F_{(1,\ 0.144)} = 11.839$	$F_{(1,\ 0.023)} = 10.96$
		p= 0.006 *	**p= 0.002 ***	**p= 0.002 ***
Adults	**Controls (mean ± SD)**	0.580 ± 0.037	0.387 ± 0.039	0.254 ± 0.015
	NF1 (mean ± SD	0.572 ± 0.034	0.365 ± 0.048	0.264 ± 0.016
	ANOVA repeated measures	$F_{(1,\ 0.084)} = 0.746$	$F_{(1,\ 0.142)} = 3.591$	$F_{(1,\ 0.013)} = 2.313$
		p= 0.396	p= 0.069	p= 0.14

Table 15: Statistical analysis of group effect in eigensystem parameters

		λ_1	λ_2	λ_3
Children	**Controls (mean ± SD)**	0.0015 ± 7.3E-05	0.00062 ± 7.5E-05	0.00042 ± 7.4E-05
	NF1 (mean ± SD)	0.0016 ± 5.9E-05	0.00069 ± 6.1E-05	0.00049 ± 5.7E-05
	ANOVA repeated measures	$F_{(1,\ 2.857E\text{-}7)} = 1{,}931$	$F_{(1,\ 3.751E\text{-}7)} = 12.329$	$F_{(1,\ 3.894E\text{-}7)} = 12.572$
		p= 0.175	**p= 0.001 ***	**p= 0.001 ***
Adults	**Controls (mean ± SD)**	0.0015 ± 7.3E-05	0.00062 ± 5.6E-05	0.00042 ± 5.6E-05
	NF1 (mean ± SD)	0.0015 ± 8.0E-05	0.00066 ± 7.6E-05	0.00047 ± 7.7E-05
	ANOVA repeated measures	$F_{(1,\ 2.604E\text{-}7)} = 1{,}915$	$F_{(1,\ 3.468E\text{-}7)} = 4.432$	$F_{(1,\ 3.817E\text{-}7)} = 5.497$
		p= 0.178	**p= 0.045 ***	**p= 0.027 ***

8.1.2.1. Fractional Anisotropy (FA)

ANOVA repeated measures analysis showed us a significant group effect verified in visual-callosal WM pathways (Table 4; p= 0.006). With graphics 2 and 3 we conclude that this significant group effect is illustrated by a significant decrease of FA values in those pathways for NF1 patients. Independent-Samples t-test analysis was used to identify the pathways with the major FA differences between groups. The t-test analysis shows a significant FA decrease in all WM pathways in NF1 children compared to controls (Table 6). The greatest decrease occurs for the WM pathways with seed points in the primary visual cortex V1 (p=0.001). In adults, there is no group effect for any of the FA values in none of the estimated visual-callosal WM pathways.

Table 16: Statistical analysis of group effect in measures of FA in visual-callosal WM pathways with seed points in V1, dorsal V2, ventral V2, dorsal V3 and ventral V3

		Children	Adults
V1	**Controls (mean ± SD)**	0.573 ± 0.035	0.563 ± 0.02
	NF1 (mean ± SD)	0.538 ± 0.025	0.553 ± 0.027
	T - Test	t(41) = 3.710	t(31) =1.332
		p= 0.001 *	p= 0.193
Dorsal V2	**Controls (mean ± SD)**	0.59 ± 0.044	0.589 ± 0.03
	NF1 (mean ± SD)	0.555 ± 0.036	0.571 ± 0.044
	T - Test	t(41) = 2.820	t(31) = 1.380
		p= 0.007 *	p= 0.177
Ventral V2	**Controls (mean ± SD)**	0.587 ± 0.047	0.592 ± 0.046
	NF1 (mean ± SD)	0.551 ± 0.042	0.579 ± 0.032
	T - Test	t(34) = 2.458	t(29) = 0.893
		p= 0.019 *	p= 0.379
Dorsal V3	**Controls (mean ± SD)**	0.597 ± 0.045	0.579 ± 0.033
	NF1 (mean ± SD)	0.565 ± 0.032	0.581 ± 0.029
	T - Test	t(41) = 2.592	t(30) = -0.221
		p= 0.013 *	p= 0.826
Ventral V3	**Controls (mean ± SD)**	0.572 ± 0.049	0.578 ± 0.048
	NF1 (mean ± SD)	0.536 ± 0.055	0.574 ± 0.032
	T - Test	t(37) = 2.169	t(28) = 0.259
		p= 0.031 *	p= 0.798

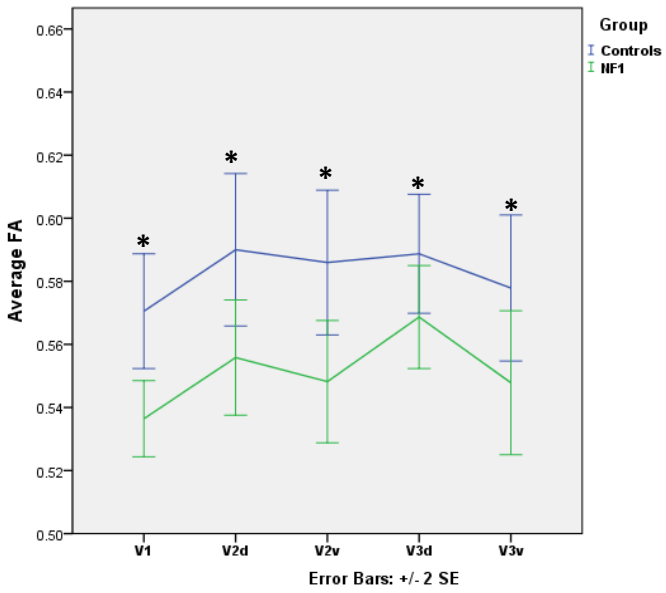

Graphic 2: Average FA of visual-callosal WM pathways with seed points in V1, V2d, V2v, V3d and V3v in children, on a group effect comparison between control subjects and NF1 patients.

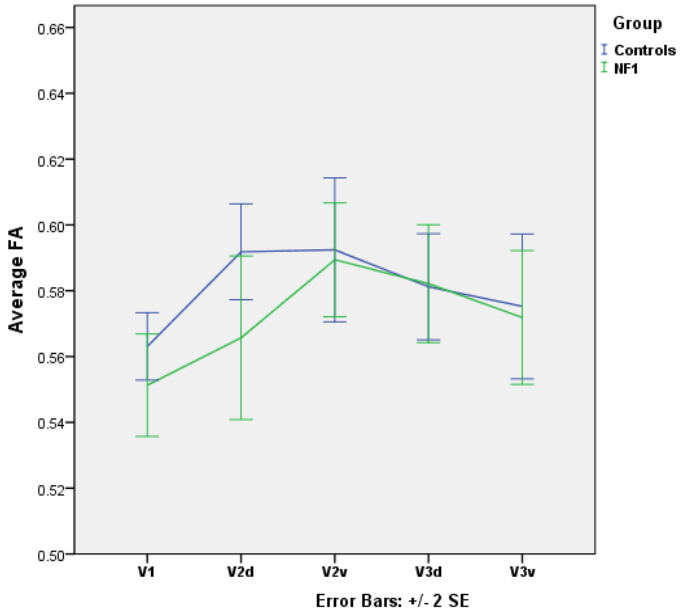

Graphic 3: Average FA of visual-callosal WM pathways with seed points in V1, V2d, V2v, V3d and V3v in adults, on a group effect comparison between control subjects and NF1 patients.

8.1.2.2. Axial Fractional Anisotropy (Axial FA)

Table 17: Statistical analysis of group effect in measures of Axial FA in visual-callosal WM pathways with seed points in V1, dorsal V2, ventral V2, dorsal V3 and ventral V3

		Children	Adults
V1	**Controls (mean ± SD)**	0.387 ± 0.034	0.371 ± 0.02
	NF1 (mean ± SD)	0.344 ± 0.022	0.349 ± 0.037
	T - Test	t(41) = 4.712	t(31) = 2.286
		p< 0.001 **	**p= 0.029 ***
Dorsal V2	**Controls (mean ± SD)**	0.405 ± 0.045	0.399 ± 0.032
	NF1 (mean ± SD)	0.366 ± 0.035	0.365 ± 0.052
	T - Test	t(41) = 3.175	t(31) = 2.341
		p= 0.003 *	**p= 0.026 ***
Ventral V2	**Controls (mean ± SD)**	0.399 ± 0.05	0.398 ± 0.048
	NF1 (mean ± SD)	0.354 ± 0.04	0.367 ± 0.044
	T - Test	t(34) = 2.901	t(29) = 1.892
		p= 0.006 *	p= 0.069
Dorsal V3	**Controls (mean ± SD)**	0.410 ± 0.045	0.386 ± 0.033
	NF1 (mean ± SD)	0.374 ± 0.031	0.382 ± 0.058
	T - Test	t(41) = 3.046	t(30) = 0.272
		p= 0.004 *	p= 0.787
Ventral V3	**Controls (mean ± SD)**	0.376 ± 0.056	0.381 ± 0.05
	NF1 (mean ± SD)	0.339 ± 0.05	0.364 ± 0.046
	T - Test	t(37) = 2.150	t(28) = 0.925
		p= 0.038 *	p= 0.363

Regarding the axial FA variance on visual-callosal WM pathways between controls and NF1, the significant group effect verified with the ANOVA repeated measure analysis (Table 4; p=0.002 for children) is properly illustrated as a significant axial FA decrease in NF1 individuals (Graphics 4 and 5). Independent-Samples t-test were used to identify the visual-callosal WM pathways contributing to the overall group effect verified in Table 4. A significant axial FA decrease is found in all children's visual-callosal WM pathways, while in adults we also verify a group effect, however with a higher p-value (Table 7) and only in WM pathways with seed points in V1 and dorsal V2.

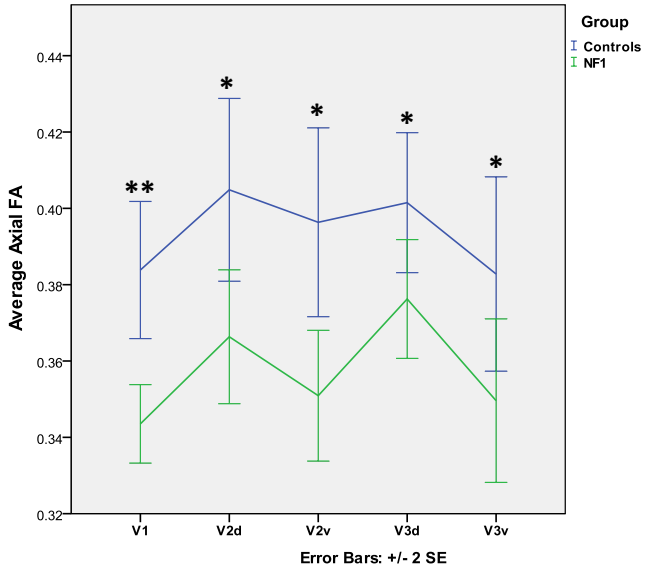

Graphic 4: Average axial FA of visual-callosal WM pathways with seed points in V1, V2d, V2v, V3d and V3v in children, on a group effect comparison between control subjects and NF1 patients

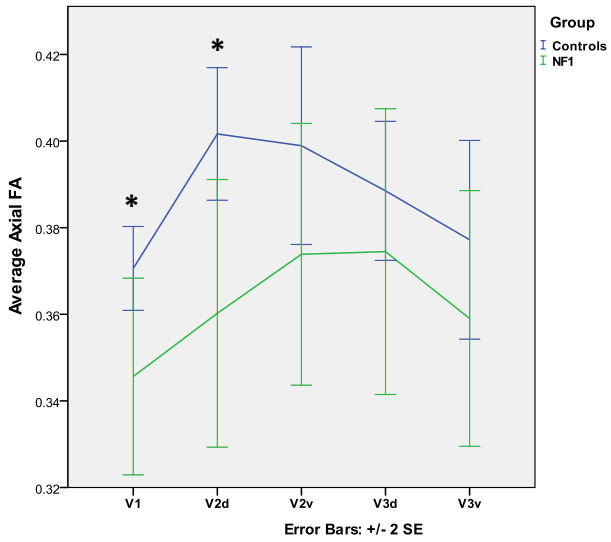

Graphic 5: Average axial FA of visual-callosal WM pathways with seed points in V1, V2d, V2v, V3d and V3v in adults, on a group effect comparison between control subjects and NF1 patients.

8.1.2.3. Mean Diffusivity (MD)

In visual-callosal WM pathways, we find a significant group effect both in children and adults (Table 9), reflected by a significant MD increase (Graphics 6 and 7). This increase is found in visual-callosal WM pathways with seed points in V1, dorsal V3 and also in dorsal and ventral V2 for the children group. In adults we observed a significant group effect, however with a higher p-value (Table 8) and only in WM pathways with seed points in dorsal and ventral V2.

Table 18: Statistical analysis of group effect in measures of MD in visual-callosal WM pathways with seed points in V1, dorsal V2, ventral V2, dorsal V3 and ventral V3.

		Children	Adults
V1	**Controls (mean ± SD)**	0.258 ± 0.013	0.0256 ± 0.012
	NF1 (mean ± SD)	0.275 ± 0.011	0.265 ± 0.017
	T - Test	t(41) = -4.788	t(31) = -1.708
		p< 0.001 **	p= 0.098
Dorsal V2	**Controls (mean ± SD)**	0.253 ± 0.013	0.248 ± 0.012
	NF1 (mean ± SD)	0.266 ± 0.011	0.262 ± 0.013
	T – Test	t(41) = -3.445	t(31) = -2.900
		p= 0.001 *	**p= 0.007 ***
Ventral V2	**Controls (mean ± SD)**	0.262 ± 0.018	0.254 ± 0.013
	NF1 (mean ± SD)	0.277 ± 0.014	0.271 ± 0.02
	T - Test	t(34) = -2.776	t(29) = -2.972
		p= 0.009 *	**p= 0.006 ***
Dorsal V3	**Controls (mean ± SD)**	0.251 ± 0.012	0.249 ± 0.011
	NF1 (mean ± SD)	0.266 ± 0.009	0.255 ± 0.011
	T - Test	t(41) = -4.392	t(30) = -1.353
		p< 0.001 **	p= 0.186
Ventral V3	**Controls (mean ± SD)**	0.271 ± 0.028	0.262 ± 0.02
	NF1 (mean ± SD)	0.281 ± 0.016	0.266 ± 0.011
	T - Test	t(37) = -1.290	t(28) = -0.560
		p= 0.205	p= 0.791

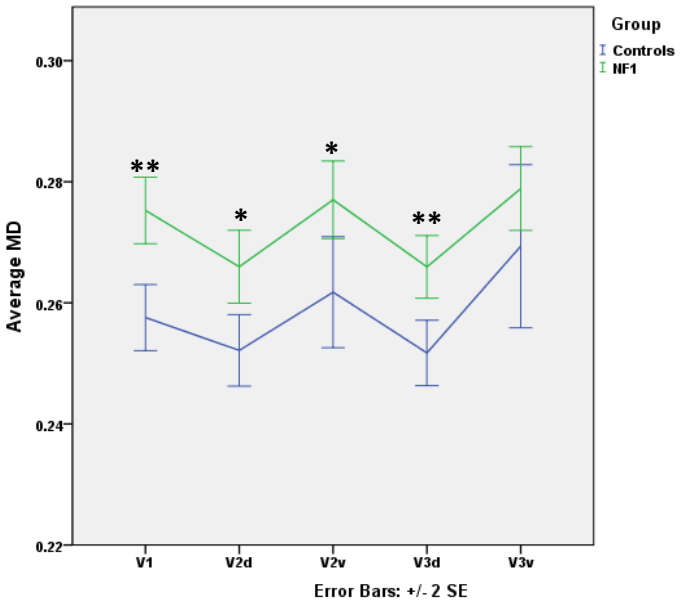

Graphic 6: Average MD of visual-callosal WM pathways with seed points in V1, V2d, V2v, V3d and V3v in children, on a group effect comparison between control subjects and NF1 patients.

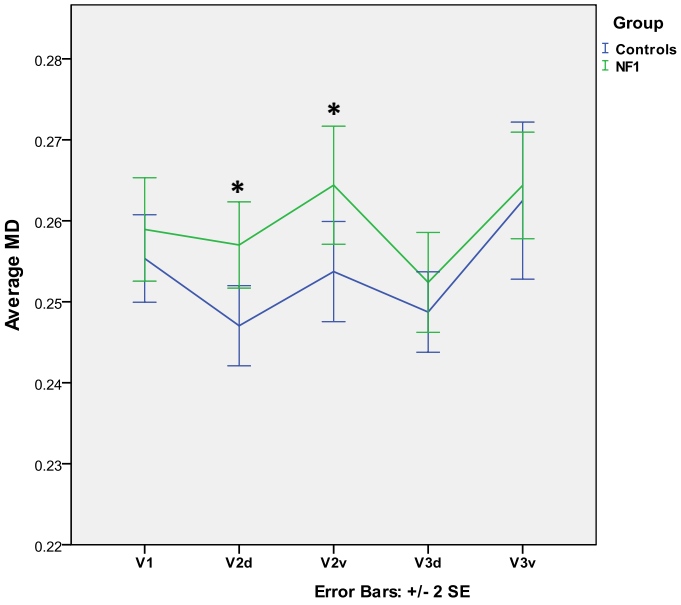

Graphic 7: Average MD of visual-callosal WM pathways with seed points in V1, V2d, V2v and V3d, V3v in adults, on a group effect comparison between control subjects and NF1 patients.

8.1.2.4. Eigenvalues (λ_1, λ_2 and λ_3)

Table 9: Statistical analysis of group effect in measures of λ_2 and λ_3 in visual-callosal WM pathways with seed points in V1, dorsal V2, ventral V2, dorsal V3 and ventral V3

		λ_2		λ_3	
		Children	**Adults**	**Children**	**Adults**
V1	**Controls (mean ± SD)**	0.00062 ± 4.8E-0.5	0.00064 ± 3.5E-05	0.00043 ± 5.3E-05	0.00044 ± 4.0E-05
	NF1 (mean ± SD)	0.0007 ± 3.8E-05	0.00068 ± 6.6E-05	0.00051 ± 3.8E-05	0.00049 ± 7.1E-05
	T - Test	t(41) = -5.386	t(16.287) = -2.315	t(41) = -5.196	t(17.014) = -2.369
		p< 0.001 **	**p= 0.034 ***	**p< 0.001 ****	**p= 0.03 ***
Dorsal V2	**Controls (mean ± SD)**	0.0006 ± 5.6E-05	0.0006 ± 4.5E-05	0.00041 ± 5.8E-05	0.0004 ± 4.7E-05
	NF1 (mean ± SD)	0.00066 ± 5.3E-05	0.00065 ± 6.8E-05	0.00047 ± 5.0E-05	0.00048 ± 6.8E-05
	T - Test	t(41) = -3.672	t(31) = -2.936	t(41) = -3.680	t(31) = -3.379
		p= 0.001 *	**p= 0.006 ***	**p= 0.001 ***	**p= 0.002 ***
Ventral V2	**Controls (mean ± SD)**	0.00062 ± 7.9E-05	0.00061 ± 6.3E-05	0.00043 ± 7.9E-05	0.00041 ± 5.7E-05
	NF1 (mean ± SD)	0.00069 ± 6.2E-05	0.00068 ± 8.5E-05	0.0005 ± 5.9E-05	0.00049 ± 8.7E-05
	T - Test	t(34) = -2.950	t(29) = -2.722	t(34) = -3.012	t(29) = -3.024
		p= 0.006 *	**p= 0.011 ***	**p= 0.005 ***	**p= 0.005 ***
Dorsal V3	**Controls (mean ± SD)**	0.00059 ± 5.4E-05	0.00061 ± 4.3E-05	0.0004 ± 5.6E-05	0.00041 ± 4.5E-05
	NF1 (mean ± SD)	0.00065 ± 4.6E-05	0.000063 ± 8.2E-05	0.00046 ± 4.2E-05	0.00044 ± 8.2E-05
	T - Test	t(41) = -3.868	t(14.708) = -0.779	t(41) = -4.164	t(15.014) = -1.365
		p< 0.001 **	p= 0.448	**p< 0.001 ****	p= 0.192
Ventral V3	**Controls (mean ± SD)**	0.00066 ± 1.1E-05	0.00064 ± 7.8E-05	0.00046 ± 1.0E-05	0.00044 ± 7.7E-05
	NF1 (mean ± SD)	0.00072 ± 8.1E-05	0.00067 ± 7.6E-05	0.00052 ± 7.1E-05	0.00048 ± 7.7E-05
	T - Test	t(37) = -1.662	t(28) = -1.051	t(37) = -1.874	t(28) = -1.217
		p= 0.105	p= 0.302	p= 0.069	p= 0.234

ANOVA repeated measures analysis showed no general group effects in the mean variance of the major eigenvalue (λ_1) of the diffusion tensor, however it was verified a significant group effect for the mean variance of the two lower eigenvalues (Table 5). With the Independent-Samples t-test analysis we verify a highly significant group effect, illustrated by an increase in the two lower eigenvalues $(\lambda_2 \text{ and } \lambda_3)$ in visual-callosal WM pathways with seed points in V1 and dorsal V3, for children with NF1. A group effect is also verified in children for WM pathways with seed points in dorsal and ventral V2 as well (Table 9). In adults, a significant group effect is verified for WM pathways with seed points in V1 and dorsal and ventral V2.

Following next we illustrate the average values of the eigenvalues in the visual-callosal WM pathways for children and adults, comparing and illustrating the significant differences between the control and NF1 groups.

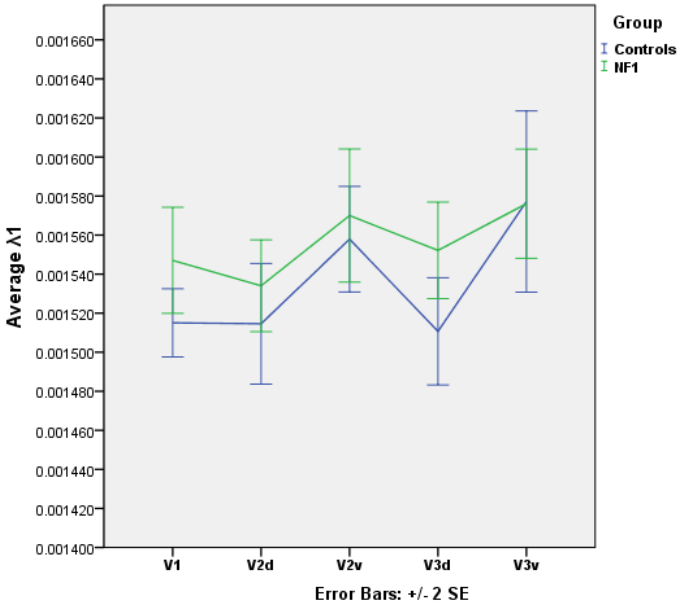

Graphic 8: Average λ_1 of visual-callosal WM pathways with seed points in V1, V2d, V2v, V3d and V3v in children, on a group effect comparison between control subjects and NF1 patients.

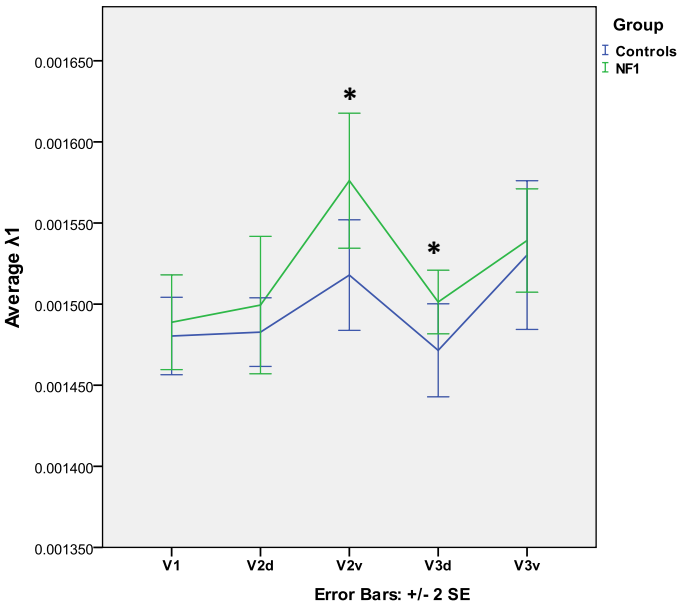

Graphic 9: Average λ_1 of visual-callosal WM pathways with seed points in V1, V2d, V2v, V3d and V3v in adults, on a group effect comparison between control subjects and NF1 patients.

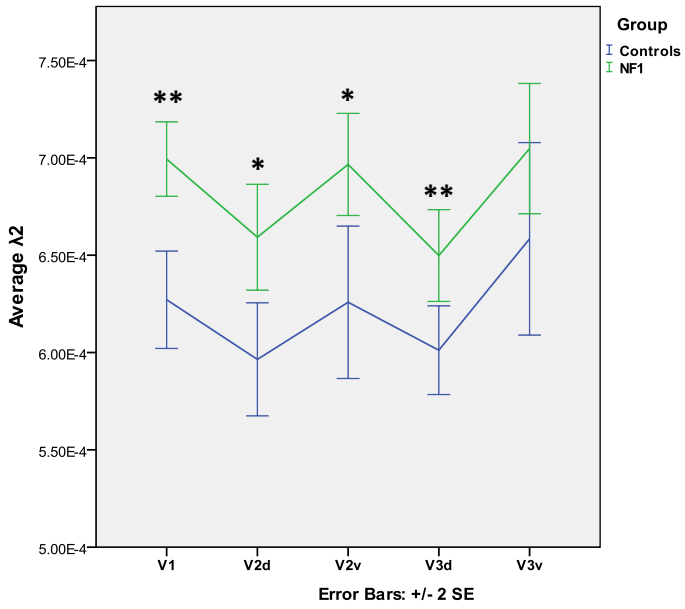

Graphic 10: Average λ_2 of visual-callosal WM pathways with seed points in V1, V2d, V2v, V3d and V3v in children, on a group effect comparison between control subjects and NF1 patients.

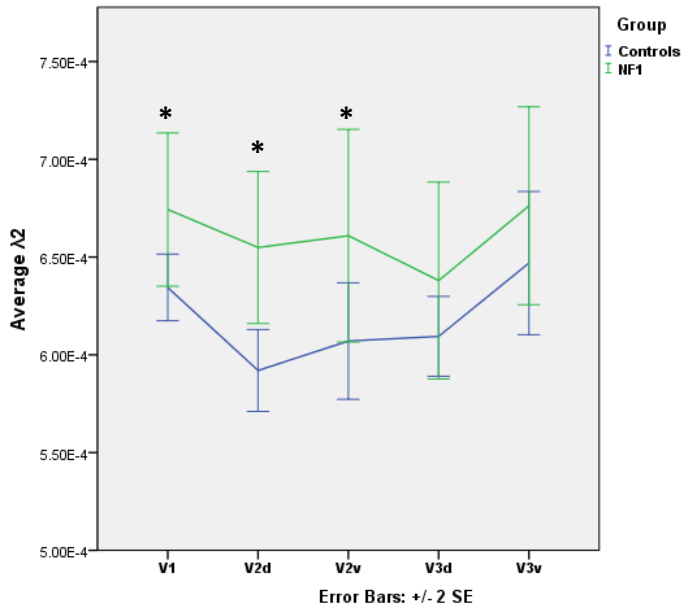

Graphic 11: Average λ_2 of visual-callosal WM pathways with seed points in V1, V2d, V2v, V3d and V3v in adults, on a group effect comparison between control subjects and NF1 patients.

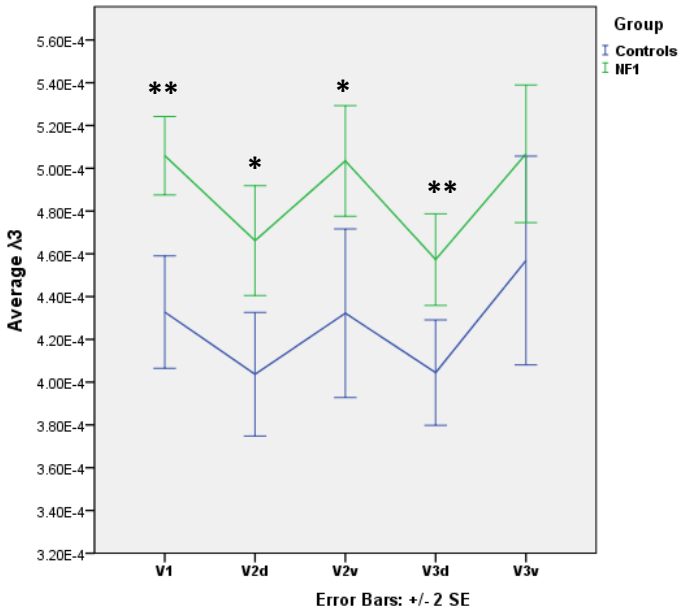

Graphic 12: Average λ_3 of visual-callosal WM pathways with seed points in V1, V2d, V2v, V3d and V3v in children, on a group effect comparison between control subjects and NF1 patients.

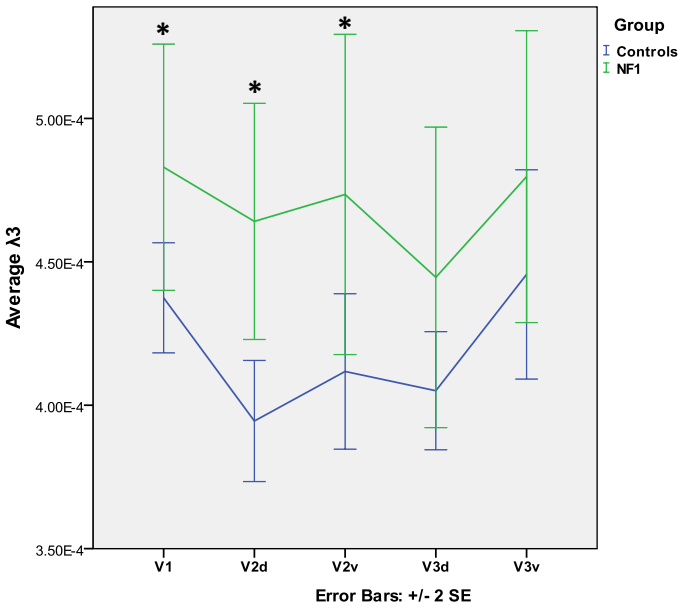

Graphic 13: Average λ_3 of visual-callosal WM pathways with seed points in V1, V2d, V2v, V3d and V3v in adults, on a group effect comparison between control subjects and NF1 patients.

8.1.2.5. Age effect

No correlations with age were found for none diffusion parameter or eigensystem value in all WM pathways identified for both children and adults in the control and NF1 group ($p>0.1$).

8.2. Robust fiber identification approach

With the first identification approach there is an occurrence that we need to analyze in more detail: in some individuals we identify fiber tracts projecting towards a particular region of the visual cortex in one brain hemisphere, but not in the same functional region in the other. This fact can be explained with several possibilities, like the fiber tracking algorithm used in the BrainVoyager tractography or even the presence of a tumour/abnormality in one hemisphere of the brain. It must be taken in consideration that the same visual region is not equal for the two hemispheres of the brain, and this might also be an explanation for this lack in the fiber identification.

So it was decided to analyze the fiber tracts with another fiber identification approach, where there are only kept the fibers identified with seed points in the two brain hemispheres. This is done in order to make a comparison with our first fiber identification to see if there is any difference in the statistical analysis between the two approaches.

8.2.1. Percentage of fiber identification, according to each seed visual region in control subjects and patients with NF1

The more robust fiber identification approach also enabled the identification of visual-callosal WM pathways starting in visual regions V1, dorsal V2, ventral V2, dorsal V3 and ventral V3. However with lower detection, the percentage of subjects where these fibers are identified suffered a decrease, as expected: we have fiber tract identification with seed points in V1 in 90% and 100% for children in the control and NF1 group respectively, while in adults there is an identification in approximately 90% of the individuals in both groups. Both fiber tracts with seed points in visual dorsal regions V2 and V3 are identified in between 80 and 95% for children and adult controls, while in the NF1 group they are identified in a lower percentage of subjects and patients, varying between 50 and 80% of individuals. Fiber tracts starting in ventral regions are those with the lowest percentage of identification, with an identification degree percentage ranging between 40 and 50% of individuals for fiber tracts with seed points in V2, and between 50 and 60% for fibers starting in V3.

With ANOVA repeated measures analysis we identify a total of: 7 healthy volunteer and 7 children patients with NF1 and 7 healthy volunteer and only 3 adults with NF1 where we identify visual-callosal WM pathways with seed points in all visual regions (V1, dorsal V2, ventral V2, dorsal V3 and ventral V3)

.

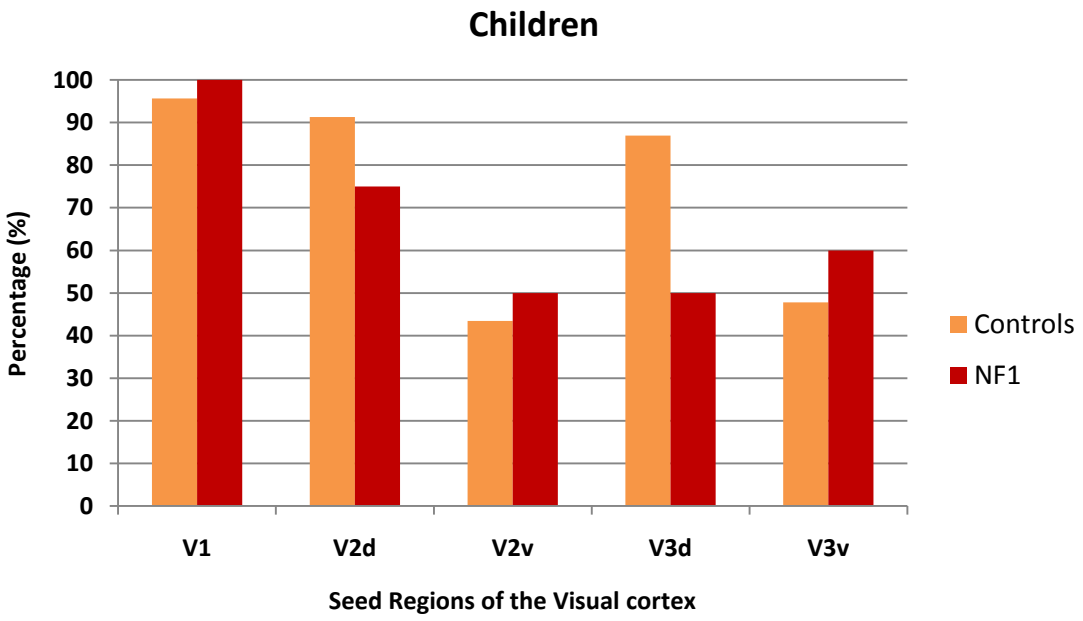

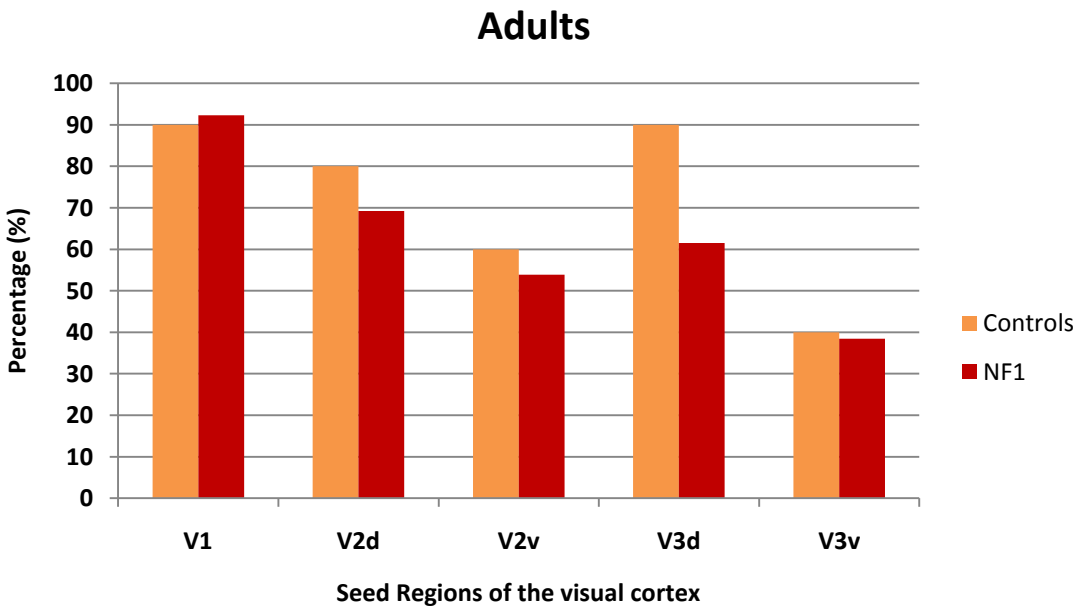

Graphic 14: Percentage of fiber identification, according to each seed visual region in control subjects and patients with NF1 separated between (A) children and (B) adults.

8.2.2. Statistical analysis in Visual-Callosal pathways

Statistical analysis on diffusion parameters and eigenvalues revealed significant group effect for all measures in children, except for the mean variance of MD and the main eigenvalue (λ_1) of the diffusion tensor. In adults, no significant group effect is verified in any of our measures (Tables 10 and 11).

Table 10: Statistical analysis of the group effect in isotropic and anisotropic diffusion parameters

		FA	Axial FA	MD
Children	**Controls (mean ± SD)**	0.582 ± 0.039	0.395 ± 0.04	0.256 ± 0.014
	NF1 (mean ± SD)	0.546 ± 0.033	0.353 ± 0.031	0.274 ± 0.014
	ANOVA repeated measures	F(1, 0.065) = 6.112	F(1, 0.076) = 7.234	F(1, 0.014) = 4.469
		p= 0.029 *	**p= 0.02 ***	p= 0.058
Adults	**Controls (mean ± SD)**	0.578 ± 0.031	0.386 ± 0.032	0.252 ± 0.013
	NF1 (mean ± SD	0.565 ± 0.031	0.358 ± 0.04	0.262 ± 0.014
	ANOVA repeated measures	F(1, 0.012) = 0.226	F(1, 0.011) = 1.005	F(1, 0.005) = 2.084
		p= 0.647	p= 0.346	P= 0.187

Table 191: Statistical analysis of group effect in eigensystem parameters.

		λ_1	λ_2	λ_3
Children	**Controls (mean ± SD)**	0.0015 ± 6.0E-05	0.00062 ± 5.7E-05	0.00042 ± 5.9E-05
	NF1 (mean ± SD)	0.0016 ± 5.7E-05	0.00069 ± 5.8E-05	0.00049 ± 5.3E-05
	ANOVA repeated measures	$F_{(1,\ 8.186E-9)}$ = 0.791	$F_{(1,\ 2.111E-7)}$ = 6.798	$F_{(1,\ 2.399E-7)}$ = 6.503
		p= 0.391	**p= 0.023 ***	**p= 0.025 ***
Adults	**Controls (mean ± SD)**	0.0015 ± 6.3E-05	0.00062 ± 4.5E-05	0.00042 ± 4.7E-05
	NF1 (mean ± SD)	0.0015 ± 7.0E-05	0.00067 ± 6.7E-05	0.00047 ± 7.1E-05
	ANOVA repeated measures	$F_{(1,\ 9.477E-8)}$ = 1.798	$F_{(1,\ 4.224E-8)}$ = 2.032	$F_{(1,\ 5.552E-8)}$ = 1.539
		p= 0.217	p= 0.192	p= 0.25

8.2.2.1. Fractional Anisotropy (FA)

With the robust fiber tract identification approach, we have a lower statistical power when compared to our first approach, and consequently the statistical differences found in the group effect on the ANOVA repeated measures and Independent-Samples t-test analysis are lower or even inexistent (p-value too high). For this fact, our Independent-Samples t-test analysis shows us a significant FA decrease in NF1's children WM pathways with seed points in V1, dorsal and ventral V2 and dorsal V3 (Table 12).

Table 20: Statistical analysis of group effect in measures of FA in visual-callosal WM pathways with seed points in V1, dorsal V2, ventral V2, dorsal V3 and ventral V3.

		Children	Adults
V1	**Controls (mean ± SD)**	0.571 ± 0.034	0.563 ± 0.022
	NF1 (mean ± SD)	0.54 ± 0.025	0.553 ± 0.027
	T - Test	t(39) = 3.365	t(29) = 1.176
		p= 0.02 *	p= 0.249
Dorsal V2	**Controls (mean ± SD)**	0.582 ± 0.039	0.591 ± 0.029
	NF1 (mean ± SD)	0.546 ± 0.03	0.55 ± 0.02
	T – Test	t(35) = 3.012	t(23) = 3.784
		p= 0.005 *	**p= 0.001 ***
Ventral V2	**Controls (mean ± SD)**	0.586 ± 0.043	0.577 ± 0.045
	NF1 (mean ± SD)	0.54 ± 0.029	0.594 ± 0.028
	T - Test	t(18) = 2.789	t(17) = -0.939
		p= 0.012 *	p= 0.361
Dorsal V3	**Controls (mean ± SD)**	0.59 ± 0.042	0.583 ± 0.032
	NF1 (mean ± SD)	0.562 ± 0.033	0.576 ± 0.027
	T - Test	t(34) = 2.118	t(24) = 0.536
		p= 0.042 *	p= 0.597
Ventral V3	**Controls (mean ± SD)**	0.581 ± 0.037	0.585 ± 0.023
	NF1 (mean ± SD)	0.546 ± 0.054	0.57 ± 0.043
	T - Test	t(19) = 1.738	t(11) = 0.834
		p= 0.098	p= 0.422

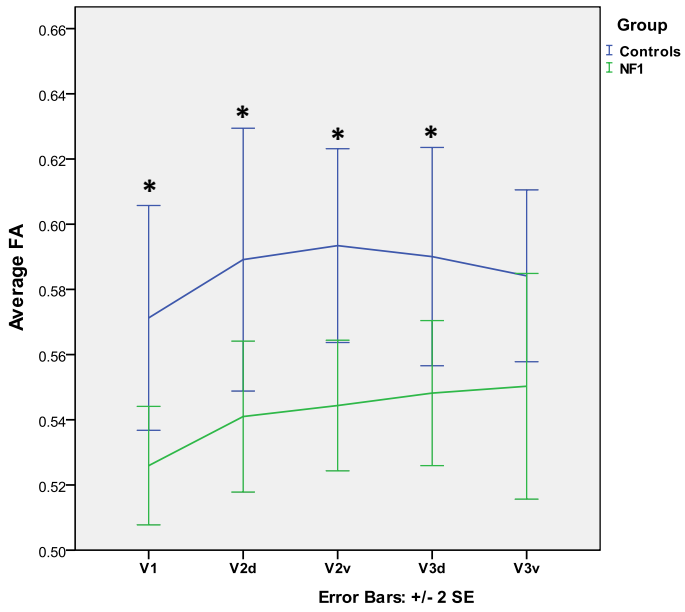

Graphic 15: Average FA in visual-callosal WM pathways with seed points in V1, V2d, V2v, V3d and V3v in children, on a group effect comparison between control subjects and NF1 patients.

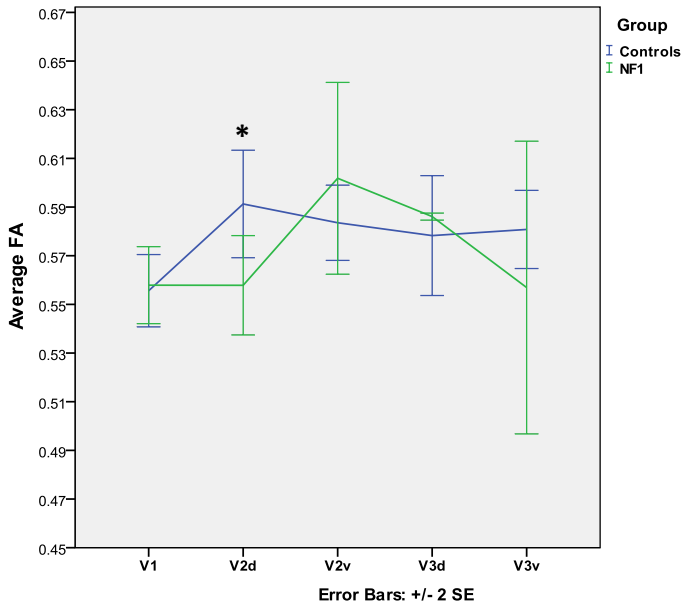

Graphic 16: Average FA in visual-callosal WM pathways with seed points in V1, V2d, V2v, V3d and V3v in adults, on a group effect comparison between control subjects and NF1 patients.

8.2.2.2. Axial Fractional Anisotropy (Axial FA)

Regarding the axial FA variance on visual-callosal WM pathways between controls and NF1, with ANOVA analysis we verify a significant group effect, illustrated in a significant axial FA decrease for children with NF1 (Graphics 19 and 20). A significant axial FA decrease is found in visual-callosal WM pathways with seed points in all visual areas of the cortex for children, while in adults we verify a significant group effect only for the visual-callosal WM pathways identified with seed points in V1 and dorsal V2 (Table 13).

Table 13: Statistical analysis of group effect in measures of Axial FA in visual-callosal WM pathways with seed points in V1, dorsal V2, ventral V2, dorsal V3 and ventral V3.

		Children	Adults
V1	**Controls (mean ± SD)**	0.384 ± 0.033	0.371 ± 0.021
	NF1 (mean ± SD)	0.346 ± 0.021	0.349 ± 0.037
	T - Test	t(39) = 4.270	t(29) = 2.091
		p< 0.001 **	**p= 0.045 ***
Dorsal V2	**Controls (mean ± SD)**	0.397 ± 0.04	0.402 ± 0.03
	NF1 (mean ± SD)	0.357 ± 0.028	0.341 ± 0.03
	T – Test	t(35) = 3.358	F(23) = 4.888
		p= 0.002 *	**p< 0.001 ****
Ventral V2	**Controls (mean ± SD)**	0.398 ± 0.048	0.383 ± 0.045
	NF1 (mean ± SD)	0.343 ± 0.029	0.371 ± 0.055
	T - Test	t(18) = 3.080	t(17) = 0.521
		p= 0.008 *	p= 0.609
Dorsal V3	**Controls (mean ± SD)**	0.403 ± 0.042	0.39 ± 0.032
	NF1 (mean ± SD)	0.371 ± 0.031	0.373 ± 0.039
	T - Test	t(34) = 2.513	t(24) = 1.201
		p= 0.017 *	p= 0.241
Ventral V3	**Controls (mean ± SD)**	0.388 ± 0.039	0.39 ± 0.025
	NF1 (mean ± SD)	0.346 ± 0.051	0.373 ± 0.036
	T - Test	t(19) = 2.149	t(11) = 0.971
		p= 0.045 *	p= 0.352

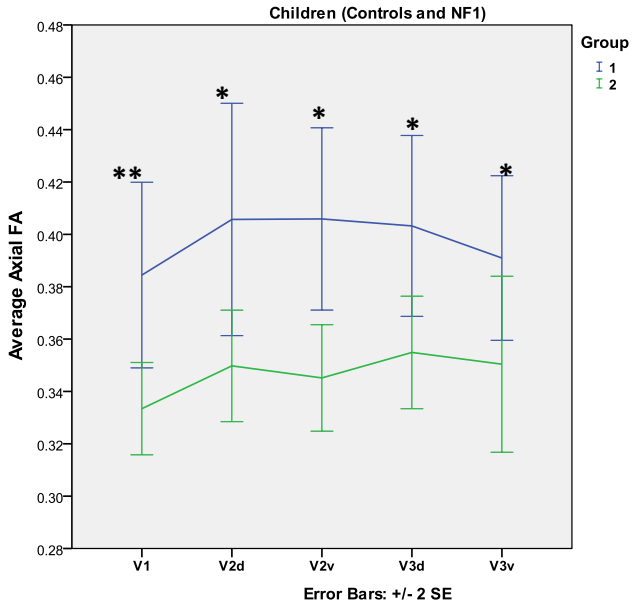

Graphic 17: Average Axial FA in visual-callosal WM pathways with seed points in V1, V2d, V2v, V3d and V3v in children, on a group effect comparison between control subjects and NF1 patients.

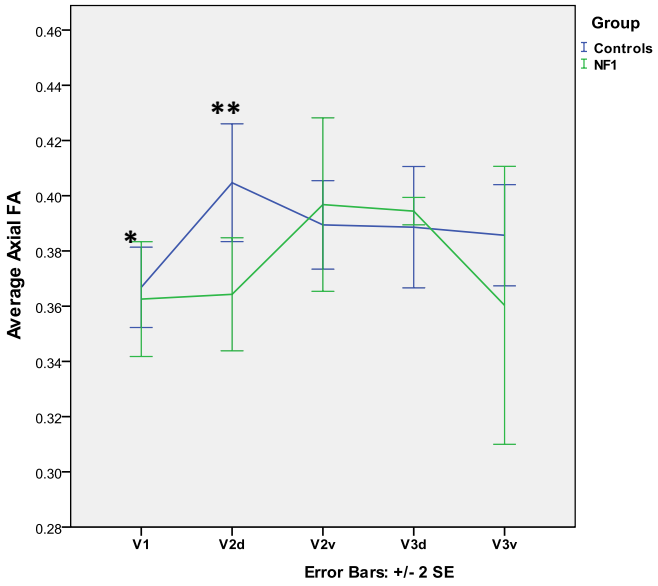

Graphic 18: Average Axial FA in visual-callosal WM pathways with seed points in V1, V2d, V2v, V3d and V3v in adults, on a group effect comparison between control subjects and NF1 patients.

8.2.2.3. Mean Diffusivity (MD)

ANOVA repeated measures analysis had not shown a significant group effect in the variance of MD values between controls and NF1 (Table 12; p=0.058), however we find a significant group effect with the independent-samples t-test, in children for all visual-callosal WM pathways. In adults the only exception is a group effect, illustrated by a MD increase in

NF1's individuals, which we verify in visual-callosal WM pathways with seed points in visual region ventral V2 in children and dorsal V2 in adults. This group effect happens because of the number of individuals analyzed in each analysis, since ANOVA repeated measures is a more robust statistical method, resulting as we said for this approach on the analysis of only 14 children and 10 adults. Independent-samples t-test analyzes a highest number of individuals where each pathway is identified independently from the identified WM pathways with seed points in other region in the visual cortex.

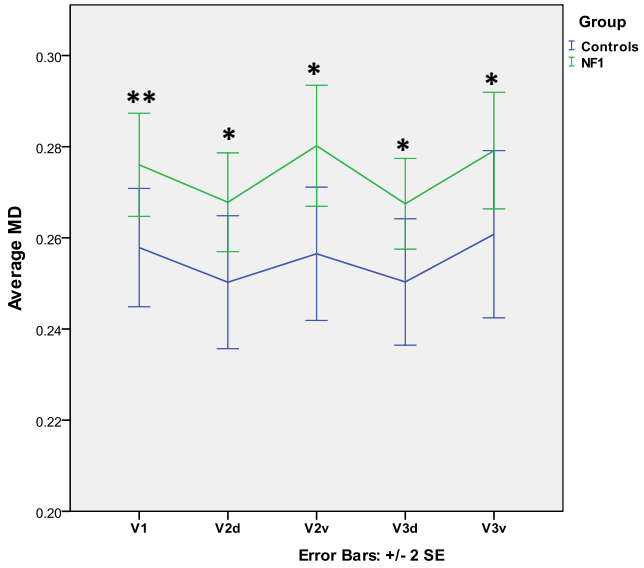

Graphic 19: Average MD in visual-callosal WM pathways with seed points in V1, V2d, V2v, V3d and V3v in children, on a group effect comparison between control subjects and NF1 patients.

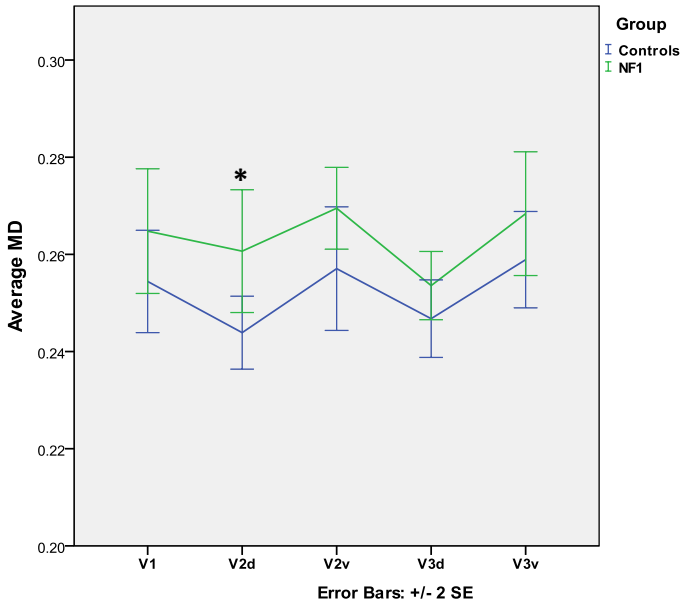

Graphic 20: Average MD in visual-callosal WM pathways with seed points in V1, V2d, V2v, V3d and V3v in adults, on a group effect comparison between control subjects and NF1 patients.

8.2.2.4. Eigenvalues (λ_1, λ_2 and λ_3)

Table 14: Statistical analysis of group effect in measures of λ_2 and λ_3 in visual-callosal WM pathways with seed points in V1, dorsal V2, ventral V2, dorsal V3 and ventral V3

		λ_2		λ_3	
		Children	**Adults**	**Children**	**Adults**
V1	**Controls (mean ± SD)**	0.00063 ± 4.8E-05	0.00063 ± 3.6E-05	0.00043 ± 5.1E-05	0.00044 ± 4.1E-05
	NF1 (mean ± SD)	0.0007 ± 3.8E-05	0.00068 ± 6.7E-05	0.0005 ± 3.7E-05	0.00049 ± 7.1E-05
	T - Test	t(39) = -4.921	t(17.103) = -2.320	t(39) = -4.826	t(17.722) = -2.393
		p< 0.001 **	**p= 0.033 ***	**p< 0.001 ****	**p= 0.028 ***
Dorsal V2	**Controls (mean ± SD)**	0.00061 ± 5.2E-05	0.00059 ± 4.5E-05	0.00041 ± 5.4E-05	0.0004 ± 4.9E-05
	NF1 (mean ± SD)	0.00067 ± 4.8E-05	0.00068 ± 5.4E-05	0.00048 ± 4.6E-05	0.00049 ± 5.9E-05
	T - Test	t(35) = -3.848	t(23) = -4.489	t(35) = -3.771	t(23) = -4.344
		p< 0.001 **	**p< 0.001 ****	**p= 0.001 ***	**p< 0.001 ****
Ventral V2	**Controls (mean ± SD)**	0.00062 ± 7.1E-05	0.00063 ± 6.2E-05	0.00042 ± 7.4E-05	0.00043 ± 5.6E-05
	NF1 (mean ± SD)	0.00071 ± 5.6E-05	0.00067 ± 9.8E-05	0.00051 ± 5.3E-05	0.00048 ± 1.2E-04
	T - Test	t(18) = -3.129	t(17) = -1.240	t(18) = -3.174	t(17) = -1.412
		p= 0.006 *	p= 0.232	**p= 0.005 ***	p= 0.176
Dorsal V3	**Controls (mean ± SD)**	0.0006 ± 5.2E-05	0.00061 ± 4.0E-05	0.0004 ± 5.5E-05	0.00041 ± 4.4E-05
	NF1 (mean ± SD)	0.00065 ± 4.7E-05	0.00064 ± 6.3E-05	0.00046 ± 4.3E-05	0.00044 ± 6.6E-05
	T - Test	t(34) = -3.160	t(24) = 0.067	t(34) = -3.513	t(24) = -1.596
		p= 0.003 *	p= 0.144	**P= 0.001 ***	p= 0.124
Ventral V3	**Controls (mean ± SD)**	0.00064 ± 6.4E-05	0.00062 ± 4.2E-05	0.00043 ± 6.3E-05	0.00043 ± 3.9E-05
	NF1 (mean ± SD)	0.00072 ± 9.4E-05	0.00065 ± 5.2E-05	0.00052 ± 8.7E-05	0.00045 ± 4.9E-05
	T - Test	t(19) = -2.340	t(11) = -1.154	t(19) = -2.616	t(11) = -0.879
		p= 0.03 *	p= 0.273	**p= 0.017***	p= 0.398

Independent-samples t-test analysis showed no significant group effect in the mean variance of the major eigenvalue $(\boldsymbol{\lambda_1})$ of the diffusion tensor for any visual-callosal WM pathway. With the ANOVA analysis we verify a significant group effect, illustrated by an increase in the lower eigenvalue $(\boldsymbol{\lambda_2}$ **and** $\boldsymbol{\lambda_3})$ in visual-callosal WM pathways with seed points in V1, dorsal V2, ventral V2 and dorsal V3. In adults, a significant group effect is verified for WM pathways with seed points in dorsal V2.

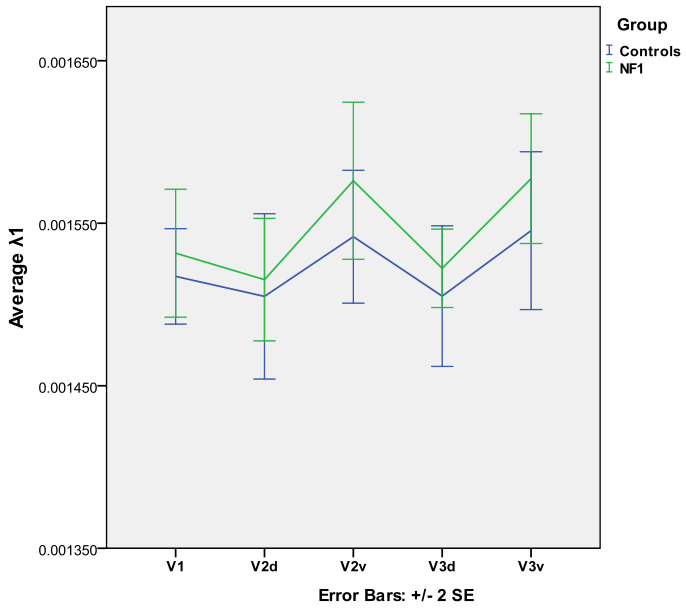

Graphic 21: Average λ_1 of visual-callosal WM pathways with seed points in V1, V2d, V2v, V3d and V3v in children, on a group effect comparison between control subjects and NF1 patients.

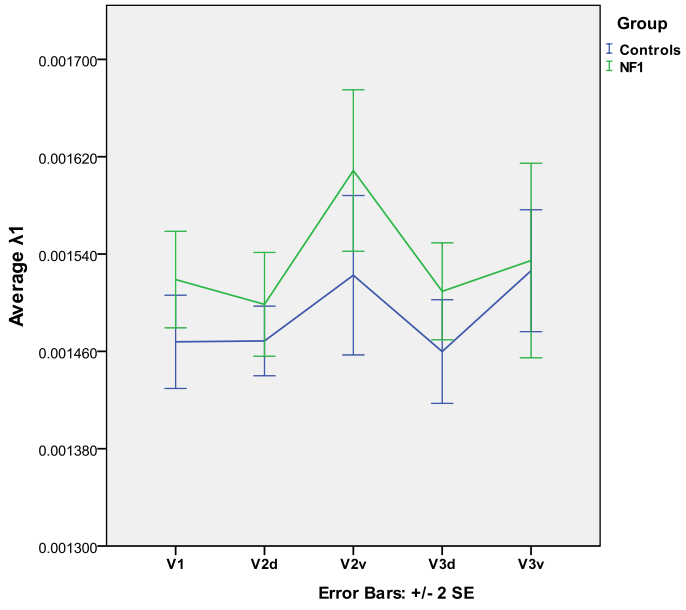

Graphic 22: Average λ_1 of visual-callosal WM pathways with seed points in V1, V2d, V2v, V3d and V3v in adults, on a group effect comparison between control subjects and NF1 patients.

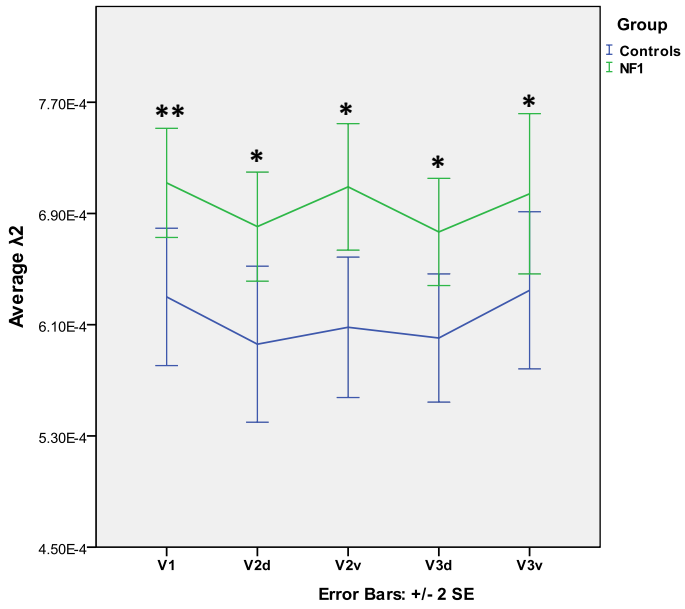

Graphic 23: Average λ_2 of visual-callosal WM pathways with seed points in V1, V2d, V2v, V3d and V3v in children, on a group effect comparison between control subjects and NF1 patients.

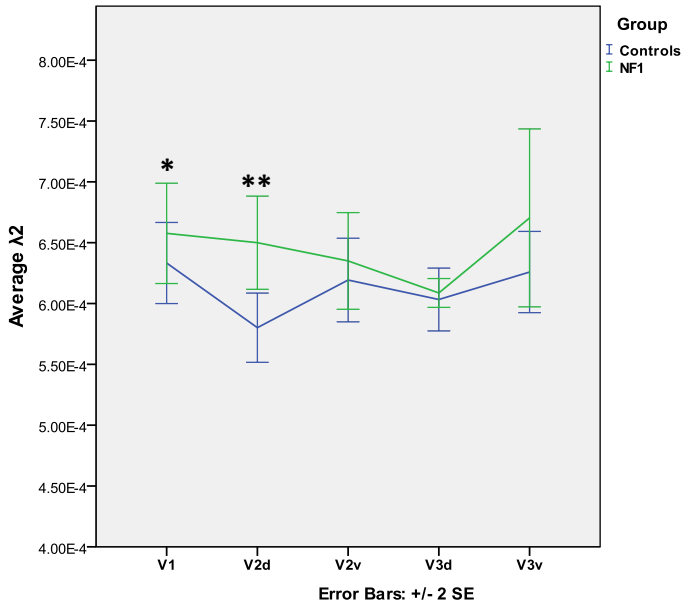

Graphic 24: Average λ_2 of visual-callosal WM pathways with seed points in V1, V2d, V2v, V3d and V3v in adults, on a group effect comparison between control subjects and NF1 patients.

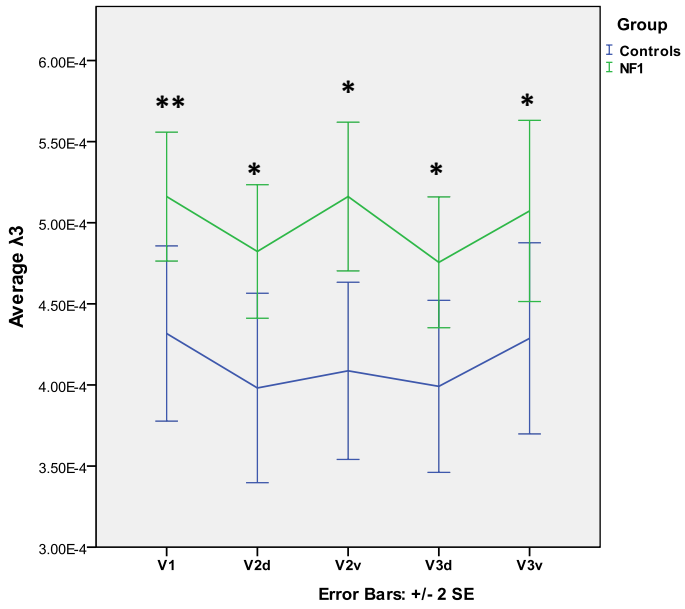

Graphic 25: Average λ_3 of visual-callosal WM pathways with seed points in V1, V2d, V2v, V3d and V3v in children, on a group effect comparison between control subjects and NF1 patients.

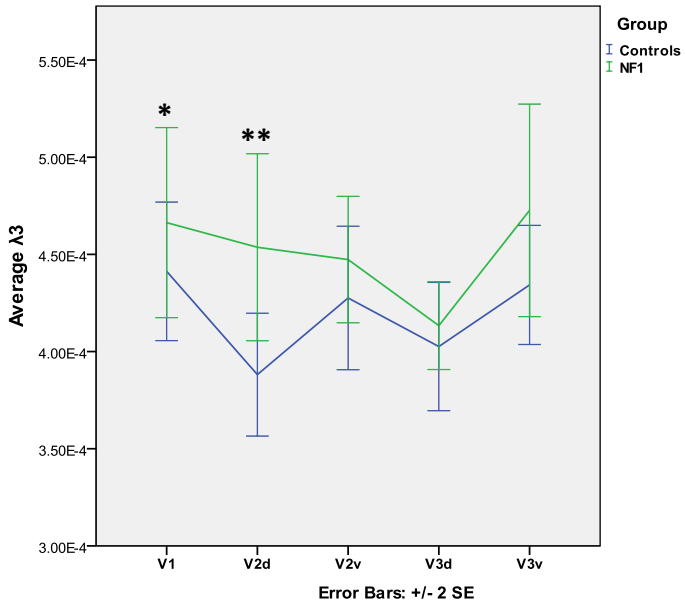

Graphic 26: Average λ_3 of visual-callosal WM pathways with seed points in V1, V2d, V2v, V3d and V3v in adults, on a group effect comparison between control subjects and NF1 patients.

8.2.2.5. Age effect

No correlations with age were found for none diffusion parameter or eigensystem value in all WM pathways identified for both children and adults in the control and NF1 group ($p>0.1$).

DISCUSSION

The methodology used describes both anatomical and diffusion properties of estimated visual-callosal WM pathways; identified according to their seed points in specific regions of the human visual cortex (V1, dorsal V2, ventral V2, dorsal V3 and ventral V3). These WM pathways are of great importance, specifically for the connection between regions in the visual cortex of the left and right brain hemispheres. This connection is made through the corpus callosum, an important WM structure within the brain and so, the comprehension of the diffusion properties of some of its characteristic fiber tracts is of extreme importance.

- **Fiber tracking enables the identification of visual-callosal WM pathways with seed points in all regions of the visual cortex defined with fMRI**

In order to identify the visual-cortex/occipital-lobe fiber tracts we first defined two VOIs: the first including the WM in each occipital lobe and the second surrounding the splenium of the corpus callosum taking into account anatomical landmarks [29]. Using fiber tracking methodologies in BrainVoyager, we estimate all WM matter pathways passing through the occipital lobe, intersecting through the splenium of the corpus callosum and projecting towards the occipital of the other brain hemisphere. Our two fiber tracking procedures (Methods; Chapter 7) identified each estimated occipital-callosal fiber tract according to their seed points or termination in regions of the visual cortex defined with fMRI, obtaining five types of visual-callosal WM pathway identifications (figure 48).

In both fiber identification procedures presented in this work, we do not have a full identification of all visual-callosal WM pathways for all of the participants, i.e. there are some individuals where we were unable to identify all five types of fibers. For both children and adults, we identify a larger amount of fibers projecting into the primary visual cortex V1 than for visual regions V2 and V3. The fiber tracking method applied by BrainVoyager also follows visual-callosal fiber tracts projecting into dorsal regions in greater number than the ones projecting into ventral regions. Indeed, we suspect that those fiber tracts projecting into ventral regions also exist, since they are identified in some individuals (graphics 1 and 16). However they are not fully identified in all individuals by our method and this may be explained due to the default restrictions of the fiber tracking algorithm used in BrainVoyager, like the FA and the angle threshold which we cannot modify in order to identify more fibers. Also, we can be in the occurrence of several fibers that may cross between themselves and this

fact is poorly fit by the diffusion tensor used with DTI. Other diffusion MRI approaches like DSI and Q-ball Imaging would be required in order to identify these fibers.

In the literature, we identify several tractographic studies estimating fiber tracts starting projecting towards the occipital lobe, like those developed by Wakana et al (1986), Dougherty et al (2005), Ben-Schachar et al (2007) and Wandel et al (2010). However, only Wakana et al (1986) and Dougherty et al (2005) had distinguished those fibers between their projections towards dorsal and ventral regions of the occipital lobe and they also found to be more difficult to estimate fibers projecting towards ventral than dorsal regions of the occipital lobe. Another interesting study is a tractography study developed by Schmahmann et al (2007) where the author identified fibers starting in the ventral occipital lobe (particularly in the visual regions V3 and V4) and entering the inferior longitudinal fasciculus [49]. However we cannot make a proper comparison with the fibers that we identified, because this study was performed using DSI methodologies.

Some studies performed in the macaque monkey, for example Lyon et al (2002), show evidences of connections between dorsal and ventral regions of the extrastriate visual cortex with the primary visual cortex V1. In two studies [51, 52], Lyon et al (2002) showed that V1 is connected with at least 12 functional regions of the visual cortex. From these connections, half of them were involving the visual area V2 and approximately 20% was involving the ventral portion of V3.These studies give evidences to the possibility of WM pathways in the human cortex passing through the splenium of the corpus callosum and projecting into ventral regions of the visual cortex in humans.

- **NF1 presents statistical alterations in diffusion properties and eigensystem values levels when compared with controls, related with myelin structural alterations, specifically a myelin degradation**

Our results show significant group effects, in diffusion and eigensystem properties of the estimated fiber tracts, for both children and adults with NF1, however with a greater effect for children. For each diffusion parameter analyzed, we first employed an ANOVA repeated measures analysis to perform a full mean comparison of each voxel belonging to each fiber tract estimated. This analysis also takes into consideration a possible measure repetition in some specific voxels, due to identification by two different fiber tract estimations.

This analysis reflected an overall group effect between controls and NF1, suggesting an overall alteration of the WM structure in individuals diagnosed with NF1, reflected by FA and axial FA decreases and MD and eigenvalues λ_2 and λ_3 increases. Significant FA and Axial FA decreases combined with MD increase are likely to be associated to diffuse and basic alterations in the WM microstructure, corresponding to a misorientation of the tissue's longitudinal order, possibly related to a myelin alteration/disruption due to loss or collapse of the WM axon's myelin [26], as illustrated in figure 49.

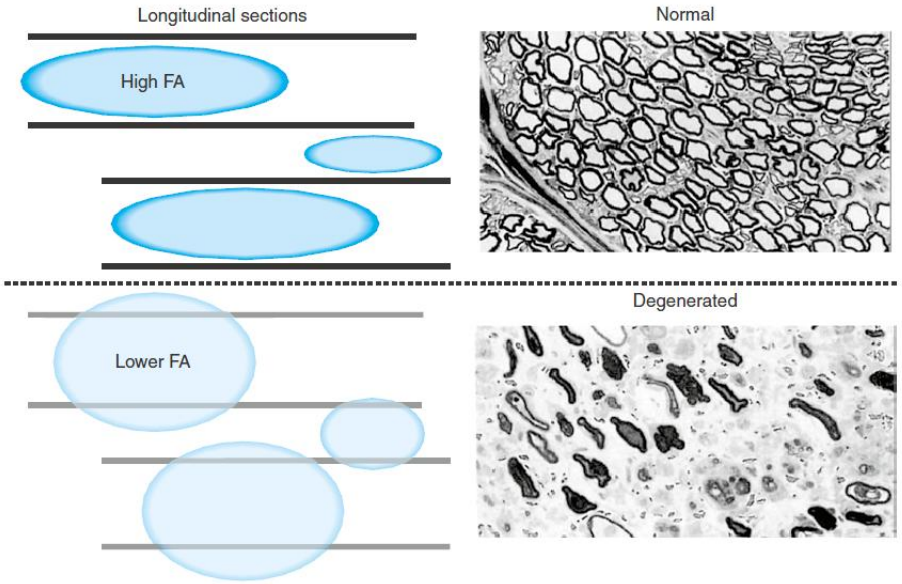

Figure 51: Schematic illustration structural damage to myelin, resulting in a loss or collapse of the myelin and reducing the anisotropy level within the tissue [26].

The increase verified in the eigenvalues λ_2 and λ_3 might explain the reduction verified in the FA and axial FA values, since the degree of anisotropy of water molecules within a tissue can be reduced by an increase of perpendicular diffusivity, as illustrated in figure 50. This feature supports the assumption made with the verified FA and MD values alteration, relating the decrease of FA values and a MD value increase to myelin degradation. The highly significant alteration verified in the eigenvalues λ_2 and λ_3 is related to the highly significant alteration verified in the axial FA values, since the myelin degradation verified in visual-callosal WM pathways is most likely caused by an alteration on the perpendicular orientation of water molecule diffusivity, instead of an alteration on the parallel orientation, which would be the case if there was a significant group effect verified for eigenvalue λ_1.

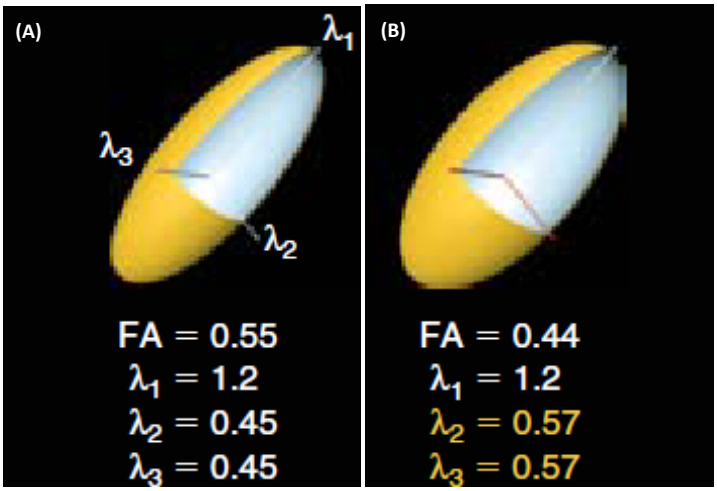

Figure 52: Schematic illustration of the perpendicular diffusivity effect in fractional anisotropy alterations. (A) higher FA, and (B) lower FA [26].

Post-hoc t-tests showed that the overall group effect was mainly due to mean differences verified in visual-callosal WM pathways with seed points in V1, but also with seed points in V2 and V3 dorsal regions. No group effect was found in visual-callosal WM pathways with seed points in ventral V3, and this fact might be related to the greater difficulty found in the identification of WM pathways with seed points in ventral regions.

Our results are indeed in accordance with some DTI studies made in NF1's UBOs that were summarized in chapter 2. Alkan et al (2005) examined a total of 30 individuals diagnosed with NF1 and 26 healthy volunteers in seven distinct locations, generating ADC maps and extracted directly from them the ADC values. They found that the ADC values had a significant increase for almost all locations, especially those located in the WM. Accordingly, Zamboni et al (2007) performed a study including 10 adults diagnosed with NF1 and 10 age-matched healthy volunteers, where FA and ADC values were measured in several brain locations, such as the brain stem, thalamus, corpus callosum and parieto-occipital regions. This study reported significant FA decrease and ADC increase for all regions in all NF1 patients, and considered that this feature was a consequence of diffuse alterations in the microstructure of the selected ROIs. Furthermore, a more recent study found FA and ADC alterations in 7 regions of interest in both hemispheres, including UBOs [24]. In this work the analysis of the eigensystem values (λ_1, λ_2 and λ_3) and the axial FA were also measured in the defined ROIs, to differentiate qualitatively between NF1 individuals and healthy volunteers. They found significant increases in the ADC values in 5 of the 7 regions, however no significant differences in FA and axial FA values in those locations. In the UBOs a significant higher eigenvalues λ_2 and λ_3 was reported,

concluding that those results were possibly related to a disturbance in the microstructure of those regions, caused by fluid accumulation.

Our results are in accordance with previous studies, since we also find an inverse alteration between MD (directly related to ADC) and FA values in the visual-callosal WM pathways. Moreover, our DTI-FT quantitative analysis in visual-callosal WM pathwayswas able to identify differences in eigenvalues λ_2 and λ_3, as previously observed in UBOs (van Engelen et al 2008).

To test the robustness of the results, a more robust fiber identification approach was performed. In this approach, we only included for analysis individuals with fiber tracts identified having seed points in both brain hemispheres for all visual regions defined with fMRI. This more robust approach was performed, to test if there was a significant alteration of the results by excluding individuals where fibers starting in a particular region of the visual cortex were identified for one of the hemispheres but not for the other. The results were quite similar to the first fiber identification approach, in what concerns the significant differences found in the group effect comparison. Therefore, it can be assumed that the lack of estimation of a particular fiber tract amount projecting to one hemisphere in comparison to the other, is not likely to be related to abnormalities in the WM microstructure, but with probable limitation of the fiber tracking algorithm used in BrainVoyager or even with the DTI methodology itself. More recent and more robust methodologies, like DSI and Q-ball Imaging would be required to estimate those fibers; however these approaches are also coupled with difficulties, mainly due to their long acquisition time (exceeding one hour per subject).

In children we found significant decreases in FA and axial FA and a significant increase in eigenvalues λ_2 and λ_3, as with the first fiber identification approach. However we did not find significant differences in adults, for any diffusion and eigensystem parameter. Additionally, we did not observed significant differences between NF1 and control children, in mean diffusivity. This result can be due to the lower number of individuals tested with the robust approach, compared to those tested with the first approach.

- **<u>NF1 children show more significant differences in the diffusion properties of visual-callosal WM pathways than adults</u>**

Several studies report the high prevalence of some NF1 phenotypic alterations in childhood, and their strong influence in crucial cognitive functions such as attention, language and visual perception [1, 4, 8].

Considering this experimental fact, in our statistical analysis we performed the ANOVA repeated measures analysis and the independent samples t-test in two groups: children (age range 7 to 17 years old) and adults (age range 19 to 42). Moreover, we had a greater number of individuals in the children group than in the adult group to the fact we observed more pronounced differences in NF1 children than in adults when compared with their matched controls. This result might also be related to a later maturation of WM pathways in NF1 individuals. To test this last assumption we performed parametric correlation analysis (Pearson) to test if there was a relation between our DTI measured parameters and age. However, no significant correlations were found in diffusion parameters or in the eigensystem values neither for controls nor NF1s and so, we are in no conditions to perform a full assumption. More analysis would be required to study this experimental fact in greater detail, starting with the performance of a similar analysis in a greater number of individuals diagnosed with NF1, especially adults. Level et al (2008) showed the existence of a correlation between WM maturation and age in healthy individuals. In this study a total of 202 healthy volunteers were tested with ages between 5 and 30 years old. It was made a full tractographic estimation and analysis of the human brain, where it can be distinguished the occipital-callosal fiber tracts passing through the splenium of the corpus callosum [50].

Given the importance of the tracts analyzed in our work to normal vision, since they are responsible for the inter-hemispheric connection and information transfer between different regions of the visual cortex, our results may help explain the visual-perception deficits observed in NF1.

- **DTI is a critical tool in the study of diffusion properties in WM pathways**

DTI allows non-invasive, *in vivo* assessment and proper illustration of WM fiber tracts and their orientation, providing also several relevant scalar parameters. This helps to understand the brain abnormalities verified in NF1, because of a better microstructural evaluation of the parenchyma, which can be achieved through DTI methodologies due to its access to the diffusion of water molecules at the micron scale. The water diffusion anisotropy properties are dependent on several factors, such as: axon packing and its internal structure, the permeability

of the cell's membrane to water, WM myelination, and even the constituents of the water within the tissue. Therefore, these are important biomarkers of the tissue condition and are relevant to pathological processes.

CONCLUSIONS

The significant FA and Axial FA decrease combined with the MD increase verified in the visual-callosal WM pathways of NF1 children are likely to be associated to diffuse and basic alterations in the WM microstructure, possibly related to a myelin alteration/disruption. This possibility is also supported by the higher axial eigenvalues (λ2 and λ3) in the NF1 group, being this feature associated to myelin degradation.

A group effect was also found in the visual-callosal WM pathways of adults, however only for the eigenvalues λ_2 and λ_3 and with a lower significance than the differences found in children. This fact might be related to a later maturation of WM pathways in NF1 individuals.

A higher group effect is found especially in visual-callosal WM pathways with seed points in the primary visual cortex (V1), and for the visual-callosal WM pathways with seed points in dorsal V2. No group effect was found in visual-callosal WM pathways with seed points in ventral V3, and this fact might be related to the greater difficulty in identifying WM pathways with seed points in ventral regions, as reported in other studies [30, 33, 34, 35, 50].

In summary, our results indicate an alteration in the myelin microstructure of the visual-callosal fiber tracks in NF1. Since these tracts are important to normal vision, the present results help to explain the visual-perceptual deficits observed in this disorder.

FUTURE WORK

Our results suggest that the visual-callosal WM pathways in children with NF1 suffer greater and more severe microstructural alterations than adults. However, since we have a lower number of adult individuals, where those fibers are estimated with our fiber tracking approach, it cannot be said with certainty that there is indeed a greater effect in children. So it would be interesting to investigate these differences in more detail, with the recruitment of more healthy and NF1 adult volunteers.

Our DTI analysis provided a full mapping of the brain of each individual with FA, MD and eigenvalues λ1, λ2 and λ3, for posterior analysis, so now all kind of fiber tracking estimations can be analyzed. Our work was about the study of visual-callosal fibers, but another interesting procedure that could be tested in the future is the estimation of other types of fibers. NF1 presents a wide range of cognitive impairments, related to alterations in several functional regions of the human brain. For example, one could estimate the fibers of the optic radiation in the lateral geniculate nucleus, also important in visual information transfer. It would be a very interesting complement of this work.

In addition, one could analyze and provide neuroanatomic information about the corpus callosum, the major WM structure in the human brain and connecting several functional regions of the brain related to cognitive functions.

REFERENCES

[1] Kayl AE, Moore BD 3rd. Behavioral phenotype of neurofibromatosis, type 1. Ment Retard Dev Disabil Res Rev. 2000; 6:117-24.

[2] Kumar, A. S. Neurofibromatosis Type 1 : Involvement of NF1 Mutations in Nervous System Tumours and Learning and Cognitive Dysfunction in this Disorder Neurofibromatosis Type 1. Journal on Developmental Disabilities. 2004; 11:41-62

[3] Payne JM, Moharir MD, Webster R, North KN. Brain structure and function in neurofibromatosis type 1: current concepts and future directions. J Neurol Neurosurg Psychiatry. 2010; 81:304-309

[4] C. Shilyansky, Y.S. Lee, and A.J. Silva. Molecular and Cellular Mechanisms of Learning Disabilities: A Focus on NF1. Annu Rev Neurosci. 2010; 33:221-243

[5] Angela DL, Nandini Patel, Robert MA, Leslie HS. Abdominal Neoplasms in Patients with Neurofibromatosis Type 1: Radiologic-Pathologic Correlation. 2005; 25:455-80.

[6] A. Alkan, A. Sigirci, R. Kutlu, H. Ozcan, G. Erdem, M. Aslan, O. Ates, C. Yakinci, and M. Egri, "Neurofibromatosis type 1 : Diffusion weighted imaging findings of brain," European Journal of Radiology, vol. 56, 2005, pp. 229-234.

[7] R.M. Costa and a J. Silva, "Review Article: Molecular and Cellular Mechanisms Underlying the Cognitive Deficits Associated With Neurofibromatosis 1," Journal of Child Neurology, vol. 17, Aug. 2002, pp. 622-626

[8] K. North, "Neurofibromatosis type 1.," American journal of medical genetics, vol. 97, Jan. 2000, pp. 119-27

[9] Moore BD, Ater JL, Copelan DR, "Neuropsychological profile of children with neurofibromatosis, brain tumour or both", J. Child Neurol, vol 9, 1995, pp. 368-77

[10] Hachin C, Iannuzzi S, Chaix Y, "Behavioral and cognitive phenotypes in children with neurofibromatosis type 1 (NF1): the link with the neurobiological level", Brain Dev, Jan. 2011, vol 33, pp. 52-61

[11] Barker, D., E. Wright, K. Nguyen, "Gene for von Recklinghausen neurofibromatosis is the pericentric region of chromosome 17", Science, vol 236, 1987, pp. 1100-1102

[12] Seizinger, B. R,m G. A. Rouleau, A. H. Lane, "Linkage analysis in von Recklinghausen neurofibromatosis (NF1) with DNA markers for chromosome 17", Genomics, 1987, vol 1, pp. 346-348

[13] Viskochil D, Buchberg AM, Xu G, Cawthon RM, Stevens J, Wolff RK, et al, "Deletions and translocation interrupt a cloned gene at the neurofibromatosis type 1 locus", Cell, 1990, vol 249, pp. 181-6

[14] Vogel F, Motulsky AG, "Human genetics. Problems and approaches", 3rd edition. Berlin. Springer, 1997, p.54

[15] Jussi Koivunen, "NF1 tumor suppressor in epidermal differentiation and growth – implications fou wound epithelialization and psoriasis, 2003

[16] K.J. Staley and A.E. Anderson, "Hyperactive interneurons impair learning in a neurofibromatosis model.," Nature neuroscience, vol. 12, Jan. 2009, pp. 8-10.

[17] Said SM, Yeh TL, Greenwood RS, "MRI mophometric analysis and neuropsychological function in patients with neurofibromatosis", Neureport, 1996, vol 7, pp. 1941-44

[18] Moore BD, "Brain volume in children with neurofibromatosis type 1 Relation to neuropsychological status."

[19] E.L. Wignall, P.D. Griffiths, N.G. Papadakis, I.D. Wilkinson, L.I. Wallis, O. Bandmann, P.E.E. Cowell, and N. Hoggard, "Corpus callosum morphology and microstructure assessed using structural MR imaging and diffusion tensor imaging: initial findings in adults with neurofibromatosis type 1.," *AJNR. American journal of neuroradiology*, vol. 31, May. 2010, pp. 856-61.

[20] J. Sevick, A.J. Barkovich, and M.S.B. Edwards, "Evolution of White in Neurofibromatosis MR Findings Matter Lesions Type 1 :," *Image (Rochester, N.Y.)*.

[21] R.G. Steen, J.S. Taylor, J.W. Langston, J.O. Glass, V.R. Brewer, W.E. Reddick, R. Mages, and E.K. Pivnick, "Prospective evaluation of the brain in asymptomatic children with neurofibromatosis type 1: relationship of macrocephaly to T1 relaxation changes and structural brain abnormalities.," *AJNR. American journal of neuroradiology*, vol. 22, May. 2001, pp. 810-7.

[22] Di Paolo DP, Zimmerman RA, Rorke LB, e tal. "Neurofibromatosis type I: pathologic substrate if high signal-intensity foci in the brain", Radiology, 1995, vol 195, pp. 721-24

[23] S.L. Zamboni, T. Loenneker, E. Boltshauser, E. Martin, and K. a Il'yasov, "Contribution of diffusion tensor MR imaging in detecting cerebral microstructural changes in adults with neurofibromatosis type 1.," *AJNR. American journal of neuroradiology*, vol. 28, Apr. 2007, pp. 773-6.

[24] van Engelen SJ, Krab LC, Moll HA, et al, "Quantitative differentiation between healthy and disordered brain matter in patients with neurofibromatosis type I using diffusion tensor imaging", AJNR Am J Neuroradiol, 2007, vol 28, pp. 773-76

[25] Eastwood JD, Fiorella DJ, MacFall JF, et al, "Increased brain apparent diffusion coefficient in children with neurofibromatosis type 1", Radiology, 2001, vol 219, pp. 354-58

[26] Heidi Johansen-Berg, Timothy EJ Behrens, "Diffusion MRI from quantitative measurement to in-vivo neuroanatomy" 1st edition, 2009

[27] E. Mooshagian, "Anatomy of the corpus callosum reveals its function.," *The Journal of neuroscience : the official journal of the Society for Neuroscience*, vol. 28, Feb. 2008, pp. 1535-6.

[28] M. Wahl, B. Lauterbach-Soon, E. Hattingen, P. Jung, O. Singer, S. Volz, J.C. Klein, H. Steinmetz, and U. Ziemann, "Human motor corpus callosum: topography, somatotopy, and link between microstructure and function.," *The Journal of neuroscience : the official journal of the Society for Neuroscience*, vol. 27, Nov. 2007, pp. 12132-8.

[29] S. Hofer and J. Frahm, "Topography of the human corpus callosum revisited--comprehensive fiber tractography using diffusion tensor magnetic resonance imaging.," *NeuroImage*, vol. 32, Sep. 2006, pp. 989-94.

[30] Witelson SF, "Hand and sex differences in the isthmus and genu of the human corpus callosum. A postmortem morphological study", Brain, 1989, vol 112, pp. 799-835

[31] F. Tong, "Primary visual cortex and visual awareness.," *Nature reviews. Neuroscience*, vol. 4, Mar. 2003, pp. 219-29.

[32] B. a Wandell, S.O. Dumoulin, and A. a Brewer, "Visual field maps in human cortex.," *Neuron*, vol. 56, Oct. 2007, pp. 366-83.

[33] R.F. Dougherty, M. Ben-Shachar, G. Deutsch, P. Potanina, R. Bammer, and B. a Wandell, "Occipital-callosal pathways in children: Validation and atlas development.," *Annals of the New York Academy of Sciences*, vol. 1064, Dec. 2005, pp. 98-112.

[34] R.F. Dougherty, M. Ben-Shachar, R. Bammer, A. a Brewer, and B. a Wandell, "Functional organization of human occipital-callosal fiber tracts.," *Proceedings of the National Academy of Sciences of the United States of America*, vol. 102, May. 2005, pp. 7350-5.

[35] M. Ben-Shachar, R.F. Dougherty, and B. a Wandell, "WM pathways in reading.," *Current opinion in neurobiology*, vol. 17, Apr. 2007, pp. 258-70.

[36] Haris S. Chrysikopoulos, "Clinical MRI and Physics", A Tutorial, Springer, 2009

[37] D. Weishaupt, V. D. Köchli, and B. Marincek, How does MRI work? Springer, Oct. 2006.

[38] Donal W. Mc Robbie, Elizabeth A. Moore, Martin J. Graves, Martin, R. Prince, "MRI from picture to protno", 2nd edition, Cambridge

[39] A. Hendrix, Magnets, Spins, and Resonances – An Introduction to the basics of Magnetic Resonance. Erlangen, Alemanha: Siemens AG Medical Solutions, 2003.

[40] Kamil Marek Gorczewski, "Multi-directional diffusion weighted imaging: Implementation, verification and clinical application", 2010

[41] Pierpaoli C, Basser PJ, "Toward a quantitative assessment of diffusion anisotropy", Magn Reson Med, 1996, vol 36(6), pp. 893-906

[42] Conturo TE, Lori NF, Cull TS, Shimony JS, "Tracking neuronal fiber pathways in the living human brain", Proc Natl Acad Sci USA, 1999, vol 96, pp. 10422-27

[43] Jones DK, Horsfield MD, Simmons A, "Optimal strategies for measuring diffusion in anisotropic systems by magnetic resonance imaging", Magn Reson Med, 1999, vol 42, pp. 515-25

[44] Mori S, Crain BJ, Chacko VP, Van Zijl OC, "Three dimensional tracking of axonal projections in the brain by magnetic resonance imaging", Ann Neurol, 1999, vol 45, pp. 265-69

[45] Parker GJM, "Tracing fiber tracts using fast marching. In: *Book of Abstracts: Eighth Annual Meeting of the International Society for Magnetic Resonance in Medicine*, ISMRM, Berkely, CA, p.85.

[46] Sporns O, Tononi G, Edelman G, "Connectivity and complexity: the relationship between neuroanatomy and brain dynamics", Neural Netw, 2000, vol 13, pp. 909-922

[47] Hagmann P, Thiran J-P, Jonasson L, Vandergheynst P, Clarke S, Maeder P, Meuli R, "DTI mapping of human brain connectivity: statistical fiber tracking and virtual dissection." *NeuroImage, vol* 19, pp.545–554.

[48] S. Wakana, H. Jiang, and P.C.M.V. Zijl, "Radiology Fiber Tract – based Atlas of Human WM Anatomy," *Radiology*, 2003, pp. 21-29.

[49] J.D. Schmahmann, D.N. Pandya, R. Wang, G. Dai, H.E. D'Arceuil, A.J. de Crespigny, and V.J. Wedeen, "Association fibre pathways of the brain: parallel observations from diffusion spectrum imaging and autoradiography.," *Brain : a journal of neurology*, vol. 130, Mar. 2007, pp. 630-53.

[50] C. Lebel, L. Walker, a Leemans, L. Phillips, and C. Beaulieu, "Microstructural maturation of the human brain from childhood to adulthood.," *NeuroImage*, vol. 40, Apr. 2008, pp. 1044-55.

[51] D.C. Lyon and J.H. Kaas, "Evidence from V1 connections for both dorsal and ventral subdivisions of V3 in three species of New World monkeys.," *The Journal of comparative neurology*, vol. 449, Jul. 2002, pp. 281-97.

[52] D.C. Lyon, J.H. Kaas, and W. Hall, "Evidence for a Modified V3 with Dorsal and Ventral Halves in Macaque Monkeys," vol. 33, 2002, pp. 453-461.

[53] [Online source] http://www.brainimaging.pt/index.php?view=venueevents&id=4%3Aanifc&option=com_eventlist&lang=en [Access date: 19/04/2011]

[54] [Online source] http://www.imaios.com/en/e-Courses/e-MRI [Access date: 01/07/2011]

[55] [Online source] http://www.humanconnectomeproject.org/ [Access date: 25/07/2011]

[56] [Online source] http://www.google.com/imgres?q=visual+v1,+v2,+v3&um=1&hl=pt-PT&sa=N&biw=1138&bih=564&tbm=isch&tbnid=OJxyw4Fccaa7pM:&imgrefurl=http://www.dana.org/news/cerebrum/detail.aspx%3Fid%3D2870

[57] National Institutes of Health Consensus Development Conference Statement: neurofibromatosis. Bethesda, Md., USA, July 13-15, 1987. Neurofibromatosis. 1988; 1(3):172-8.